Miniaturized Radio Repeater Design for Enhanced Ad-hoc Wireless Communication

by

Young Jun Song

A dissertation submitted in partial fulfillment
of the requirements for the degree of
Doctor of Philosophy
(Electrical Engineering)
in The University of Michigan
2013

Doctoral Committee:

Professor Kamal Sarabandi, Chair
Professor David R. Dowling
Professor Eric Michielssen
Professor Amir Mortazawi

To my mother Jong Hee Lee and my father Sye Ho Song

To my wife Eunhye Lee and my daughter Irene Song

for their love, support, and dedication

ACKNOWLEDGEMENTS

First and foremost, to my advisor Professor Kamal Sarabandi for invaluable encouragement, support, and guidance. Your passion and effort encouraged me throughout this long journey and provided me with the value of confidence.

My gratitude also to Professor Bo Hyung Cho for showing me the joy of working with my hands and Professor Jang Gyu Lee for encouraging me to pursue this path.

I cannot fully express my gratitude to my mother Jong Hee Lee, my father Sye Ho Song, and my brother Young Seo Song for tireless support and warm encouragement. My thanks also to my mother-in-law Kyeonghee Lee and my father-in-law Chijae Lee. Your belief and confidence in my ability inspired me to achieve greater things than I would have dreamed.

For great friendship and insightful discussions, I would like to acknowledge the past and present members of the Radlab and all of my friends. Your help and camaraderie made my life in the graduate school much more delightful and enjoyable.

Finally, I would like to thank my beautiful wife Eunhye Lee - admirable educator and the most wise woman I have ever known - for support and dedication, which made this journey possible. Your endless love and encouragement supported me throughout all of trials and brought great happiness and delight into my life. Thank you to my great and adorable daughter Irene Song for bring the joy of my life and your smiling. From the bottom of my heart, I am thankful to share my life with you. I love you.

TABLE OF CONTENTS

LIST OF FIGURES

Figure

LIST OF TABLES

Table

LIST OF APPENDICES

Appendix

LIST OF ABBREVIATIONS

ADS advanced design system

dBi the forward gain of an antenna compared with the hypothetical isotropic antenna in decibels (dB)

dBm the power ratio in decibels (dB) of the measured power referenced to 1 mW

dBsm the radar cross section (RCS) in decibels (dB) of a target referenced to 1 m^2

DGS defected ground structure

EBG electromagnetic band-gap

E-field electric-field

E-plane the plane containing the electric-field vector and the direction of maximum radiation

FDD Frequency Division Duplex

FEM Finite Element Method

HFSS high frequency structural simulator

H-field magnetic-field

H-plane the plane containing the magnetic-field vector and the direction of maximum radiation

ISM industrial, scientific, and medical

LOS line-of-sight

MIMO multiple input and multiple output

MMA multi-element monopole antenna

PEC perfect electric conductor

PIFA planar inverted-F antenna

PMC perfect magnetic conductor

PML perfectly matched layer

Q quality

RCS radar cross section

RF radio frequency

RSSI radio signal strength indicator

Rx receive

S-parameters scattering parameters

TDD Time Division Duplex

TEM Transverse Electric Magnetic

TE Transverse Electric

TM Transverse Magnetic

Tx transmit

ABSTRACT

Miniaturized Radio Repeater Design for Enhanced Ad-hoc Wireless Communication

by

Young Jun Song

Chair: Kamal Sarabandi

In complex communication channel environments the radio link coverage at microwave frequencies is mainly restricted by the exorbitant path-loss between communication nodes. Complex environments such as urban canyons and building interiors often contain numerous obstacles which impede line-of-sight propagation and cause significant path-loss. In such environments, the communication inevitably relies on multi-path propagation such as multiple reflections, diffractions, and penetration through obstacles, which can result in loss of connectivity even over short distances. As an alternative, radio repeaters have been developed to enhance the signal coverage of low-power radios in complex communication environments. Although numerous approaches have been proposed to minimize the dimensions, power consumption, and complexity of the radio repeater system, up until recently, the near-field mutual coupling between the transmit and receive antennas has been the main cause that had limited their physical dimensions and performance.

This thesis deals with development of a low-power subwavelength radio repeater system that can handle multiple channels simultaneously and does not require a specific communication protocol. To realize a small-size radio repeater, two isola-

tion techniques are presented to suppress the near-field mutual coupling between the transmit and receive antennas of the radio repeater. First, a metamaterial-based electromagnetic band-gap isolator is introduced, which prohibits substrate mode propagation simply by creating a perfect magnetic conductor wall. This isolator achieves 24 dB of isolation improvement, which enables to implement a subwavelength radio repeater with 32 dB of active amplifier gain. Secondly, a drastic suppression of the mutual coupling is accomplished using a near-field cancellation technique. This is done by placing the receive antenna between the two elements of a small transmit antenna array fed with the same magnitude but out-of-phase signals. This results in an electromagnetic null-plane at the receive location and is utilized to decrease the mutual coupling. In this approach the mutual coupling is reduced by -86 dB, which enables demonstration of a miniaturized radio repeater with more than 50 dB of active amplifier gain. The performance of the radio repeaters are characterized in the far-field using a radar system in backscattering mode. The high-gain repeater shows 21.3 dBsm of radar cross section, which corresponds to that of a 13.1 m diameter metallic sphere.

This work concludes with an analytical derivation of the repeater radar cross section and implementation of dual-channel radio repeater design. The radar cross section of the dual-channel radio repeater is compared with the estimated value and exhibits more than 26.0 dBsm for both channels.

CHAPTER I

Introduction

1.1 Motivation

For wireless network systems, the path-loss between the transmitter and receiver is the most critical factor that determines the possible range of communication between two nodes. Complex channel environments such as urban canyons and building interiors often contain numerous obstacles, which impede line-of-sight (LOS) communication and increase the path-loss. In such environments, therefore, existing long range ad-hoc communication inevitably depends on the multi-path propagation including multiple reflection, diffraction, and penetration through obstacles. Moreover, especially at high frequencies the path-loss significantly increases due to the multi-path and near-ground effects. Traditionally higher transmitter power and closely spaced communication nodes have been suggested for ad-hoc networks to improve the path-loss and extend the signal coverage in such scenarios. However, such methods increase the system complexity, consume more power, and lead to low data rate due to the higher latency. Furthermore, in the absence of LOS communication the signal due to multi-path experiences fast fading effects, which can also result in loss of connectivity even over short distances as presented in [3] and [4].

In order to mitigate these problems and improve the wireless connectivity and the signal coverage, radio repeaters have been proposed as an alternative in various

application scenarios [5, 6, 7, 8, 9, 10, 11, 12, 13, 14, 15, 16, 17, 18]. In addition, numerous commercial products utilizing the concept of the radio repeater have been introduced and fabricated [19, 20, 21, 22]. The main objective of the radio repeater is to boost and retransmit the received signal, which functions as a "repeated" base station in the corresponding site, as shown in Fig. 1.1.

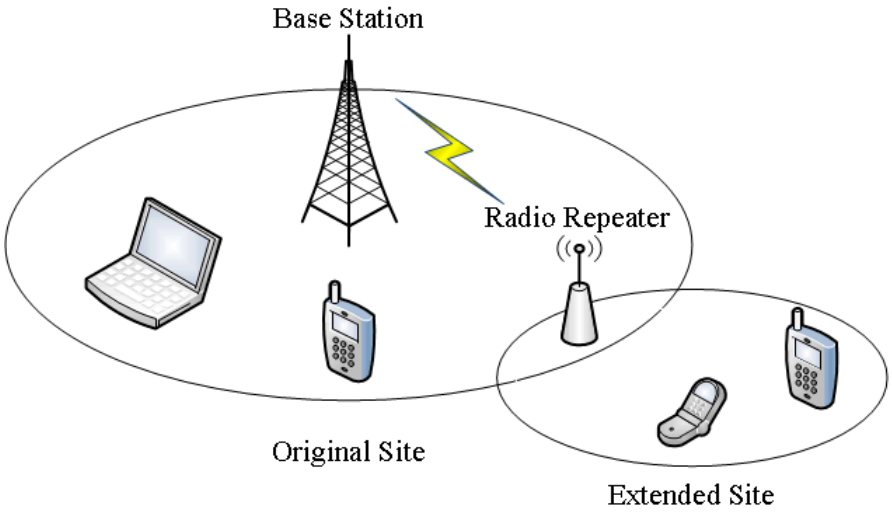

Figure 1.1: Illustration of extended signal coverage using a radio repeater.

Radio repeaters can be categorized into two classes such as "High-level" and "Low-level" repeaters [23]. The first type of the repeaters is placed on the high elevation such as tall buildings and mountains to maximize the signal coverage. In general, this type of repeater system consists of large antennas and complex circuitry for the isolation between the transmit and receive antennas. An example of the high-level repeater is illustrated in Fig. 1.2(a). The low-level radio repeaters are usually used for local communications such as building interiors and basements. This type of repeater provides the amplified radio frequency (RF) signal to blinded or shadow regions as illustrated in Fig. 1.2(b). Usually radio repeaters are extensively utilized in public safety, commercial communication, and government agencies to relay radio signals across a wider area.

As shown in Fig. 1.3, a simple radio repeater consists of Receive antenna (Rx),

(a) (b)

Figure 1.2: Common examples of radio repeaters: (a) High-level repeater [1]; (b) Low-level repeater (installed at the University of Michigan [2]).

Transmit antenna (Tx), and RF amplifier circuitry. For the downlink communication, the received signal from the base station in the LOS is amplified and retransmitted to another repeater or the intended receive node that is in the LOS, and vice versa for the uplink direction. In this operation, the isolation between the Tx and Rx antennas serves the most critical factor due to the existence of the positive feedback loop.

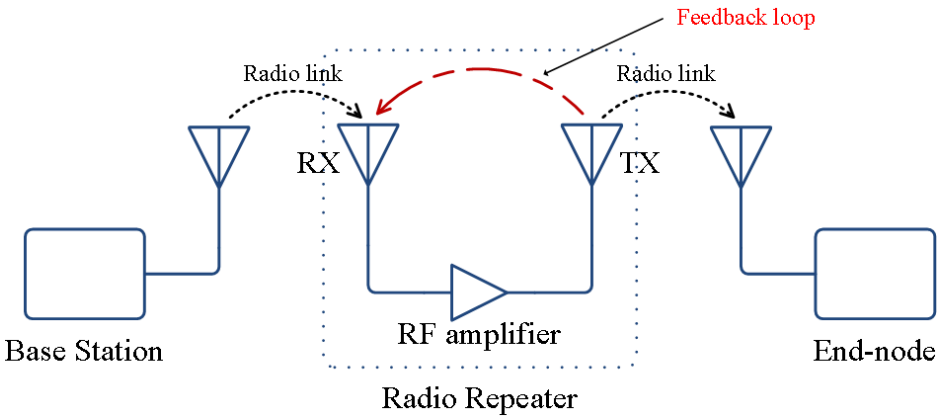

Figure 1.3: Schematic of the radio repeater system.

Conventional radio repeaters are not amenable for the application of the small portable scenarios such as emergency radio communications (collapsed building, lack of power supply) and explorations for hazardous situations. First, conventional radio repeaters use frequency division duplex or time division duplex to resolve the isolation

problem, which cause complex system setup and large physical dimensions. Second, these repeaters require a high power consumption for the operation, which is not suitable for the lack of power supply.

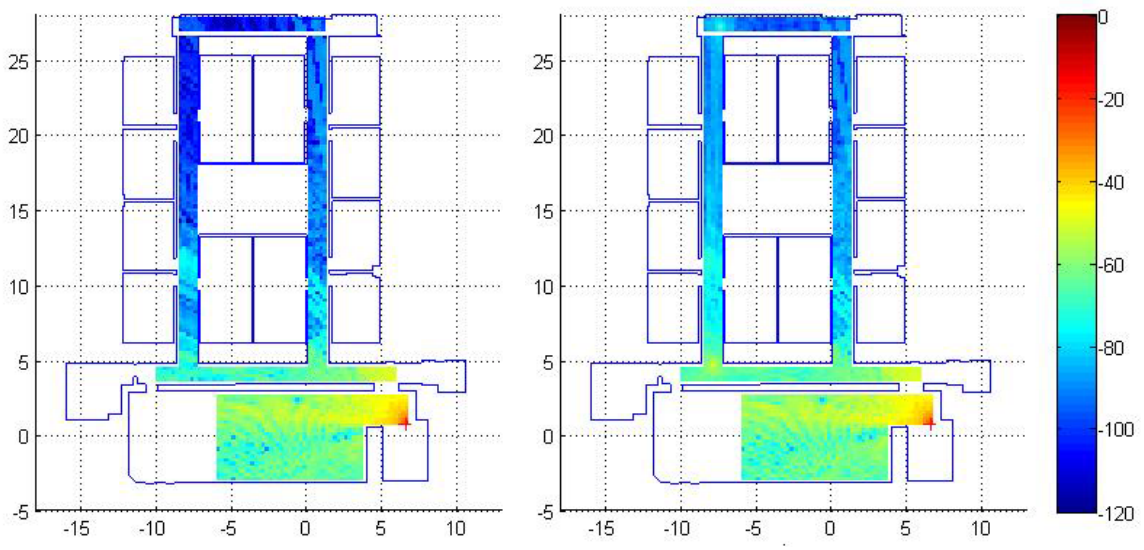

(a) (b)

Figure 1.4: Simulated wireless signal coverage in an indoor environment: (a) without repeater; (b) with two repeaters at the left-upper and left-lower corners.

This research is focused on novel designs for implementation of the low-level types of the radio repeater. Since the mutual coupling between the Tx and Rx antennas restricts the system miniaturization and performance of the repeater, various suppression techniques of the mutual coupling are investigated in this thesis. This entails in simplification of the repeater architecture, which results in the low-power and high-gain operation. An initial test of the radio repeater is simulated using the numerical wave propagation simulator developed at the University of Michigan and reported in Fig. 1.4 [24]. Placing a transmitter of 2.4 GHz at the right-lower room, the signal strength is measured along the indoor hallway 1.4(a). The complete shadow region is observed at the upper hallway. Fig. 1.4(b) shows that the signal connectivity is improved by about 20 dB once the radio repeaters are placed at the lower and upper corners of the left corridor.

1.2 Background

As the Tx and Rx antennas of the radio repeater are integrated into the compact system, this configuration inevitably creates mutual coupling between two antennas. In other words, a positive feedback loop exists in such radio repeaters as shown in Fig. 1.3, which can cause system oscillation and loss of signal connectivity, if the amplifier gain is higher than the mutual coupling. Because of this intrinsic positive feedback loop (due to the radiation and near-field effects), the active gain of the radio repeater is limited by the level of mutual coupling between the Tx and Rx antennas. When the gain of the RF amplifier is greater than the isolation level of the Tx and Rx antennas, the repeater will start to oscillate, and the communication coverage of that micro cell cannot be established. Thus, the level of mutual coupling restricts the system performance of a radio repeater with a low-power and simple architecture and how small such a system can be made.

In order to circumvent this intrinsic problem, numerous studies have been presented to suppress the mutual coupling between two adjacent antennas. For this purpose, Frequency Division Duplex (FDD) and Time Division Duplex (TDD) have been extensively investigated, and some are reported in [25, 26, 27, 28]. The first method is to divide the frequencies of the uplink and downlink signals. This methodology utilizes a FDD to reduce the mutual coupling by separating signal frequencies. However, it requires complex circuitry, larger size, and a common protocol to manage frequency allocation, which all imply higher cost and much more power consumption. The second method is to separate the signal in time domain using a TDD. This also introduces additional logic circuitry, latency, and knowledge of the repeater, transmitter and receiver locations. Consequently, the suppression of the mutual coupling without expense of system complexity and cost is the most critical factor in design of the radio repeater.

Various researches have investigated and reported to improve the isolation be-

tween multiple antennas such as multiple input and multiple output (MIMO) communication systems and diversity antenna systems. For example, one solution pertains to optimizing the locations and orientations of two antennas as reported in [29, 30]. As expected, the higher is the distance between the antennas the more is the isolation value. In addition to the physical separation between two antennas, orthogonal polarization is utilized to achieve the isolation in [31]. However, in these approaches the isolation is limited to the specific configuration of two antennas, which causes poor isolation level and extensive system optimization process. Another approach has been introduced by separating the antenna frequencies and utilizing the lumped LC filter loaded planar inverted-F antennas (PIFA) [32]. By utilizing the high impedance of the parallel LC circuit at the resonant frequency, two antennas can be isolated. However, this solution inevitably causes degradation of the antenna efficiency and bandwidth due to the finite quality (Q) factor of the lumped components. In [33, 34, 35, 36, 37, 38, 39, 40], the authors have proposed to modify the current distribution by introducing the defected ground structure (DGS) or the artificial current path such as slots and protruding extensions. Perturbing the current distribution, the isolation from one port to other ports can be achieved. However, these approaches cause contamination of the antenna radiation pattern due to the strong electric current over the ground plane. Furthermore, the artificial current may decrease the antenna gain due to the out-of-phase current distribution, if presented. Another solutions by utilizing the decoupling network also have been proposed in [41, 42, 43]. In these approaches the mutual coupling between two adjacent antennas is analyzed using a scattering matrix. The port isolation is achieved by compensating the input impedance of the scattering matrix using additional lumped components. Although the isolation can be achieved at the input port of the decoupling network, these approaches require additional transmission lines to convert the antenna input impedance to the desired trans-admittance and cause degradation of the radiation

pattern due to the existence of the coupled current for both antennas. Furthermore, the bandwidth of the isolation is limited to the narrow bandwidth of the lumped components and the bandwidth of the matching network.

Recently, the new artificial structures, so-called metamaterial, which allow manipulation of the material properties have been presented in [44, 45, 46, 47]. Electromagnetic band-gap (EBG) structures are also proposed to suppress the mutual coupling by preventing the propagation of the electromagnetic waves in a specified frequency band. This EBG structures can be categorized into two approaches. The first method is to engineer the electric and magnetic properties of the material, such as the permittivity and permeability, by introducing metallic or dielectric inclusions in a periodic manner. For example, a mushroom-like structure can suppress the mutual coupling by introducing a negative refractive index, as shown in [48, 49, 50, 51]. Another method utilizes metamaterial insulators to block the electromagnetic energy from being transmitted across the insulation boundary, as shown in [52, 53, 54]. This metamaterial insulator consists of magneto-dielectric embedded circuits, which can be modeled as parallel LC resonant circuits. However, both approaches have intrinsic limitations when attempting to suppress the mutual coupling of antennas at the commercial ISM frequency band (around 2.4 GHz). The artificial structure requires large physical dimensions. The metamaterial insulator causes fabrication complexity and cost. The state-of-the-art is summarized as shown in Fig. 1.5.

In this thesis, new methodology to suppress the mutual coupling between adjacent antennas is proposed. First, the metamaterial-based EBG channel isolator is proposed and designed. By generating a magnetic field along the signal path between the Tx and Rx antennas with an opposite sign to that of the field generated by the Tx antenna, artificial magnetic wall is generated that serve to suppress the surface wave propagation from the Tx to the Rx antenna. With this method an isolation in excess of -42 dB is achieved at the operating frequency [55]. Second, a new concept

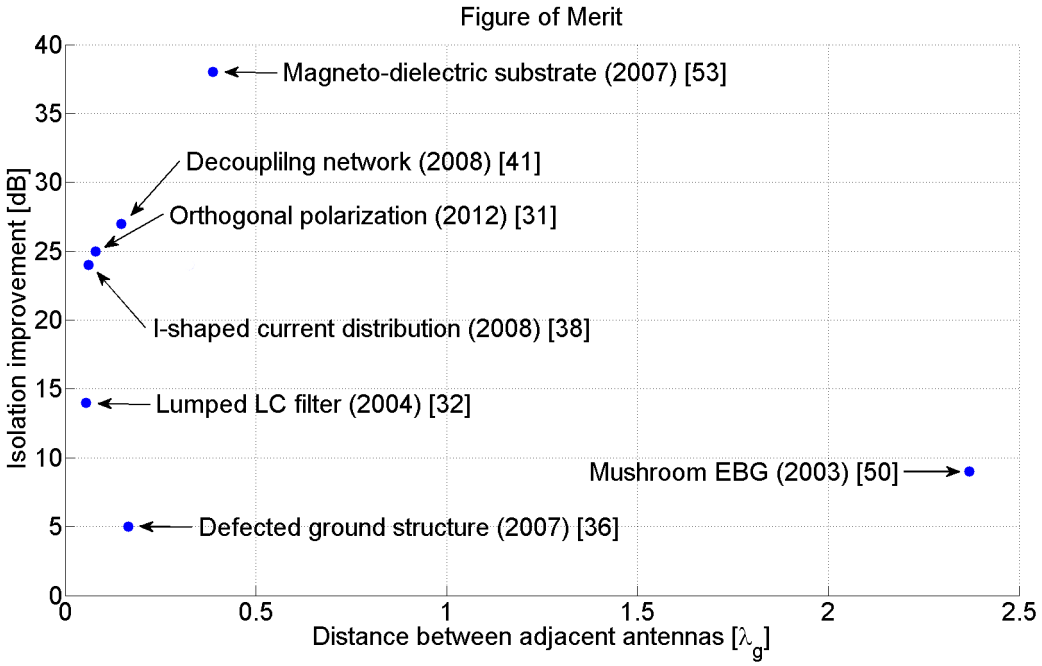

Figure 1.5: Summarized state-of-the-art for suppression of isolation.

for suppression of signal leakage between the Tx and Rx antennas is proposed and implemented. By utilizing a two element antenna array for the transmitter which is fed by a modified hybrid ring coupler, an electromagnetic null-plane is generated at the receiver location to reduce the mutual coupling drastically. It is shown that this near-field cancellation technique suppresses the mutual coupling down to -86 dB at the center frequency. It is also shown that a 50 dB gain RF amplifier chain can be inserted between the Tx and Rx antennas without system oscillation [56]. This means that over the entire band of operation of the Tx and Rx antennas the isolation is in excess of 50 dB. Finally, a dual-channel radio repeater design is proposed to achieve the simultaneous operation at two frequency channels. By utilizing parasitic elements, repeater antennas are improved to show wideband radiation bandwidth and efficiency. In addition, a closed-loop system transfer function is investigated and analyzed to numerically calculate the radar cross section (RCS) of the radio repeater system [57].

For the system validation the RCS of the proposed radio repeater is measured

and evaluated. In addition, the radio signal strength is measured and compared at the presence of the proposed repeater along the actual indoor channel environments. The beam forming technique will be introduced to enhance the gain of the proposed radio repeater.

1.3 Thesis Overview

This thesis explores a number of different performance enhancement techniques to improve the wireless signal connectivity and increase the coverage in complex channel environments. In the sections that follow, design objectives and principles of operation are presented. Novel architectures are developed and implemented in order to address the proposed techniques.

Chapter II: Investigation of Mutual Coupling Between Adjacent Antennas and Equivalent Transmission Line Model for Electromagnetic Band-Gap Isolator

The main source of the mutual coupling within the substrate is discussed in this chapter. For short distances in thin substrates, it is shown that the dominant TM_0^{odd} with a zero cutoff frequency can be approximated by a TEM wave inside and in the vicinity of the thin substrate. The propagation of this TEM wave is then modeled by an equivalent transmission line model. Detailed field profiles of the substrate mode are investigated, and the proposed electromagnetic band-gap (EBG) isolator is analyzed by modeling the EBG structure in terms of an equivalent LC circuit and establishing the proper electric and magnetic mutual couplings between the LC circuit and the equivalent transmission line model. The operation principle and modeling are detailed in this chapter.

Chapter III: Electromagnetic Band-Gap Isolator based Radio Repeater

Architecture

Implementation of a novel miniaturized radio repeater for improving wireless network connectivity in complex environment is presented in this chapter. Based on the analysis for the substrate mode in Chapter II, the metamaterial-based EBG channel isolator is designed and utilized to suppress the mutual coupling between the Tx and Rx antennas of the radio repeater. By generating the horizontal H-field along the array of the EBG channel isolators, artificial magnetic walls are generated that serve to suppress the electromagnetic wave propagation from the Tx to the Rx antenna. This results in an isolation improvement in excess of 24 dB (from -18 dB to -42 dB) at the resonant frequency. With the EBG channel isolator, it is shown that a commercial wideband RF amplifier with a gain of 32 dB can be integrated into the proposed radio repeater. The operation principle and design specifications are detailed in this chapter.

Chapter IV: Near-field Cancellation Technique based Radio Repeater Architecture

A new concept for development of a high-gain and miniaturized radio repeater is presented in this chapter. By feeding the Tx antenna array with the same magnitude but 180° out-of-phase signals, an electromagnetic null-plane is generated at the symmetry plane, where the Rx antenna is placed. In this way, the mutual coupling between the Tx and Rx antennas can be drastically reduced down to -86 dB at the center frequency. This reduction of the isolation enables to increase the active gain of the RF amplifier in excess of 50 dB within a very small form factor. The proposed radio repeater is characterized in the backscattering mode to evaluate the overall system gain and its bandwidth. An RCS value of 21.3 dBsm is measured, which corresponds to the RCS of a 13.1 m diameter of metallic sphere. The principle of the near-field cancellation and design specifications are explained and implemented

in this chapter.

Chapter V: Simultaneous Dual-channel Radio Repeater Architecture

In this chapter, a new design of dual-channel miniaturized radio repeater is presented. Due to the intrinsic positive feedback loop between the Tx and Rx antennas, radio repeaters form a closed-loop system. As a result, the overall closed-loop transfer function should be considered in the effort of evaluating system performance and RCS of the miniaturized radio repeater. The proposed closed-loop transfer function is utilized and illustrated to enhance the performance of the radio repeater. By utilizing the magnetic and electric couplings, the Tx and Rx antennas are designed to show multiple resonant frequencies and the improved radiation efficiency and bandwidth over wide frequency range. Based on the calculated closed-loop transfer function and the simulated antenna responses, the RCS of the dual-channel radio repeater is analyzed and compared with a 0.36 m of diameter of a metallic sphere. It is shown that the proposed radio repeater provides dual-channel capability with more than 26.0 dBsm of RCS on both channels.

This thesis concludes with a summary of the presented works. The notable contributions are outlined, and future directions of this research topic are briefly discussed.

CHAPTER II

Investigation of Mutual Coupling Between Adjacent Antennas and Equivalent Transmission Line Model for Electromagnetic Band-Gap Isolator

2.1 Introduction

In recent years electromagnetic band-gap (EBG) structures have been widely utilized in applications where mutual coupling between two or more closely spaced antennas is to be suppressed. Such applications include reduction of the mutual coupling among antenna elements of planar microstrip arrays [50] , reduction of cross-talk in miniaturized elements of compact arrays [53], and more recently improved isolation among antennas of multiple input multiple output (MIMO) communication systems [58, 59]. In practice EBG materials are made of subwavelength magneto-dielectric structures with particular resonant characteristics that can inhibit wave propagation near their resonance [54, 60]. In such scenarios, usually the effective permeability of the equivalent medium becomes negative. Similar behavior has also been demonstrated for designing antenna over high impedance surfaces [48, 61] and reactive impedance surfaces [62].

Due to the assumption of periodicity of EBG structures, the design procedure often relies on calculation of dispersion diagram for a unit cell. Such analyses are based on

Floquet theorem and do not account for the truncation effects that are encountered in practical situations. The numerical simulation of finite structures composed of numerous unit cells has features with dimensions much smaller than a wavelength. Thus, this requires significant computational resources, and the computational errors for such resonant structures usually exceed the required fidelity for an accurate design. One of such problems is encountered in the design of an EBG structure intended for creating high isolation between two miniaturized antennas with subwavelength separation implemented in a thin substrate [55].

In order to address these difficulties, a new equivalent circuit model for such EBG structures is presented in this chapter. A typical EBG structure, composed of two short circuited vertical pins connected by a series capacitor, is considered here to understand the physical interactions between the substrate mode and the EBG isolator. Based on a previous design [55], the lateral dimension of the interdigital capacitor is decreased, and the height of the unit cell is increased to minimize the parasitic effects from the ground plane. The proposed equivalent circuit model employs a conventional transmission line model embedding a magnetically coupled parallel LC resonant circuit. The circuit simulation and full-wave simulation responses are compared to show the validity of the proposed circuit model. It is shown that the proposed circuit model can correctly predict the reflection zero and the notch responses obtained from the full-wave simulation response.

2.2 Investigation of Substrate Mode

In most practical applications, RF communication circuits are built on dielectric substrates for system integration and miniaturization. A single-layer dielectric substrate, commonly used for many high frequency digital and RF circuits, has signal traces on top and is backed by a conducting ground plane as shown in Fig. 2.1.

In a source-free region the electric and magnetic fields can be obtained from the

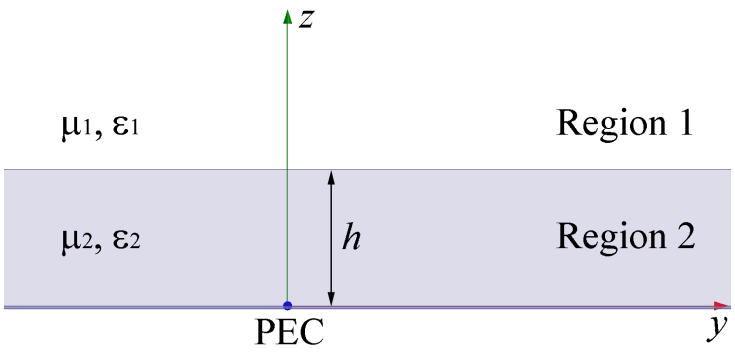

Figure 2.1: Geometry of a dielectric-coated conductor.

electric and magnetic Hertz vector potentials which satisfy Helmholtz equations. According to the boundary condition at $z = 0$, it can be shown that only $\mathrm{TM}^{\mathrm{odd}}$ and $\mathrm{TE}^{\mathrm{even}}$ modes can be guided through the substrate. For the $\mathrm{TM}^{\mathrm{odd}}$ solutions, the field quantities in each of regions are given by [63]

$$\begin{aligned} E_{1y} &= -B\nu^2 e^{-\nu z} e^{i\beta y} \\ E_{1z} &= -i\beta B\nu e^{-\nu z} e^{i\beta y} \\ H_{1x} &= -iB\omega\varepsilon_1 \nu e^{-\nu z} e^{i\beta y} \end{aligned} \tag{2.1}$$

and

$$\begin{aligned} E_{2y} &= Ak_{2c}^2 \sin(k_{2c}z) e^{i\beta y} \\ E_{2z} &= i\beta A k_{2c} \cos(k_{2c}z) e^{i\beta y} \\ H_{2x} &= iA\omega\varepsilon_2 k_{2c} \cos(k_{2c}z) e^{i\beta y} \end{aligned} \tag{2.2}$$

where the wave numbers are given by

$$\begin{aligned} k_{2c}^2 &= k_2^2 - \beta^2 \\ \nu^2 &= \beta^2 - k_1^2 \end{aligned} \tag{2.3}$$

and A and B are some constants for each of regions.

From the continuity of the tangential electric and magnetic fields at $z = h$ and

dispersion relations (2.3), the relations for k_{2c} and ν can be written as

$$\begin{aligned} &\frac{\varepsilon_1}{\varepsilon_2} X \tan X = Y \\ &X^2 + Y^2 = \left(\omega h \sqrt{\mu_2 \varepsilon_2 - \mu_1 \varepsilon_1}\right)^2 \end{aligned} \tag{2.4}$$

where $X = k_{2c} h$ and $Y = \nu h$.

The cutoff frequency for TM modes is defined as a frequency for which $\nu = 0$, thus it is given by

$$f_{c_{TM}} = \frac{m}{4h\sqrt{\mu_2 \varepsilon_2 - \mu_1 \varepsilon_1}} \text{ for } m = 0, 1, \cdots \tag{2.5}$$

Here, it should be noted that $\mathrm{TM}_0^{\mathrm{odd}}$ has a zero cutoff frequency regardless of the substrate thickness, and only $\mathrm{TM}_0^{\mathrm{odd}}$ mode can be guided through a thin substrate. Therefore, $\mathrm{TM}_0^{\mathrm{odd}}$ mode mainly contributes to the mutual coupling observed in planar circuits.

To examine the characteristics of the dominant substrate mode, let us consider a relatively thick substrate near Bluetooth operating frequency. Solving (2.3) and (2.4) for $h = 3.18$ mm, $\varepsilon_{1\mathrm{r}} = 1$, $\varepsilon_{2\mathrm{r}} = 2.2$, and $f = 2.46$ GHz, the propagation constant and attenuation constant are obtained as $k_{2c} = 56.252$, $\nu = 4.599$, and $\beta = 51.727$. The radio of the horizontal to normal components of the E-field at the interface in Region 1 (at $z = h^+$) is about -21 dB. Thus, the electromagnetic wave near the thin substrate can be approximated by a Transverse Electric and Magnetic (TEM) wave. In fact, at $z = h^+$

$$\frac{|E_y|}{|E_z|} = \frac{\sqrt{4\pi^2(\varepsilon_{2\mathrm{r}} - \varepsilon_{1\mathrm{r}})(\frac{h}{\lambda_0})^2 - X^2}}{\sqrt{4\pi^2 \varepsilon_{2\mathrm{r}}(\frac{h}{\lambda_0})^2 - X^2}} \tag{2.6}$$

from which one can determine the region of validity of quasi-TEM approximation. Numerical simulation indicates that $\frac{|E_y|}{|E_z|} <$ -20 dB can be maintained for substrates

with $\varepsilon_{2r} \leq 10$ when $h/\lambda_0 < 0.02$, and h/λ_0 can be as high as 0.03 for $\varepsilon_{2r} \leq 2.2$ as shown in Fig. 2.2. The characteristic impedance of this quasi-TEM wave is given by

$$Z_{\mathrm{TM}} = \frac{|E_z|}{|H_x|} = \frac{\beta}{\omega\varepsilon_2} \tag{2.7}$$

which equates to $Z_{\mathrm{TM0}} = 171.807\ \Omega$ at $f = 2.46$ GHz.

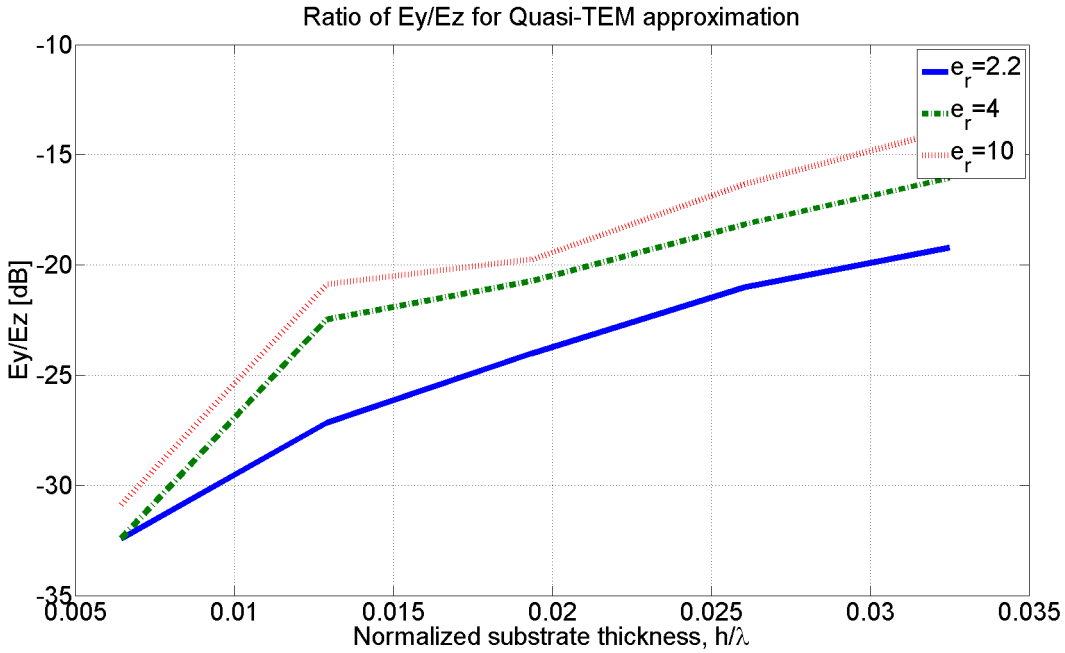

Figure 2.2: Ratio of the horizontal to normal E-field at the interface between air and a thin dielectric substrate.

2.3 Electromagnetic Band-Gap Isolator

The metamaterial-based EBG isolator is composed of single array of parallel LC resonant circuits that is magnetically coupled to the dominant substrate mode [55]. As can be seen in Fig. 2.3, the unit cell of the EBG isolator consists of vertical wires and horizontal conducting strips. The loop behaves like an inductor, and the interdigital metallic strips act as a series capacitor in the loop. For the quasi-TEM substrate mode, the horizontally polarized H-field is linked by the square loops of

the EBG, which in turn induces electric currents on the vertical wires. This induced current generates H-field in the opposite direction according to Lenz's law. When the unit cells are closely spaced to each other, the inductance of the loops is increased, and the periodic array acts like a solenoid. At resonant frequency the periodic layer acts as a perfect magnetic conductor (PMC) plane and disturbs the propagation of the substrate mode.

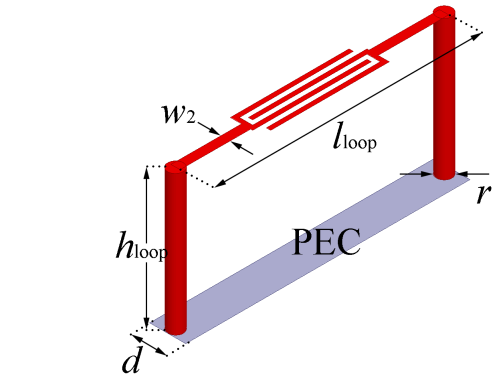

(a)

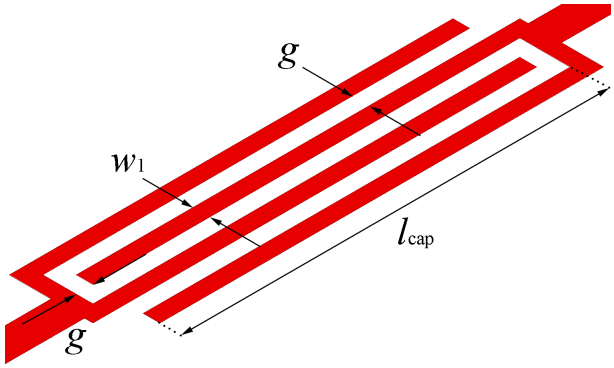

(b)

Figure 2.3: Unit cell of the electromagnetic band-gap isolator: (a) geometry and design parameters of the EBG isolator; (b) geometry and design parameters of the interdigital capacitor.

Due to the mutual coupling between the adjacent loops, the self-inductance of the square loop shown in Fig. 2.3 can be obtained from [54]

$$L_S = \frac{\mu_r \mu_0 A_{loop}}{d} \tag{2.8}$$

where $A_{\text{loop}} = h_{\text{loop}}\, l_{\text{loop}}$ is the cross sectional area of the loop, and d is the periodicity of unit cells.

As the induced current from the horizontal H-field flows through the top conducting strips, it generates E-field between the conducting strips. Since most of the E-field between these strips are in the gap and perpendicular to the metallic edges, its capacitance can be computed from the capacitance per unit length of two thin co-planar strips given by [64]

$$C_{i,e} = \varepsilon_{\text{r}}\varepsilon_0 \frac{K(k_{i,e})}{K(\sqrt{1-{k_{i,e}}^2})} \tag{2.9}$$

$$k_i = \sin(\frac{\pi}{2}\eta) \text{ and } k_e = 2\frac{\sqrt{\eta}}{1+\eta} \tag{2.10}$$

where $\eta = w_1/(w_1+g)$ is the metallization ratio and $K(k)$ is the complete elliptic integral of first kind defined by

$$K(k) = \int_0^{\pi/2} \frac{d\phi}{\sqrt{1-k^2\sin^2\phi}} \tag{2.11}$$

Since the individual capacitors between strips are connected in parallel, the total capacitance per unit length of interdigital capacitor is equal to

$$C = (n-3)\frac{C_i}{2} + 2\frac{C_i C_e}{C_i + C_e} \text{ for } n > 3 \tag{2.12}$$

where C_i is the capacitance between inner strips, C_e is between outer and inner strips, and n is the number of strips. Hence, the total capacitance of the proposed EBG isolator can be calculated easily from $C_{\text{S}} = Cl_{\text{cap}}$, where l_{cap} is the length of the strips. The designed parameters for operation at 2.46 GHz are summarized in Table 2.1. The corresponding inductance and capacitance of the unit cell are thus found to be $L_{\text{S}} = 29.9237$ nH and $C_{\text{S}} = 0.1139$ pF, respectively.

Table 2.1: Design parameters for the proposed electromagnetic band-gap isolator

l_{loop}	l_{cap}	g	w_1	w_2
6.10 mm	2.34 mm	0.10 mm	0.10 mm	0.20 mm

h_{loop}	d	r	n
3.18 mm	0.81 mm	0.36 mm	4

2.4 Equivalent Circuit Model for the EBG Isolator

As mentioned before, the substrate mode within a thin substrate can be approximated by a TEM plane wave. Also the propagation of a TEM wave in a simple medium with material parameters ε and μ can be modeled in terms of an equivalent transmission line with capacitance and inductance per unit length equal to ε and μ, respectively [65]. Hence the propagation of the substrate mode within a thin substrate can also be represented using a transmission line model as shown in Fig. 2.4. Due to the propagation symmetry along z-axis of the substrate, the Π-transmission line model is adopted. The inductance and capacitance per unit length of the transmission line L_g and C_g are given by $\mu_r\mu_0$ and $\varepsilon_{\text{r}}\varepsilon_0$, respectively.

As the EBG isolator is linked to the substrate mode through the horizontal H-field, the inductance of the EBG structure can be modeled to have an inductive mutual coupling K_1 with the inductance of the equivalent transmission line as shown in Fig. 2.4(b). The induced electric currents on two vertical wires of the EBG flow in opposite directions, and therefore the equivalent inductor of the EBG isolator is divided into two equal inductances and connected to the ground plane of the transmission line model. The mutual coupling between the vertical wires on the opposite sides is expressed by K_2. The mutual coupling between the equivalent transmission line and the horizontal conducting strip of the EBG isolator can be described through the capacitive coupling C_{P2}. Furthermore, R_{S} and C_{P1} are employed to show the finite quality (Q) factor of the EBG isolator and the parasitic capacitance between the strips and ground plane, respectively.

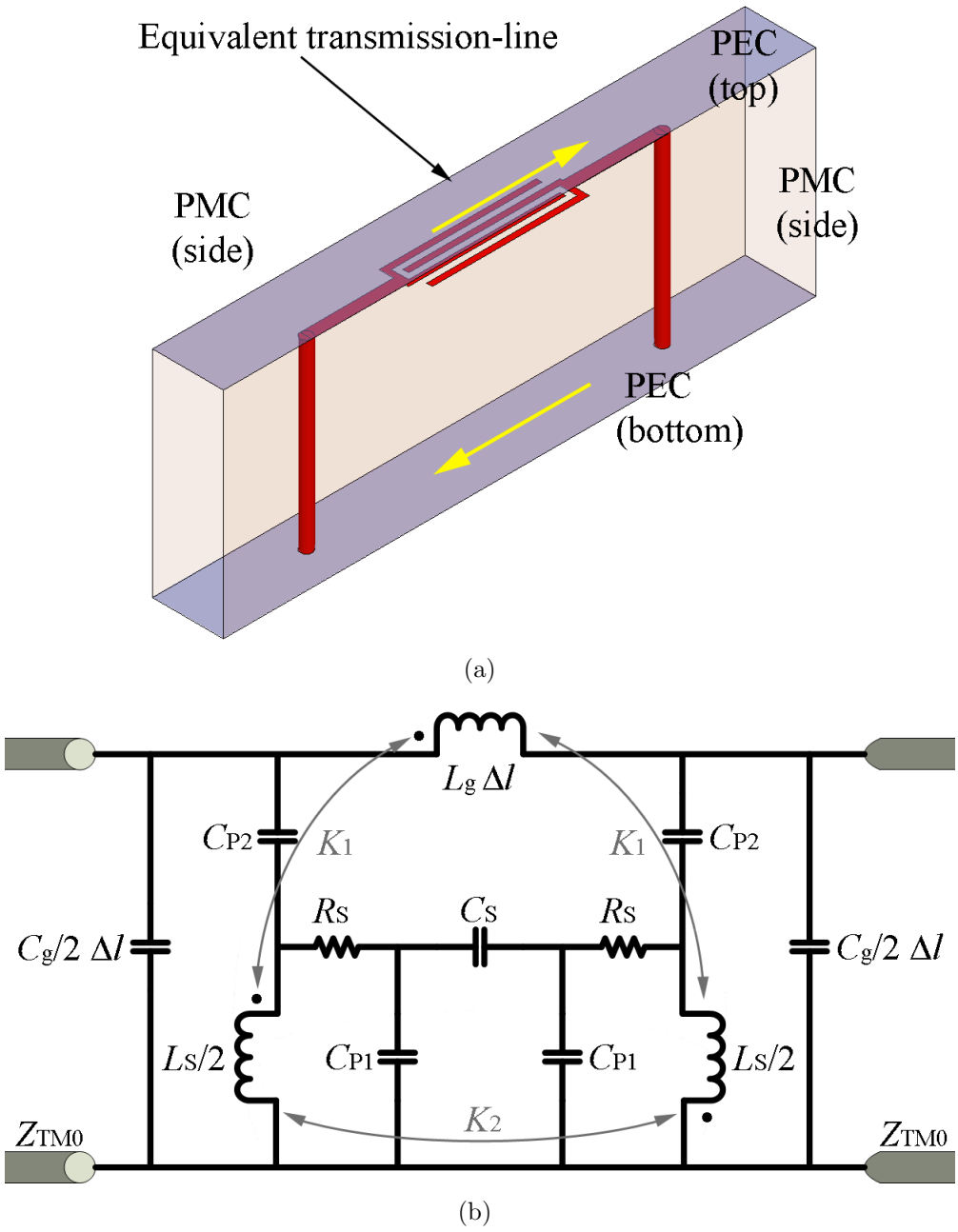

Figure 2.4: Equivalent transmission line model for the EBG isolator: (a) illustration of the conceptual equivalent transmission line; (b) equivalent circuit model for the EBG isolator embedded substrate.

In order to verify the accuracy of the EBG isolator model, a commercial full-wave solver (Ansoft's HFSS ver. 12) is utilized. As shown in Fig. 2.5(a), perfect magnetic conductor (PMC) walls are assumed to enforce the periodic condition of the unit cells. To eliminate non-physical reflections at the boundaries of the upper free space

and the front and back sides, perfectly matched layers (PML) are assigned at these openings. Perfect electric conductor (PEC) is assigned at the bottom as an infinite ground plane. In addition, two small thin pins are employed to generate the substrate mode and measure the transmission coefficient through the EBG isolator. Since only TM_0 mode can be supported, the substrate mode is coupled to the EBG isolator as shown in Fig. 2.5(b).

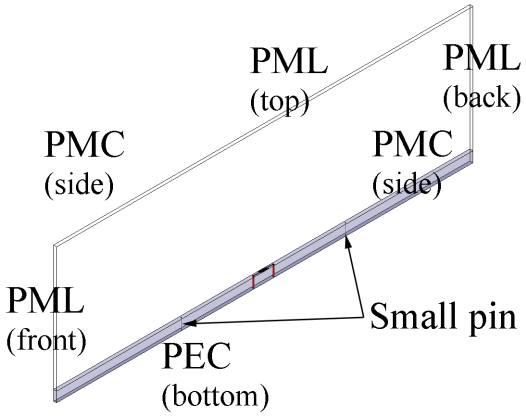

(a)

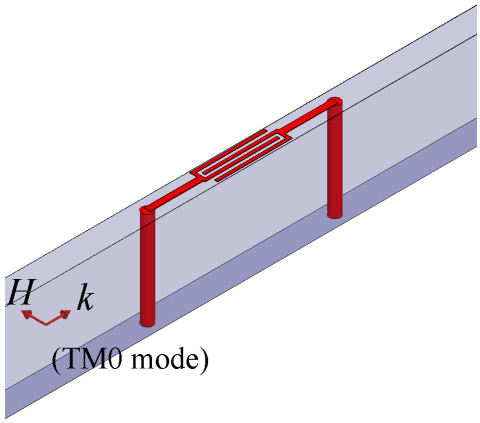

(b)

Figure 2.5: Numerical simulation setup: (a) boundary condition setup for full-wave simulation using finite element method solver; (b) propagation of TM_0 mode within the substrate.

In Section 2.3, the inductance and the capacitance of the EBG isolator are analytically evaluated from (2.8) and (2.12). The equivalent transmission line parameters are also analytically represented, and the set of values for the rest of circuit elements

are derived from the result of full-wave simulations. A curve-fitting process using a high frequency circuit simulator (Agilent's ADS 2008) is adopted to get the best fit between the circuit simulation and the full-wave response. It should be noted that a normalized frequency response is obtained by dividing the frequency response (transmission coefficient S_{21}) of the short vertical pins with and without the EBG. This approach is only valid to estimate the locations of the reflection zeros and poles of the EBG isolator. In addition, extremely dense meshes (very small tetrahedra) and very fine convergence in the finite element method (FEM) simulation are required to get accurate and stable results. The small tetrahedral meshes are required to model the gap capacitances and inductance of the loop accurately. The very fine convergence criteria is needed to get the resonant frequency of the high Q circuit correctly. The values of the circuit elements are summarized in Table 2.2. As shown in Fig. 2.6(a), three different design parameter sets and corresponding capacitance/inductance with fixed circuit elements of R_S, C_{P1}, and C_{P2} are considered to estimate the mutual coupling coefficients K_1 and K_2. The proposed equivalent circuit model shows a good agreement with the full-wave responses including a reflection zero at 2.396 GHz and a band-stop response at 2.462 GHz.

Table 2.2: Extracted circuit elements for the proposed equivalent circuit model

L_S	C_S	R_S	C_{P1}	C_{P2}	Δl
29.9237 nH	0.1139 pF	0.65 Ω	10 fF	120 fF	6.45 mm

Z_{TM0}	K_1	K_2
171.8066 Ω	0.364	-0.139

Since the mutual coupling coefficients K_1 and K_2 account for the H-field linkage from the substrate mode and the EBG isolator, these values are dependent on the physical dimensions of the EBG isolator. Using the same curve-fitting process between the full-wave simulation and the proposed circuit model, the mutual coefficients are estimated according to the length of the EBG isolator as shown in Fig. 2.6(b). As

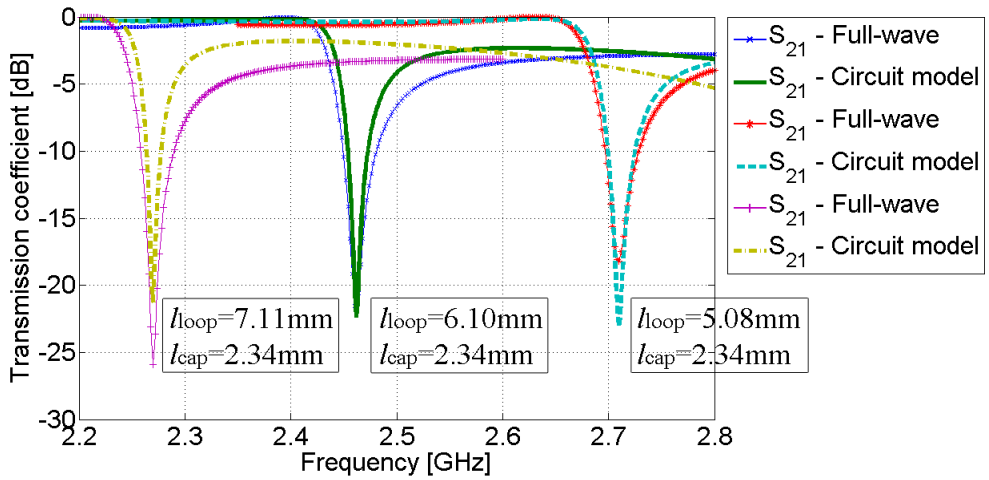

(a)

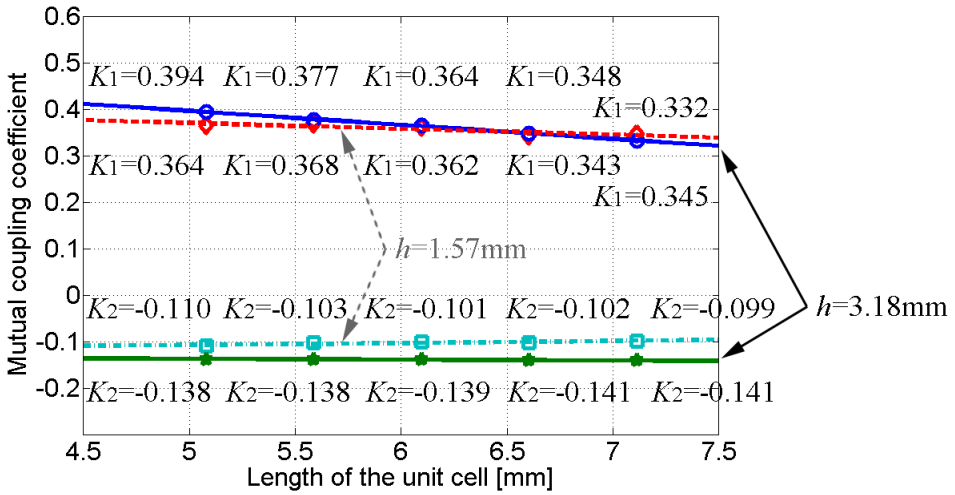

(b)

Figure 2.6: Numerical simulation results: (a) comparison between full-wave and circuit simulation responses; (b) simulated mutual coupling coefficients according to the length of the equivalent transmission line unit cell.

the unit cell becomes longer, the inductive coupling between the substrate mode and the unit cell becomes weaker. However, the mutual coupling coefficient between the two vertical wires (K_2) shows little variations to the length of the unit cell within the small range ($\lambda_g/16 \sim \lambda_g/12$).

2.5 Conclusions

In this chapter, the performance characteristics of single-layer 1-D periodic metamaterial-based electromagnetic band-gap (EBG) structures embedded in metal-backed substrates are described. It is shown that the dominant substrate mode for thin substrates can be approximated by a TEM wave inside and in the vicinity of the thin substrate. Given this TEM approximation, the magnetic coupling between the substrate mode and the EBG isolator is represented through a mutual inductive coupling and some capacitive couplings. An equivalent circuit model for the thin substrate embedding the EBG isolator is developed and analyzed. The circuit simulation response of the proposed equivalent circuit model shows a good agreement with the numerical full-wave solution. The proposed circuit model can be utilized to estimate the mutual coupling coefficients and to find the locations of the reflection zero and band-stop frequencies of the EBG isolator.

CHAPTER III

Electromagnetic Band-Gap Channel Isolator based Radio Repeater Architecture

3.1 Introduction

3.1.1 Background of this study

For wireless network systems, the path-loss between the transmitter and receiver is a critical factor that determines the possible range of communication between two nodes. Complex environments such as urban canyons and building interiors often contain numerous obstacles that impede the line-of-sight (LOS) communication and increase the path-loss. The existing long range ad-hoc communication network relies on multi-path (multiple reflection, diffraction, and penetration through obstacles). In these environments especially at high frequencies the path-loss dramatically increases, which often requires higher transmitter power and closely spaced communication nodes. Furthermore, as transmitter power increases or as transmitting nodes become closer, the potential for mutual interference between communication cells increases which, if present, can cause degradation in coverage capacity. Additionally, a topology that uses closely spaced nodes will be more expensive than a similar topology sparsely populated with nodes. To overcome these situations and to help improve the ground area coverage of communication signals without increasing the transmitter power,

radio repeaters have been extensively used in various application scenarios. Numerous studies regarding feasibility and operation of the radio repeater have been presented in [5], [10], [13], and [14].

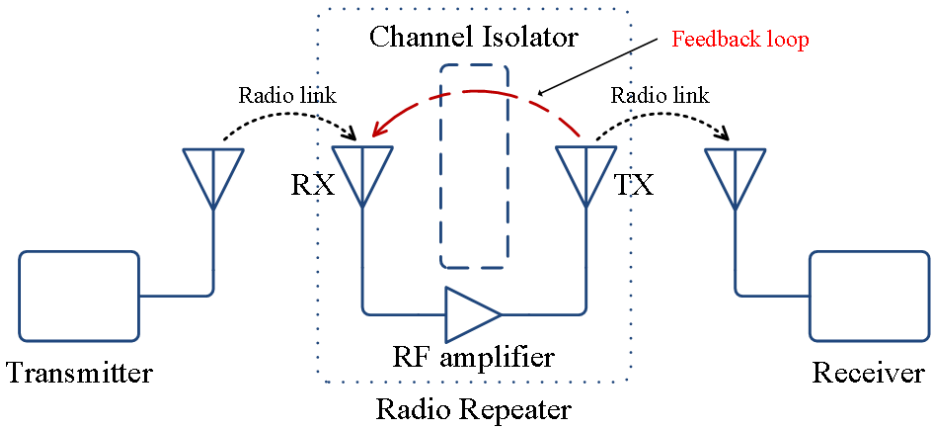

Figure 3.1: Schematic of radio link using the proposed subwavelength radio repeater.

Additionally, numerous commercial products utilizing the concept of the radio repeater have been introduced and fabricated such as in [19] and [20]. The main objective of the radio repeater in these scenarios is to achieve enhanced connectivity by amplifying a radio signal through an active device as shown in Fig. 3.1. For the downlink communication, from a base station to an end-node/unit, the signal originating at the base station is linked through the Receive antenna (Rx) of the repeater, amplified, and retransmitted through the Transmit antenna (Tx), and vice versa for the uplink direction. However, the mutual coupling between the repeater's Tx and Rx antennas generates a positive feedback loop as shown in Fig. 3.1. When the gain of the RF amplifier is greater than the isolation level of the Tx and Rx antennas, the overall system will start to oscillate, and the communication coverage of that micro cell cannot be established. Thus, the level of mutual coupling limits the performance of a radio repeater as well as the dimension and cost of the overall system. To circumvent this intrinsic problem, generally two approaches have been proposed. The first method is to divide the frequencies of the uplink and downlink signals. This methodology utilizes a Frequency Division Duplex (FDD) to reduce

the mutual coupling by separating signal frequencies. However, it requires complex circuitry, larger size, and a common protocol to manage frequency allocation, which all imply higher cost and much more power consumption. The second method is to adapt a Time Division Duplex (TDD) in time domain. This also introduces additional logic circuitry, latency, and knowledge of the repeater, transmitter and receiver locations, as presented in [25] and [26].

In this chapter, a new device is proposed to overcome the adverse effect of various complex environments by reducing the path-loss. To enhance radio connectivity and maintain low-power communication, a very small radio repeater with a large radar cross section (RCS) and an omni-directional radiation pattern is proposed. The proposed radio repeater receives the LOS signal from the transmitter, amplifies it, and then retransmits the amplified signal omni-directionally, which establishes a secondary LOS to arbitrary receivers. Thus, a series of small radio repeaters can enhance radio connectivity by establishing a LOS with the repeater nodes.

3.1.2 Benefits of the Proposed Subwavelength Radio Repeater

Fig. 3.2 shows the proposed subwavelength radio repeater. It consists of two miniaturized planar antennas capable of supporting an omni-directional pattern and vertical polarization. Additionally, a metamaterial-based isolator structure is used, and active RF amplification circuitry as well as a battery is integrated into the radio repeater platform. Since the Tx/Rx antenna of the proposed repeater shows omni-directionality over the H-plane, the uplink and downlink signal paths can be established through a single circuit path. This can reduce complexity and power consumption of RF circuitry. In addition, pure vertical polarization allows for a simple antenna structure for the base station and end-node / units as well as a decreased path-loss along the channel. It is well understood that for near-earth wave propagation scenarios vertically polarized waves experience much less path-loss compared to

horizontally polarized waves as presented in [66]. To achieve the compact dimension of the radio repeater, a metamaterial-based electromagnetic band-gap (EBG) channel isolator is utilized. By generating the normal H-field along the signal path between the Tx and Rx antennas, artificial magnetic walls are generated that serve to suppress the electromagnetic wave propagation from the Tx to the Rx antenna.

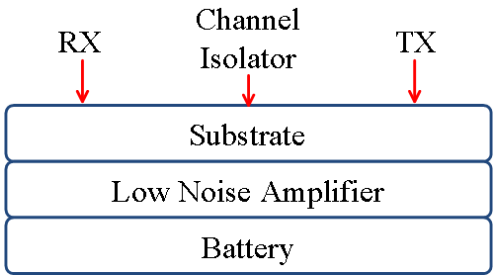

Figure 3.2: Schematic of the proposed subwavelength radio repeater system.

The proposed radio repeater occupies a very small area ($0.07\lambda_0{}^2$) with a very short height ($\lambda_0/70$) without its active circuitry. The passive components such as two miniaturized antennas and metamaterial-based isolator are presented and verified in this chapter. A prototype is fabricated using a commercially available dielectric substrate. In addition, a commercially available RF amplifier and battery are used to verify the operational feasibility of the proposed repeater. This configuration is shown to boost the power level of the received signal by 32 dB.

3.2 Design Specifications

3.2.1 Miniaturized Repeater Antenna

According to antenna theory, the intensity and polarization of the radiated field are proportional to the level and direction of the current distribution over the antenna. In many practical miniaturized antennas, the level of the excited current is limited by the impedance mismatch between the feeding network and the antenna itself. To achieve a low-profile miniaturized antenna, a quarter-wavelength microstrip

resonator fed near the short-circuited end is used. To achieve miniaturization and impedance matching a four-arm spiral shape quarter-wavelength resonator structure was utilized and presented in [67]. Although a good input reflection coefficient at the frequency of operation can be obtained, this antenna requires two layers; an upper layer consisting of the open-ended spiral shape line and a lower layer consisting of the short-circuited transmission line for the matching network to radiate the power effectively. This physical structure increases complexity and cost for fabrication. And any misalignment between the two layers can shift the operation frequency.

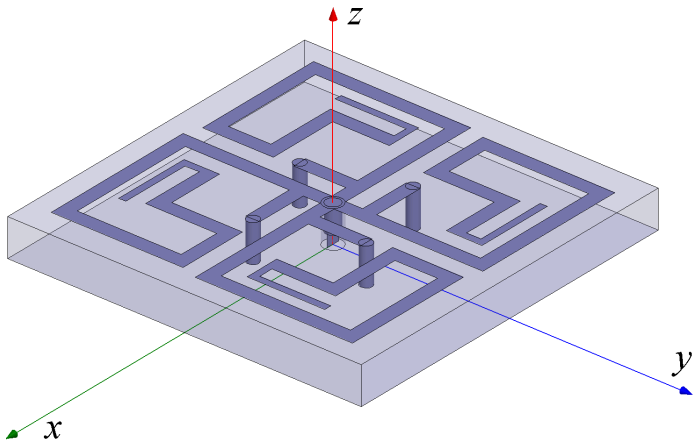

Figure 3.3: Planar multi-element monopole antenna using four quarter-wavelength arms.

The proposed new approach is to place the matching network at the same layer of the miniaturized antenna as shown in Fig. 3.3. Although the main radiation is from the shorted pins, some radiation is emanated from the spiral arms. The polarization of the radiated field from the spiral arms is horizontal. Therefore, each of the spiral arms should be placed in a symmetrical manner in order to minimize horizontally polarized radiated field. Symmetry of these arms is essential to cancel such radiated fields and eventually achieve an omni-directional vertically polarized radiation pattern. In addition, symmetry and close spacing (1.56 mm $\approx \lambda_0/70$) of the shorting pins enable the excited currents through these pins to be in-phase. The short circuited currents that pass through the four vertical pins are the dominant radiating elements and

responsible for the vertically polarized radiated field. The optimized planar multi-elements monopole antenna (MMA)[1] is designed using a commercial finite element method solver (Ansoft's HFSS ver. 11.1).

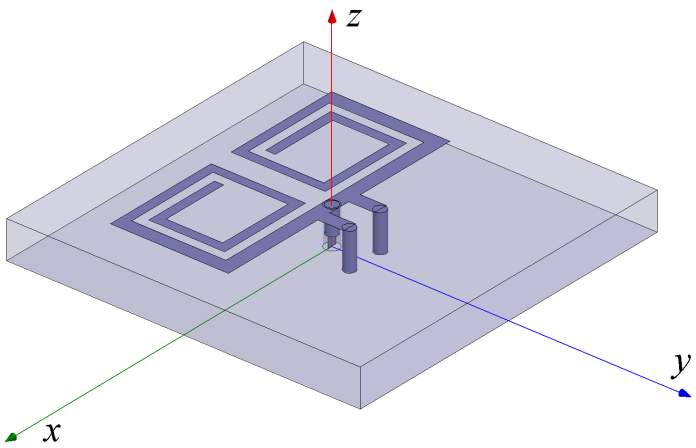

(a)

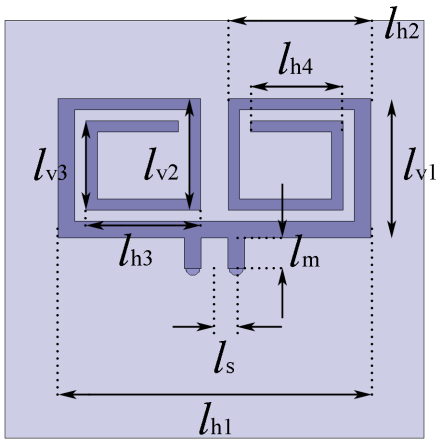

(b)

Figure 3.4: Planar multi-element monopole antenna using two quarter-wavelength arms: (a) geometry of the planar MMA; (b) design parameters.

To be incorporated into the subwavelength radio repeater, the optimized MMA must be further modified to achieve smaller dimensions. Because of the subwavelength dimension of the proposed radio repeater, a pair of the optimized MMA with four arms can produce a high level of mutual coupling within the small ground plane. Thus, the objective is to modify the MMA geometry so that mutual coupling can be

[1]This antenna was designed by Dr. Wonbin Hong.

reduced while maintaining the polarization purity and the desired radiation pattern. By utilizing only two arms of the MMA with a symmetric geometry as shown in Fig. 3.4, the horizontal current cancellation and reduction of mutual coupling can be achieved at the expense of an asymmetric radiation pattern in the E-plane. The planar MMA is designed and verified using Ansoft's HFSS. The designed geometry and parameters are shown in Fig. 3.4. The physical dimensions are optimized for operation around 2.5 GHz and summarized in Table 3.1. And all line width and spacing (between traces) values are set to 0.4 mm, except for l_{h1}, l_{v1} and l_{m} which are set to 0.6 mm.

Table 3.1: Design parameters of the planar multi-element monopole antenna

l_{h1}	l_{h2}	l_{h3}	l_{h4}	l_{v1}	l_{v2}	l_{v3}
11.20 mm	5.10 mm	4.10 mm	3.30 mm	5.00 mm	4.00 mm	3.20 mm

l_{m}	l_{s}
1.10 mm	0.78 mm

Fig. 3.5(a) presents the simulated input reflection coefficient of the planar MMA. As can be seen, the planar MMA shows a -18.5 dB of input reflection coefficient at the design frequency. The radiation pattern of the planar MMA is shown in Figs. 3.5(b), 3.5(c), and 3.5(d). The vertical polarization in the H-plane shows an omni-directional pattern, similar to that of a monopole. In addition, the level of the horizontal polarization in the H-plane is negligible compared to the vertical polarization, which implies that the cancellation between horizontal electric current is achieved effectively. Furthermore, the transmission line based antenna can be fabricated using the standard printed circuit technology. This serves to reduce the alignment error observed in the multi-layer design, and hence the fabrication process and the discrepancy between the simulation and measurement are reduced significantly.

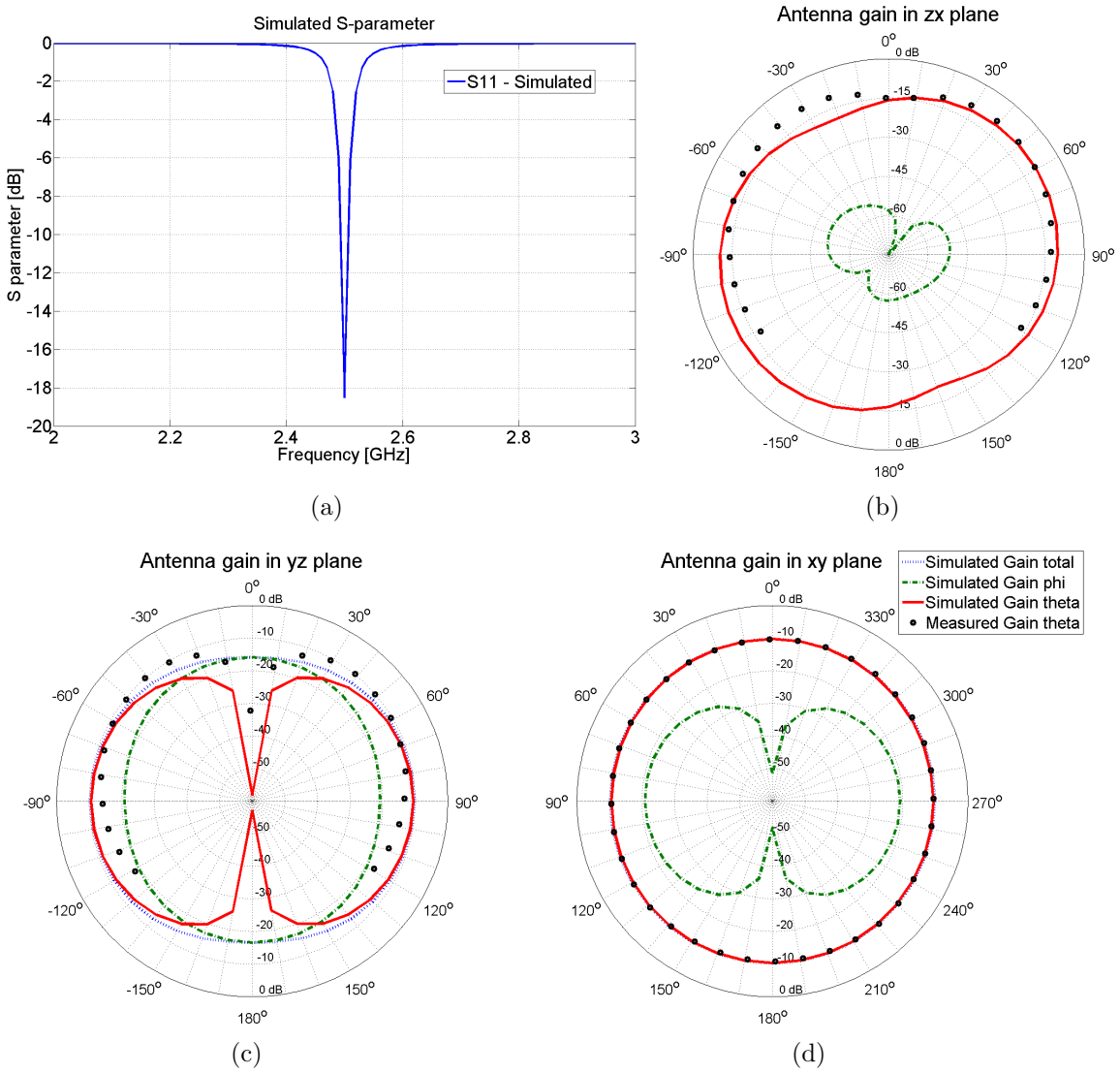

Figure 3.5: Simulated responses of the planar MMA: (a) input reflection coefficient; (b) radiation pattern in E(zx)-plane; (c) radiation pattern in E(yz)-plane; (d) radiation pattern in H(xy)-plane.

3.2.2 Metamaterial-based EBG Channel Isolator

In practical antenna systems, the mutual coupling between adjacent antennas restricts compact integration of multiple antennas in a small area for applications such as multiple input and multiple output (MIMO) communication systems. To suppress the mutual coupling, various approaches have been studied and presented in [48], [50], and [53]. In general, these studies can be categorized into two approaches. The

first method is to engineer the electric and magnetic properties of the material, such as the permittivity and permeability, by introducing an artificial structure. For example, a mushroom-like structure can suppress the mutual coupling by introducing a negative refractive index, as shown in [48] and [50]. Another method utilizes metamaterial insulators to block the EM energy from being transmitted across the insulation boundary, as shown in [53]. This metamaterial insulator consists of magneto-dielectric embedded circuits, which can be modeled as parallel LC resonant circuits. However, both approaches have intrinsic limitations when attempting to suppress the mutual coupling of antennas at the commercial ISM frequency band (around 2.5 GHz). The artificial structure requires large physical dimensions, and the metamaterial insulator causes fabrication complexity and cost.

To address these limitations, a metamaterial-based EBG channel isolator is proposed and designed as shown in Fig. 3.6(a). The proposed isolator is designed to resonate at the desired channel frequency and decrease the mutual coupling by suppression of the surface waves in the substrate generated by the vertical pins of the MMA. The vertical pins create a Transverse Magnetic (TM) wave in the substrate with zero cutoff frequency. The H-field is parallel to the ground plane and perpendicular to the pins. To inhibit propagation of the TM surface wave, a metamaterial EBG layer can be utilized. The advantage of the band-gap material is that it creates an equivalent open circuit to the surface wave as opposed to a short-circuit that a metallic wall can produce.

The band-gap metamaterial consists of an array of the parallel LC resonant circuits that are magnetically coupled with the substrate mode. This is realized using unit cells that consist of vertical wires and horizontal conducting strips, which behave like a distributed inductor and a distributed capacitor, respectively. Using image theory, when each loop is imaged a larger loop having a larger inductance and a smaller capacitance is formed as shown in Fig. 3.6(b). Assuming the fundamental mode

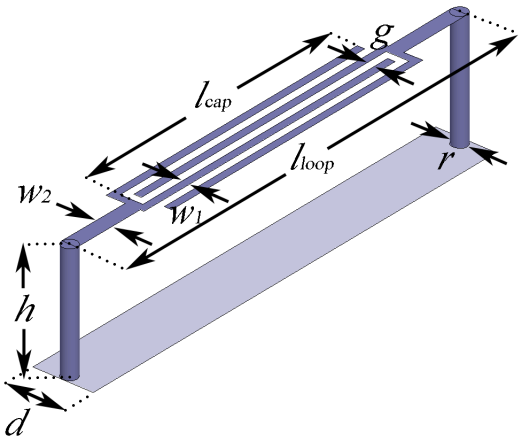

(a)

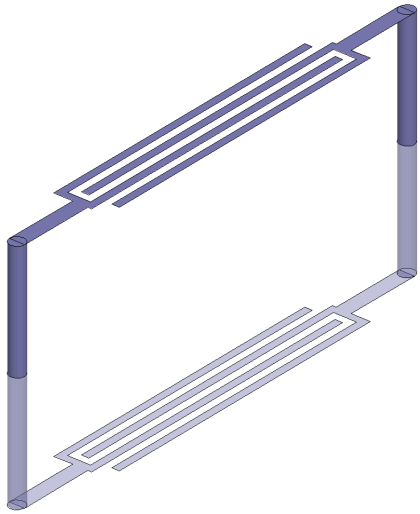

(b)

Figure 3.6: Unit cell of the metamaterial-based EBG channel isolator: (a) geometry and design parameters of the unit cell; (b) illustration of the square loop by image theory.

propagates from the Tx to the Rx antenna through the substrate, the horizontally polarized H-field linked by the square loop induces an electric current on the vertical wires. In addition, this induced current generates H-field which is perpendicular to the loop. When the unit cells are closely spaced to each other, the inductance of the loops is increased and the periodic array acts like a solenoid. At resonance the periodic layer acts as a Perfect Magnetic Conductor (PMC) plane. Due to the mutual coupling

of the adjacent loops, the self-inductance of the square loop as shown in Fig. 3.6(b) can be obtained from [54]

$$L_{\mathrm{s}} = \frac{\mu_{\mathrm{r}}\mu_0 A_{\mathrm{loop}}}{d} \tag{3.1}$$

where $A_{\mathrm{loop}} = h\ l_{\mathrm{loop}}$ is the internal area of the loop and d is the periodicity of unit cells.

The quality (Q) factor of the equivalent single pole isolator affects the performance and isolation bandwidth. Thus, commercial lumped capacitors with finite deviation of capacitance values and low Q factor will cause the suppression of the mutual coupling to deteriorate. To simultaneously reduce the deviation of these values, improve the Q factor, and lower the cost of fabrication, printed circuit technology can be utilized to implement the capacitors. As mentioned, the H-field induces the electric current on the vertical wires, and this current transforms to a displacement current (E-field) as it gets through the gaps between the fingers of the series interdigital capacitor. As most of the E-field between the metallic strips of this capacitor is in the gap and perpendicular to the metallic edges, its capacitance can be computed from the capacitance per unit length of two thin co-planar strips given by [64]

$$C_{i,e} = \varepsilon_{\mathrm{r}}\varepsilon_0 \frac{K(k_{i,e})}{K(\sqrt{1 - {k_{i,e}}^2})} \tag{3.2}$$

$$k_i = \sin(\frac{\pi}{2}\eta) \text{ and } k_e = 2\frac{\sqrt{\eta}}{1+\eta} \tag{3.3}$$

where $\eta = w_1/(w_1 + g)$ is the metallization ratio and $K(k)$ is the complete elliptic integral of first kind defined by

$$K(k) = \int_0^{\pi/2} \frac{d\phi}{\sqrt{1 - k^2 \sin^2 \phi}} \tag{3.4}$$

Since the individual capacitors between fingers are connected in parallel, the total capacitance per unit length of interdigital capacitor is equal to

$$C = (n-3)\frac{C_i}{2} + 2\frac{C_i C_e}{C_i + C_e} \text{ for } n > 3 \tag{3.5}$$

where C_i is the capacitance between inner strips, C_e is between outer and inner strips, and n is the number of fingers. Hence, the total capacitance of the proposed isolator can be calculated easily from $C_{\text{s}} = Cl_{\text{cap}}$, where l_{cap} is the length of the fingers. The interdigital capacitor is centered between two vertical wires. The designed parameters are summarized in Table 3.2. The length and height of the unit cell are chosen to be 6.25 mm $\times$ 1.57 mm. The corresponding inductance and capacitance of the unit cell are thus found to be 15.2132 nH and 0.1869 pF, respectively. Based on this calculation, the self resonant frequency is calculated to be 2.98 GHz.

Table 3.2: Design parameters of the metamaterial-based EBG channel isolator

l_{loop}	l_{cap}	g	w_1	w_2
6.25 mm	3.84 mm	0.10 mm	0.10 mm	0.20 mm

h	d	r	n
1.57 mm	0.81 mm	0.20 mm	4

3.3 Parametric Studies and Optimization

3.3.1 Optimal Configuration without the Metamaterial-based EBG Channel Isolator

In Section 3.2, the principle of operation of the MMA was established. The planar MMA with two symmetric arms and vertical pins was designed on a small ground plane and was shown to produce a very good impedance match and vertical polarization. This design is further optimized to be integrated into the metamaterial-based EBG channel isolator as shown in Fig. 3.7. As mentioned before, two arms of the

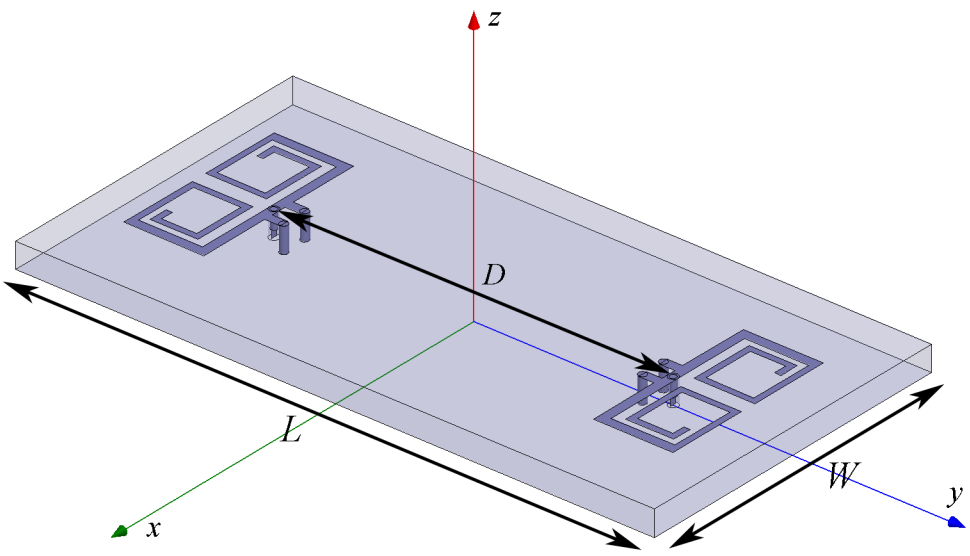

Figure 3.7: Geometry of the repeater platform without the metamaterial-based EBG channel isolator.

original MMA that would come close to the metamaterial isolator are removed. The H-field from these arms could have coupled to the isolator loops and established a link between the two antennas instead of isolating them. In a miniaturized antenna, the size of the ground plane can also affect the performance of the antenna. The edge currents on the ground plane affect the radiation pattern, directivity, and polarization. To maintain small physical dimensions, the design parameters for the optimized configuration include the position of the Tx and Rx antennas as well as the dimensions of the ground plane. The optimization is performed using HFSS to achieve impedance matching at the desired frequency, maintaining an isolation level smaller than -20 dB, and minimizing the size of the ground plane.

Fig. 3.8(a) represents a parametric study where the simulation responses of the mutual coupling (transmission coefficient S_{21}) between the Tx and Rx antennas are displayed. In this simulation the spacing between the antenna and edges of the ground plane are fixed and the distance between the two antennas, D is varied. As can be seen, the distance between the two antennas does not play a major role in the mutual coupling between the two antennas. This implies that the amount of coupling

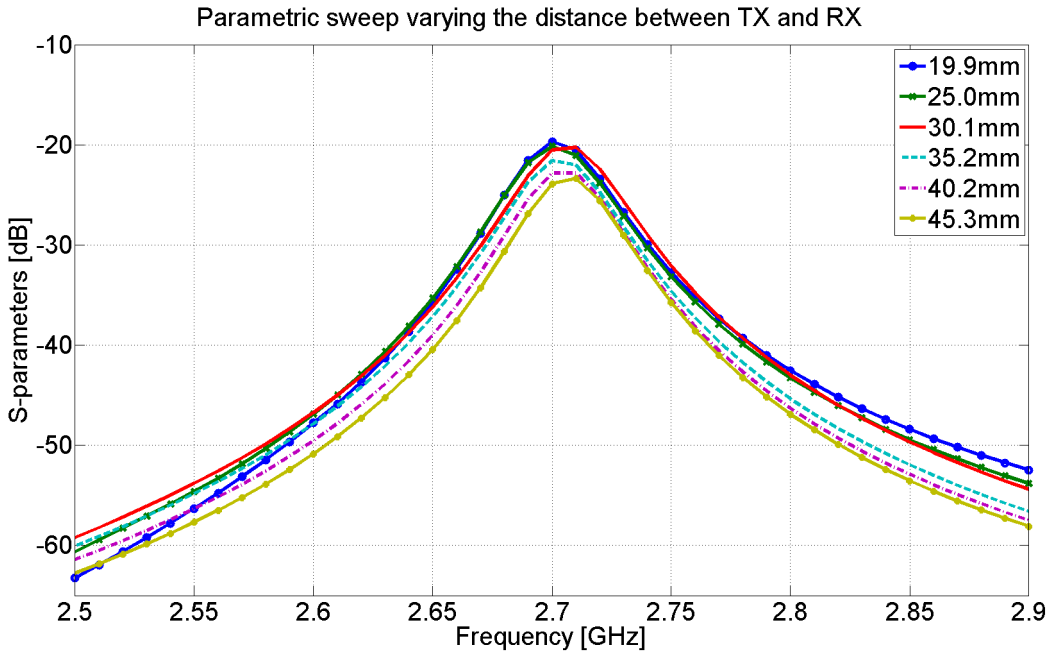

(a)

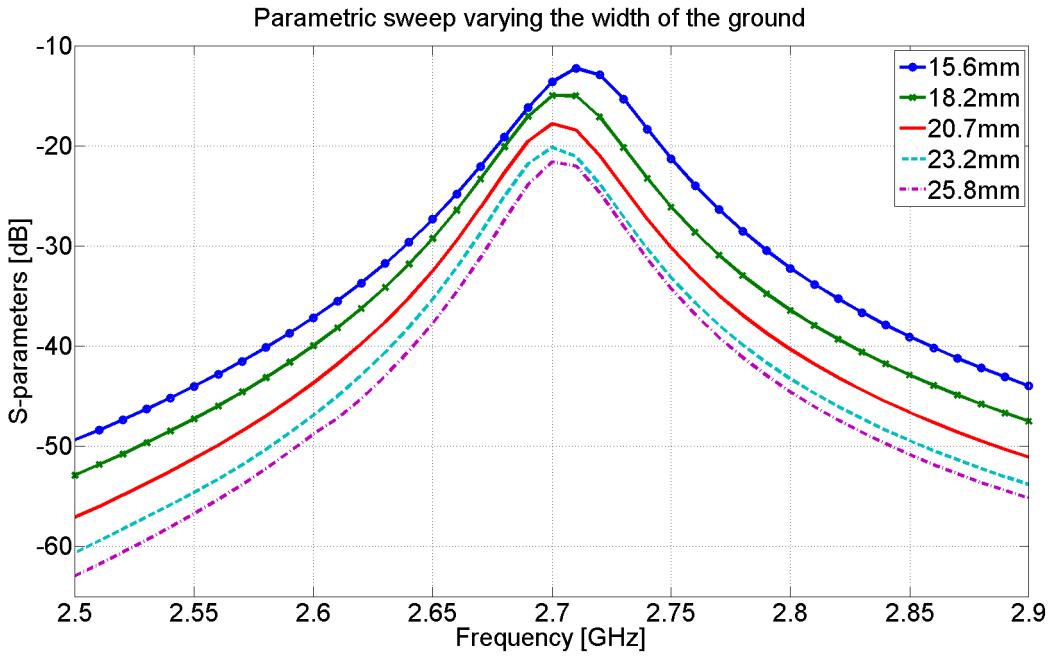

(b)

Figure 3.8: Simulated mutual coupling between the Tx and Rx antennas shown in Fig. 3.7: (a) varying the separation between the Tx and Rx antennas; (b) varying the width of the ground plane.

from surface wave propagation is not affected by the separation distance within the specified range of distances shown in Fig. 3.8(a). However, in choosing the ground plane size the overall dimension of the subwavelength radio repeater platform and the space for the metamaterial-based EBG channel isolator should be taken into account to avoid any interaction between the two antennas and the metamaterial-based EBG channel isolator. The optimized distance between the two antennas is found to be 25 mm. In addition, the width of the ground plane affects the level of mutual coupling due to excitation of edge currents. This effect is shown in Fig. 3.8(b) where all other dimensions are fixed (D=25 mm, L=40 mm) and W is changed. To account for the integration of an RF amplifier on the backside, the dimensions of the platform are finally chosen to be 40.01 mm $\times$ 20.68 mm, which corresponds to $\lambda_0/2.75 \times \lambda_0/5.32$.

3.3.2 Metamaterial-based EBG Channel Isolator and Antenna Integration

The geometry of the proposed miniaturized radio repeater is composed of two miniaturized low-profile antennas capable of radiating vertical polarization and a metamaterial isolator layer as shown in Fig.3.9. As mentioned before, close spacing between the antennas and the isolator causes the mutual coupling, and therefore it affects the performance of the repeater. Specifically, the antennas input impedances and the resonant frequency of the isolator both change as a result of the placement of the antennas and the isolator. The current distribution on the ground plane is used to evaluate the optimal placement of the isolator. As all of the physical parameters are related to each other through various electromagnetic interactions, optimization is achieved through adjusting the length of the isolator loop and the strip iteratively using HFSS.

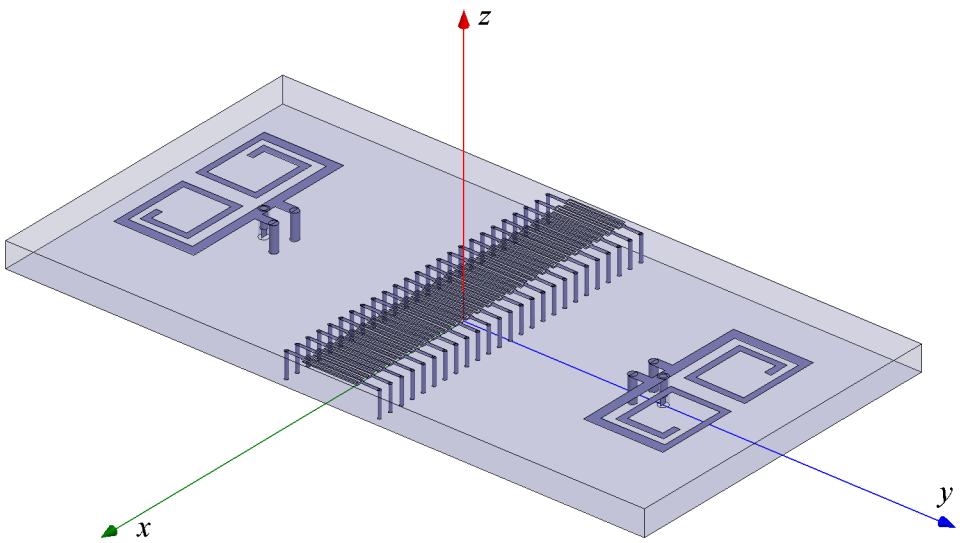

Figure 3.9: Geometry of the subwavelength radio repeater platform with the metamaterial-based EBG channel isolator.

As an initial step in the design, the Tx and Rx antennas as well as the isolator are designed separately. For integration, since multiple resonant structures within subwavelength dimensions are used, the use of manual mesh modifications in HFSS

is required to capture the details of the fields around the isolator. The designed geometry is in Fig. 3.9. Physical parameters are optimized for the repeater to operate around 2.72 GHz and are reported in Table 3.3. The optimized simulation response and measured data are discussed in Section 3.4 and 3.5.

Table 3.3: Design parameters of the subwavelength radio repeater

Design Parameters	Optimized Dimension
Distance between two antennas (D)	24.99 mm
Distance between two vertical wires (l_{loop})	5.84 mm
Length of strip fingers (l_{cap})	3.38 mm
Width of platform (W)	20.68 mm
Length of platform (L)	40.01 mm
Height of platform	1.57 mm
Adjusted Antenna Geometry (see Fig. 3.4)	**Optimized Dimension**
l_{h4}	1.21 mm
l_{v2}	3.80 mm
l_{v3}	3.00 mm
l_{m}	0.97 mm

3.4 Repeater Simulation Results

In this section full-wave analysis is carried out to examine the performance of the proposed repeater. Fig. 3.10 shows the simulated S-parameters of the optimized subwavelength radio repeater platform. As shown, a -20 dB of transmission coefficient can be achieved between the Tx and Rx antennas without the metamaterial-based EBG channel isolator with designed dimensions (assuming the two antennas are well matched.) Incorporating the metamaterial-based EBG channel isolator, the transmission coefficient drops to -30 dB. Also shown is that the antenna response is affected due to the interaction between the antennas and the isolator. In fact, per our design the antennas are well matched (over -15 dB of input reflection coefficient), and the center frequency is at the desired value in the presence of the isolator. The presence of the antenna also affects the isolator frequency response. As shown before, the res-

onant frequency of an isolated unit cell of the metamaterial isolator is at 2.98 GHz. With some small adjustments, in the presence of the antenna, this resonance occurs at 2.72 GHz as shown in Fig. 3.10.

It should be noted here that if the ground planes of transmit and receive antennas are disconnected improved isolation can be achieved. However, this way no amplifier can be inserted between the transmit and receive antennas.

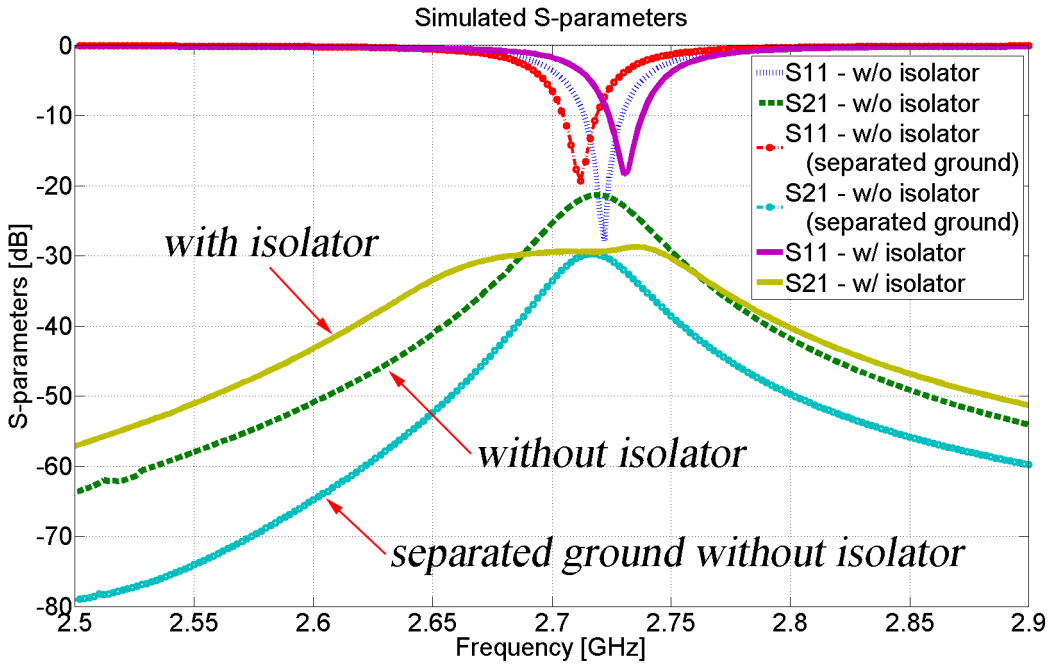

Figure 3.10: Simulated S-parameters of the subwavelength radio repeater with and without the metamaterial-based EBG channel isolator.

The simulated radiation patterns in H-plane are represented in Fig. 3.11. In order to provide enough area for two modified antennas and the metamaterial-based EBG channel isolator, the ground plane should be extended along the longitudinal direction, which breaks the symmetry of the ground plane. Although the planar MMA with square ground plane shows pure vertical polarization in H-plane (see Fig. 3.5(d)), the horizontal induced current on the rectangular ground plane generates horizontal polarization in H-plane as shown in Fig. 3.11(a). In all cases, however, the antenna shows around -9 dBi of gain in vertical polarization. The gain of the antenna is

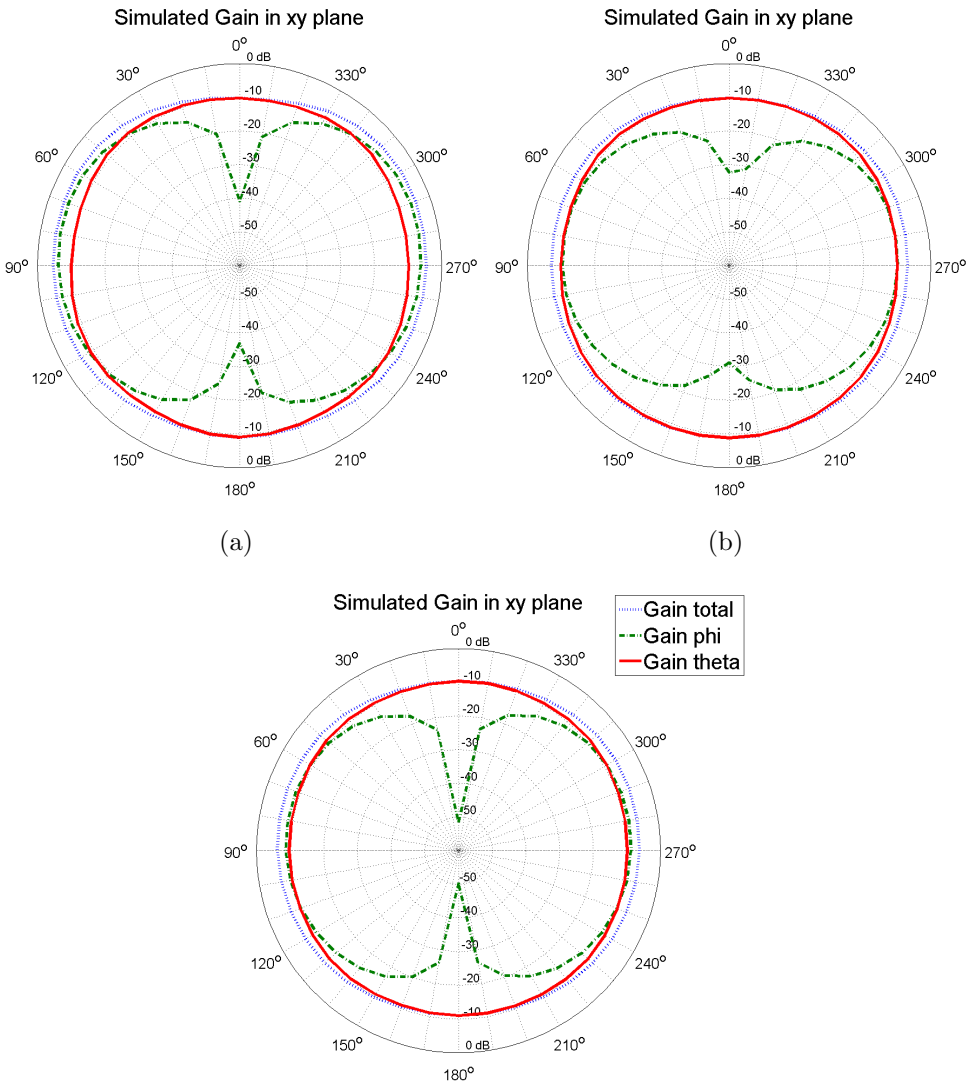

(a) (b)

(c)

Figure 3.11: Simulated radiation patterns in H(xy)-plane: (a) single ground plane without the metamaterial-based EBG channel isolator; (b) separated ground planes without the metamaterial-based EBG channel isolator; (c) single ground plane with the metamaterial-based EBG channel isolator.

limited due to dielectric and metallic losses. Increasing the dielectric thickness and increasing antenna dimensions increase the gain. Also it should be noted that the distance between two antennas is about 25 mm. For such small separations, the coupling mainly comes from the antennas' near-field.

Fig. 3.12 shows the H-field distribution over the ground plane for the repeater

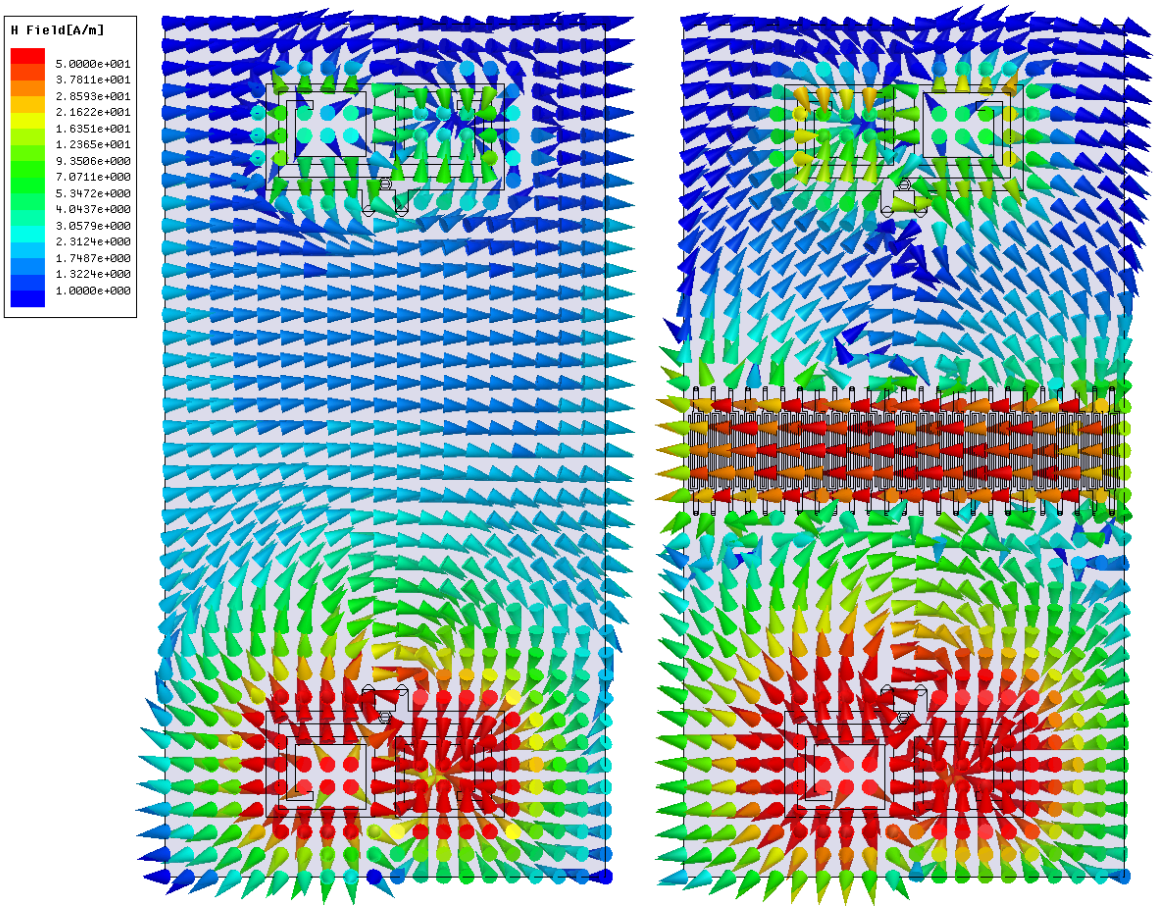

(a) (b)

Figure 3.12: Simulated H-field distributions on the substrate: (a) subwavelength radio repeater without the metamaterial-based EBG channel isolator; (b) subwavelength radio repeater with the metamaterial-based EBG channel isolator.

with and without the isolator. As expected, the horizontal H-field generated from the lower antenna in Fig. 3.12(a) propagates through the substrate and produces the mutual coupling to the top antenna. When incorporating the metamaterial-based EBG channel isolator, Fig. 3.12(b) indicates that the horizontal H-field is maximized within the metamaterial-based EBG channel isolator. This implies that the surface currents (perpendicular to the direction of the H-field in the EBG channel isolator) are interrupted by the isolator, as shown in Fig. 3.13.

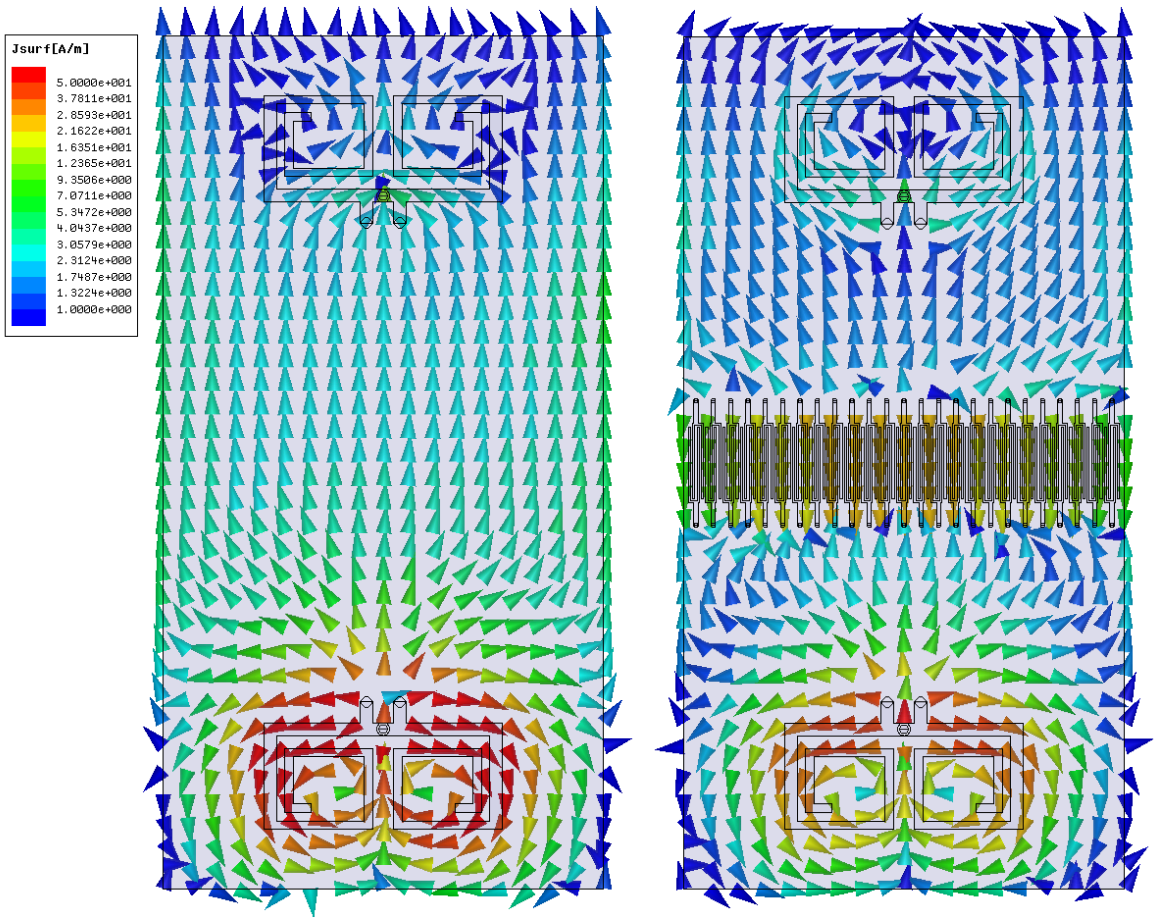

(a) (b)

Figure 3.13: Simulated current distributions on the ground plane: (a) subwavelength radio repeater without the metamaterial-based EBG channel isolator; (b) subwavelength radio repeater with the metamaterial-based EBG channel isolator.

3.5 Experimental Results

A prototype of the proposed subwavelength radio repeater system is fabricated using a 1.57 mm-thick Rogers RT/duriod 5880 substrate ($\varepsilon_r = 2.2$), as shown in Fig. 3.14. Fig. 3.15 shows the measured S-parameters of the subwavelength radio repeater and indicates that the resonant frequency is located at 2.72 GHz. Since the fabrication process includes physical limitations such as under cutting of the copper in the etching process and errors in alignment, the frequency shift between the computer

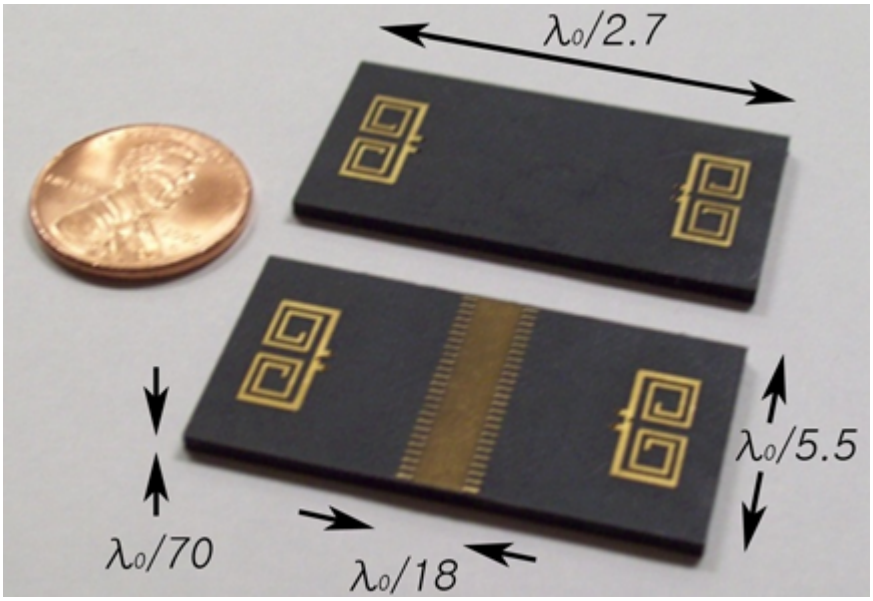

Figure 3.14: Prototype of the subwavelength radio repeater with and without the metamaterial-based EBG channel isolator.

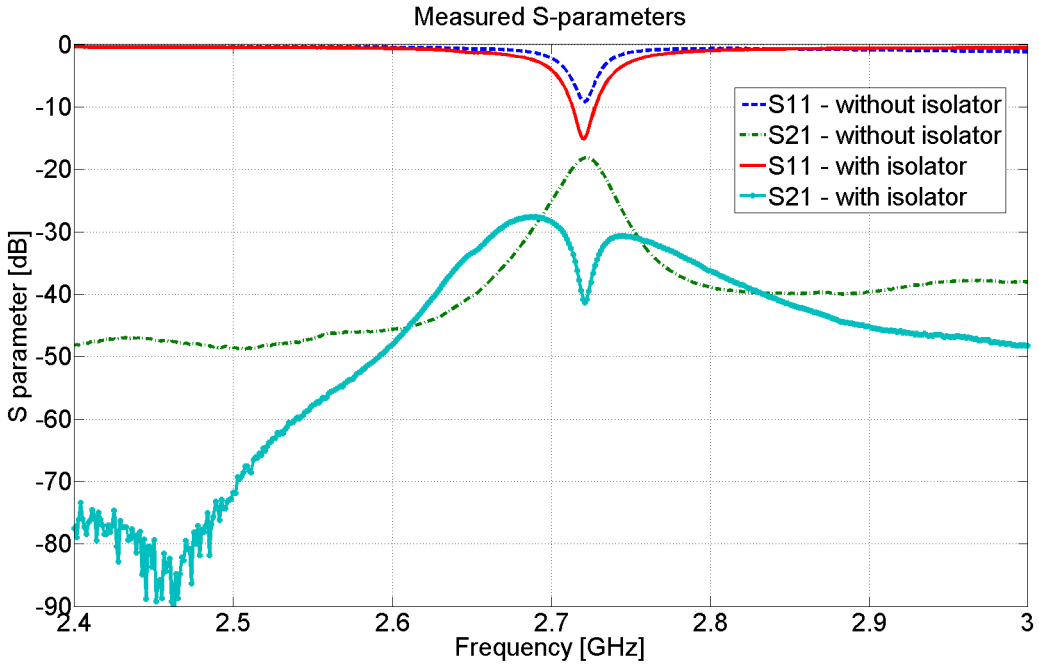

Figure 3.15: Measured S-parameters of the subwavelength repeater with and without the metamaterial-based EBG channel isolator.

based design and actual fabrication is unavoidable. However, this discrepancy can be corrected after a few trials. In addition, post tuning and optimization can be used to obtain the designed performance.

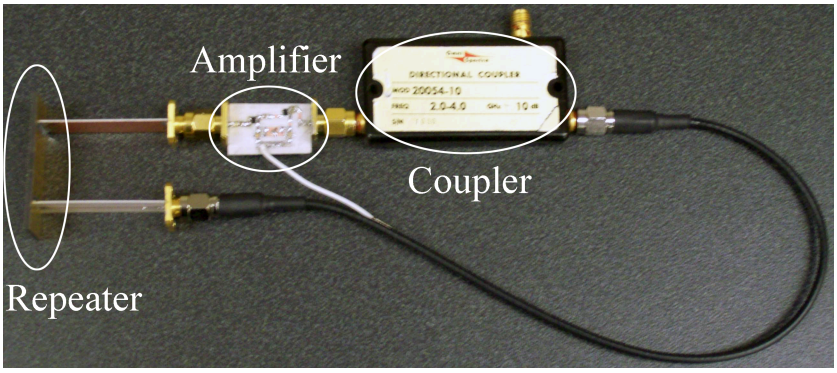

Figure 3.16: Measurement setup for operation validation of the subwavelength radio repeater.

Fig. 3.16 shows the system setup for the measuring of S-parameters. To feed each of antennas, two microstrip transmission lines are used where one is connected to an amplifier with variable gain and its output is connected to the other antenna through a directional coupler. The directional coupler is inserted between RF amplifier and transmit antenna to monitor the occurrence of oscillation when it happens as the gain is increased. As can be seen in Fig. 3.15, the repeater without the metamaterial-based EBG channel isolator shows a -18 dB of transmission coefficient, and the proposed repeater shows a -42 dB of transmission coefficient, which indicates 24 dB of suppression improvement. With the metamaterial-based EBG channel isolator, -28 dB of peak level of transmission coefficient (S_{21}) is observed, however, in spite of 1 dB of insertion loss from the directional coupler, a maximum gain of 32 dB for a wideband RF amplifier can be utilized with this repeater. Since the antennas are slightly mismatched near to the desired frequency (2.72 GHz), the maximum gain can be higher than the peak level of transmission coefficient (S_{21}). Therefore, it is verified that a commercial wideband RF amplifier with a gain of 32 dB can be integrated into the proposed repeater without oscillation.

3.6 Conclusions

In this chapter, a new concept for implementation of miniaturized radio repeater is presented. To construct the radio repeater, two miniaturized low-profile antennas ($\lambda_0/70$) radiating vertical polarization and a very thin metamaterial isolator layer are integrated into a compact configuration. The antennas are designed to have an omni-directional radiation pattern to make the repeater insensitive to the positions of the transmitter and receiver. In addition, the proposed isolator is shown to suppress the mutual coupling, improving the transmission coefficient from -18 dB to -42 dB. The dimensions of the Tx/Rx antenna and a unit cell of the isolator are 11.20 mm $\times$ 5.10 mm $\times$ 1.57 mm and 5.84 mm $\times$ 0.81 mm $\times$ 1.57 mm, respectively. The overall dimensions of the proposed radio repeater are 40.01 mm $\times$ 20.68 mm $\times$ 1.57 mm, which corresponds to $\lambda_0/2.75 \times \lambda_0/5.32 \times \lambda_0/70$. The proposed radio repeater system has been simulated and verified experimentally. A prototype of the design has been fabricated using printed circuit technology, which serves to reduce fabrication complexity and allows for easy commercial production at a large scale.

Such a radio repeater system can mitigate the adverse effects of obstacles in radio connectivity for ad-hoc networks in complex environments.

CHAPTER IV

Near-field Cancellation Technique based Radio Repeater Architecture

4.1 Introduction

In complex channel environments such as urban canyons and building interiors, the communication range is mainly restricted by the exorbitant path-loss between the two communication nodes. In indoor propagation scenarios obstacles such as walls, ceilings, and furniture cause significant multiple reflections, scattering, and diffraction. In such environments, therefore, the communication inevitably depends on the multiple paths including reflections and diffractions. In the absence of line-of-sight (LOS) communication, the signal due to multi-path experiences fast fading, which can result in loss of connectivity even over short distances [3] and [4]. Traditionally higher transmit power and closer communication nodes have been suggested for ad-hoc networks to improve the path-loss and overcome the adverse effects of the multi-path communication. However, such methods are power inefficient, require many nodes, lead to low data rate due to the higher latency, and have the potential to cause unintended interference between neighboring nodes. In order to mitigate these problems and improve the wireless connectivity in complex environments, radio repeaters have been proposed as an alternative [5, 10, 12, 13, 14, 15].

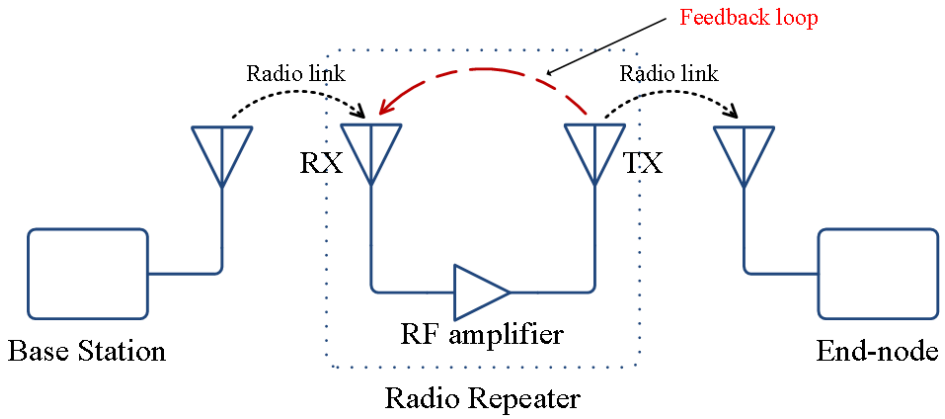

Figure 4.1: Schematic of radio link using a radio repeater.

As shown in Fig. 4.1, a simple radio repeater can be consisted of Receive antenna (Rx), Transmit antenna (Tx), and an amplifier circuitry. The received signal from the base station in the LOS is amplified and retransmitted to another repeater or the intended receive node that is in the LOS. Unlike repeaters in transmission lines or optical fibers, the mutual coupling between the Tx and Rx antennas intrinsically restricts the performance and physical dimensions of the radio repeater. Because of the positive feedback loop between the Tx and Rx antennas (due to the radiation and near-field effects), the gain of the radio repeater is limited by this level of mutual coupling. To avoid this intrinsic problem, Frequency Division Duplex (FDD) and Time Division Duplex (TDD) have been extensively investigated, and some are reported in [25, 26, 28]. These strategies rely on suppression of the mutual coupling by choosing two different frequencies or separating the signal in time domain for the up and down links, respectively. However, these methods increase the system complexity, cost, and power consumption. Recently a new concept for design of radio repeaters with a simple architecture was reported in [55]. This repeater utilizes two low-profile miniaturized antennas and a subwavelength metamaterial isolator to suppress the substrate mode and achieves an isolation in excess of 28 dB in a very small volume. As reported, the drawbacks of this repeater are low isolation and poor antenna efficiency. In a recent study it was shown that the overall repeater gain (product of

antenna and amplifier gains) of more than 35 dB is required for the repeater signal to overcome the multi-path signal in an indoor environment [24].

In this chapter, a new concept for suppression of signal leakage between the Tx and Rx antennas is proposed and implemented. By utilizing a two-element antenna array for the transmitter fed by a modified hybrid ring coupler, an electromagnetic null-plane is generated at the receiver location to reduce the mutual coupling drastically. The proposed radio repeater with a symmetric architecture is numerically analyzed, and its performance is experimentally verified. A prototype is fabricated using printed circuit technology on a commercially available dielectric substrate. The measurements show that the proposed repeater can boost the received signal by 50 dB and consequently has a radar cross section (RCS) value of 21.3 dBsm. This corresponds to the RCS of an equivalent metallic sphere having a diameter equal to 13.1 m. The proposed radio repeater utilizes miniaturized antennas capable of pure vertically polarized radiation pattern and 50 dB gain of cascaded RF amplifier. Antennas, RF circuitry, and DC power stage are fully integrated and packaged into a small size of 85.39 mm $\times$ 39.67 mm $\times$ 3.48 mm.

4.2 Design Specification for Miniaturized High-gain Radio Repeater

4.2.1 High-gain Miniaturized Planar Antenna

It is well known that for near-ground propagation scenarios vertically polarized waves experience less path-loss than horizontally polarized waves [66]. For this purpose radio repeaters considered here are equipped with antennas having vertical polarization while minimizing their height and lateral dimensions.

According to antenna theory, the gain of an antenna is proportional to its directivity and radiation efficiency. For small antennas, the antenna gain is mainly

determined by the radiation efficiency which relates to the conductor and dielectric losses. A low-profile miniaturized antenna with vertical polarization based on a quarter-wavelength microstrip resonator is reported in [55]. Although the reported multi-element monopole antenna (MMA) is capable of emanating omni-directional and vertical radiation pattern, its gain is limited by its poor radiation efficiency (about -9 dBi). Since the overall repeater system gain is proportional to the product of the Tx and Rx antenna gains, the antenna gain should be improved in the effort for increasing the repeater gain. One convenient way is to increase the height of the antenna. Because the vertical polarization mainly comes from the vertical current along the shorting pins, the antenna gain can be improved by simply extending the height of the shorting pins. However, it should be noted that the higher thickness of the substrate causes the stronger substrate mode, and consequently the higher mutual coupling between the antennas embedded in the same substrate. Increasing the height of the antenna from 1.57 mm (previous MMA design shown in Fig. 4.2 [55]) to 3.18 mm, the antenna gain is increased from -9 dBi to -4 dBi in the antenna H-plane. However, this value of gain is still too low and will degrade the overall repeater gain.

Another idea for increasing the antenna gain and bandwidth is to reduce the stored electromagnetic energy and the conductor loss. These are mainly influenced by an electric current distribution over the metallic traces of the MMA. Due to shallow skin depth and fringing field effects at high frequency, the narrow width of the strips and the sharp edges at the corners contribute to the observed exorbitant ohmic loss. To alleviate the ohmic loss, the electric current must be distributed over wider strips, and the sharp edges be removed as shown in Fig. 4.3. As can be seen, the wide width of the metallic strips evenly distributes the electric current. In addition, the round corners minimize the current density and strong electric and magnetic fields around the corners. As a result, the overall intensity of the electric current over the traces is reduced down to 10% of the previous design. This reduction of the conducting

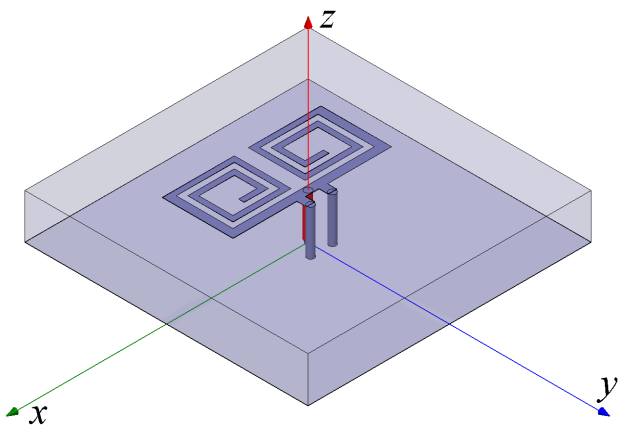

(a)

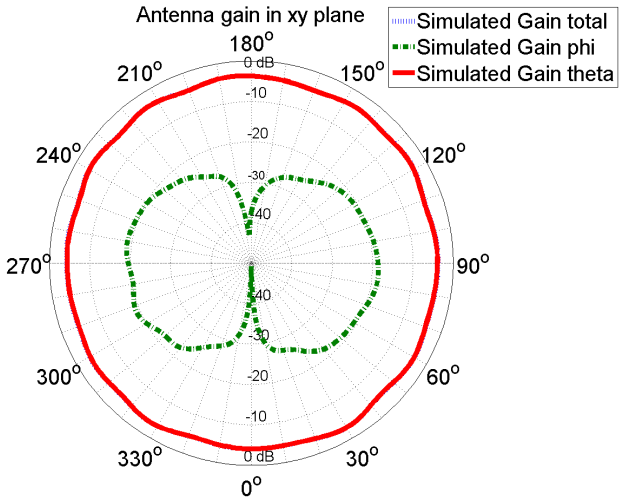

(b)

Figure 4.2: Modified planar multi-element monopole antenna: (a) geometry of the modified planar MMA; (b) simulated antenna gain in H(xy)-plane.

loss and stored energy results in improvement of the antenna gain and bandwidth. As indicated in Fig. 4.4, the new miniaturized planar antenna shows good matching at the designed frequency and higher gain (-1 dBi) in the H-plane. This indicates that 6 dB of gain enhancement for the overall repeater system is achieved from the higher gain of the modified antennas. The physical design parameters are optimized for operation around 2.46 GHz and summarized in Table 4.1.

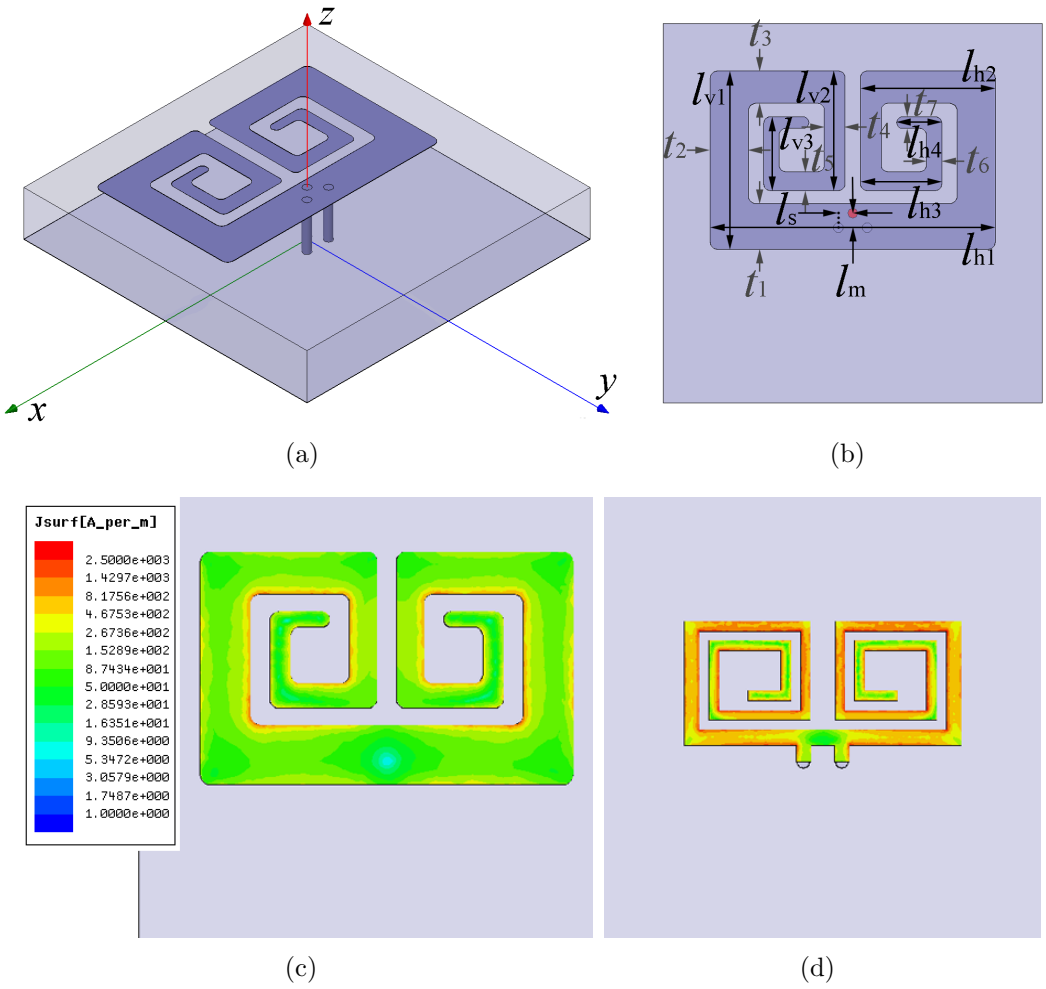

Figure 4.3: High-gain transmit antenna: (a) geometry of the high-gain Tx antenna; (b) design parameters; (c) simulated current distribution of the high-gain Tx antenna; (d) simulated current distribution of the modified planar MMA.

Table 4.1: Design parameters of the redesigned transmit antenna

l_{h1}	l_{h2}	l_{h3}	l_{h4}	l_{v1}	l_{v2}	l_{v3}
15.04 mm	7.11 mm	4.29 mm	2.39 mm	9.40 mm	6.30 mm	3.89 mm

t_1	t_2	t_3	t_4	t_5	t_6	t_7
2.41 mm	2.01 mm	1.70 mm	1.09 mm	0.99 mm	0.81 mm	0.61 mm

l_m	l_s
0.76 mm	0.76 mm

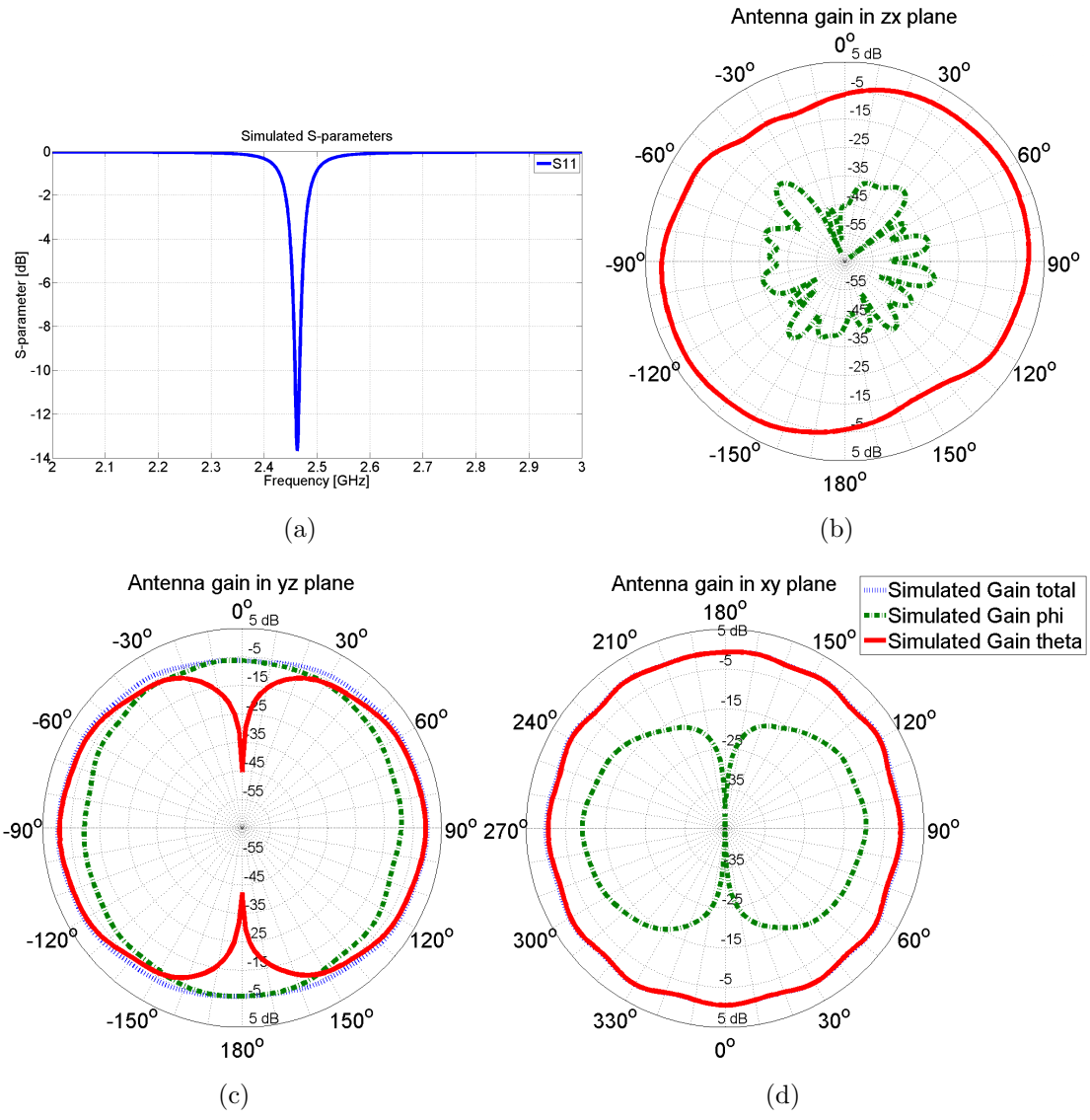

Figure 4.4: Simulated responses of the high-gain Tx antenna: (a) input reflection coefficient; (b) radiation pattern in E(zx)-plane; (c) radiation pattern in E(yz)-plane; (d) radiation pattern in H(xy)-plane.

4.2.2 Transmit-Receive Antenna Isolation

As mentioned before, the mutual coupling between the Tx and Rx antennas is the most critical factor that limits the maximum achievable repeater gain. Various approaches have been suggested and studied to suppress the mutual coupling in [48, 50, 34, 53, 55]. The mushroom type of metamaterial structure and electromagnetic band-gap (EBG) structure are commonly proposed and demonstrated in [48] and [50]. However, the metamaterial-based approaches inevitably require periodic structures and consequently large physical dimensions. Although, the magneto-dielectric embedded-circuit based method in [53] can be adapted in a small system dimension, its coupling suppression is narrow-band and limited by the quality (Q) factor of the resonant EBG loops. With a finite Q factor, it was reported that the printed EBG structure can suppress the peak level of transmission coefficient (S_{21}) from -18 dB to -28 dB in [55].

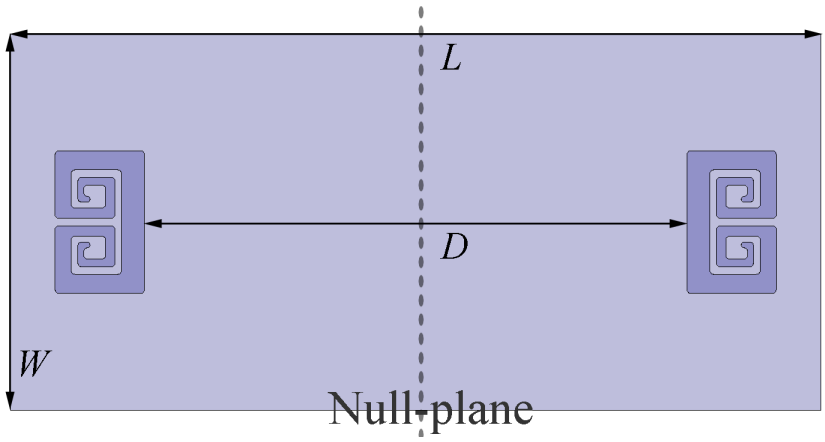

Figure 4.5: Design parameters of the high-gain Tx antenna array

In order to achieve further suppression of the mutual coupling, a new concept based on generating a null-plane from a symmetric and out of phase pair of Tx antennas is suggested. Feeding two antennas by signals having the same amplitude but 180° out of phase, the resulting E-field will vanish in the perpendicular bisect-plane of the substrate on which the antennas are built. As shown in Fig. 4.5, the Tx

antennas are positioned on the substrate in a symmetric manner.

If the receiver has a plane of symmetry that coincides with the perpendicular bisect-plane, the received voltage due to the mutual coupling will be zero. In this configuration, the null-plane exists independent of the separation between the two elements of the Tx antenna array. However, if the two antennas are too close to each other, the transmit antenna gain will drop due to far-field cancellation. To avoid such cancellation in the far-field, the Tx antennas can be separated by $\lambda_0/2$ in which case the fields add up coherently in the far-field in the end-fire directions. In these directions the field is doubled, and the transmitter gain is increased by 6 dB. The antenna gain drops gradually as a function of angle towards the null-plane. To maximize the antenna gain, the distance D between the two Tx antennas is set to 57.15 mm. The width W and length L of the substrate are optimized to 39.67 mm and 85.39 mm, respectively. The optimized Tx array and its simulated radiation patterns are shown in Fig. 4.6. As expected, an electric null-plane is generated at the symmetric plane. It should be noted that since the power is split into two ways the overall repeater gain will be increased by 3 dB in the end-fire directions in the H-plane. As shown in Fig. 4.6(d), the half-power beamwidth of such array is very wide (more than 80° in each of the end-fire lobes).

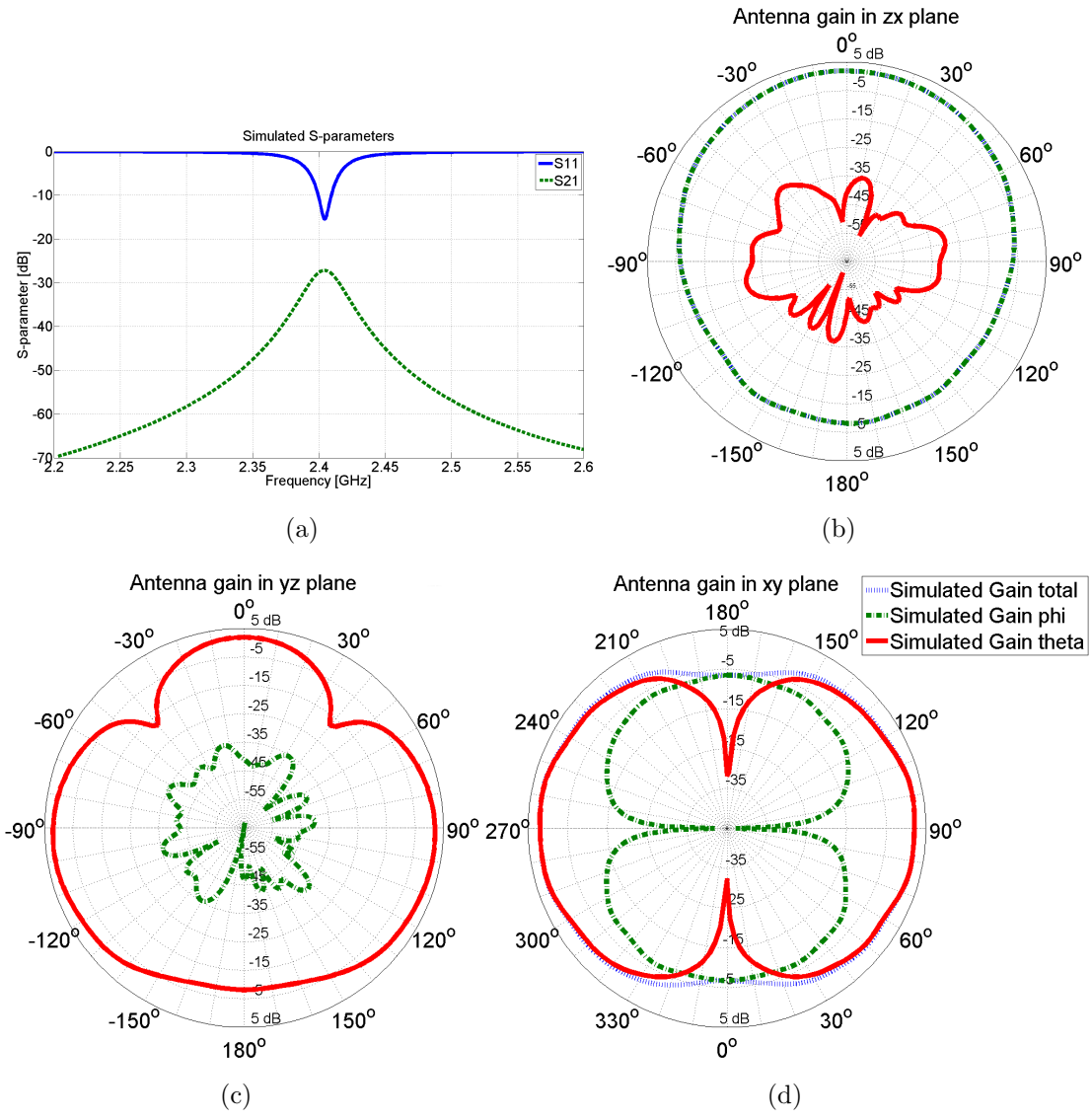

(a) (b)

(c) (d)

Figure 4.6: Simulated responses of the high-gain Tx antenna array: (a) input reflection coefficient; (b) radiation pattern in E(zx)- plane; (c) radiation pattern in E(yz)-plane; (d) radiation pattern in H(xy)-plane.

4.2.3 Receive Antenna

As presented in Section 4.2.2, the Rx antenna should also operate with vertical polarization and have a plane of symmetry to be placed in the null-plane of the Tx array. The antenna feed must be in the plane of symmetry and in the null-plane. This way the retransmitted signal from the Tx array will induce the electric currents in the opposite directions over the symmetric arms of the Rx antenna. As a result, the induced current on the Rx feed will be zero, and the desired isolation can be achieved as shown in Fig. 4.7. A topology similar to the Tx antenna can be considered. To create a symmetric geometry, the topology of the Tx antenna is imaged about its longer direction as shown in Fig. 4.8(a). However, the locations of the shorting pins and feed point are modified. Basically the feed is placed in the plane of symmetry, and the shorting pins are also placed in a symmetric fashion with respect to the feeding pin and the plane of symmetry. This is shown more clearly in Fig. 4.8(b). In this figure design parameters that influence the antenna characteristics such as the resonant frequency, input impedance, bandwidth, and antenna efficiency are also described.

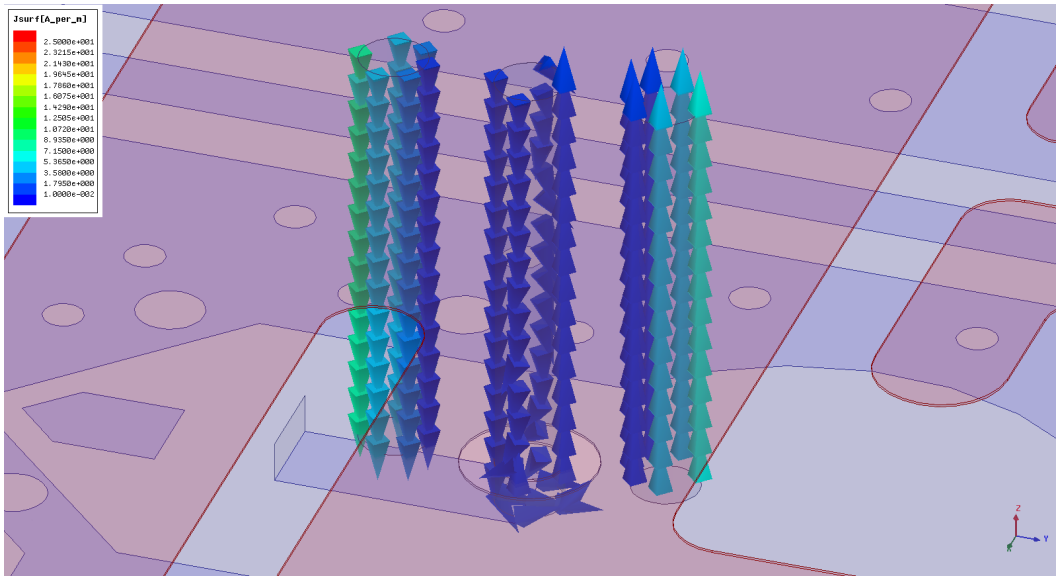

Figure 4.7: Simulated current distribution on the vertical pins of the high-gain receive antenna.

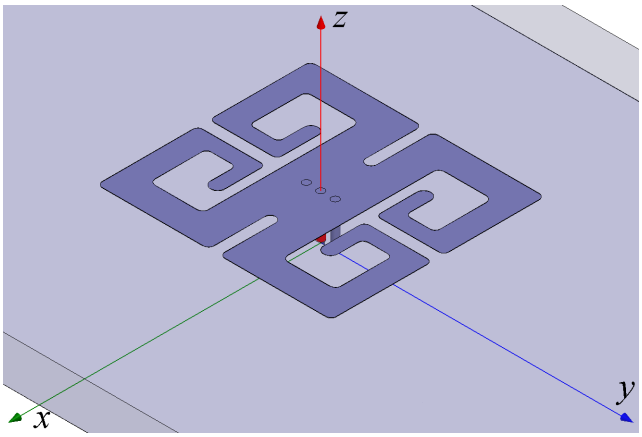

(a)

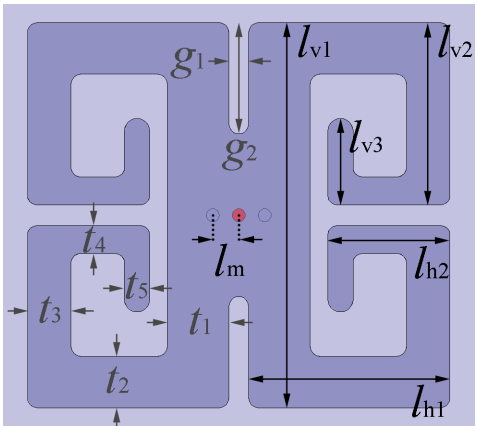

(b)

Figure 4.8: High-gain receive antenna: (a) geometry of the high-gain Rx antenna; (b) design parameters.

Each arm of the four-arm MMA is approximately quarter-wavelength long which produces a strong electric current through the shorting pins. This in turn results in a purely vertical polarization radiation pattern. As the Rx antenna occupies the larger volume and surface area, it shows the higher gain and bandwidth compared to the Tx antenna. The input reflection coefficient and radiation patterns of the Rx antenna are shown in Fig. 4.9. The numerically simulated vertical gain and bandwidth are shown to be -1.3 dBi in the H-plane and 15 MHz, respectively. The omni-directional and vertical polarization enables the repeater to receive the signal regardless of the location of the base station. The physical design parameters are

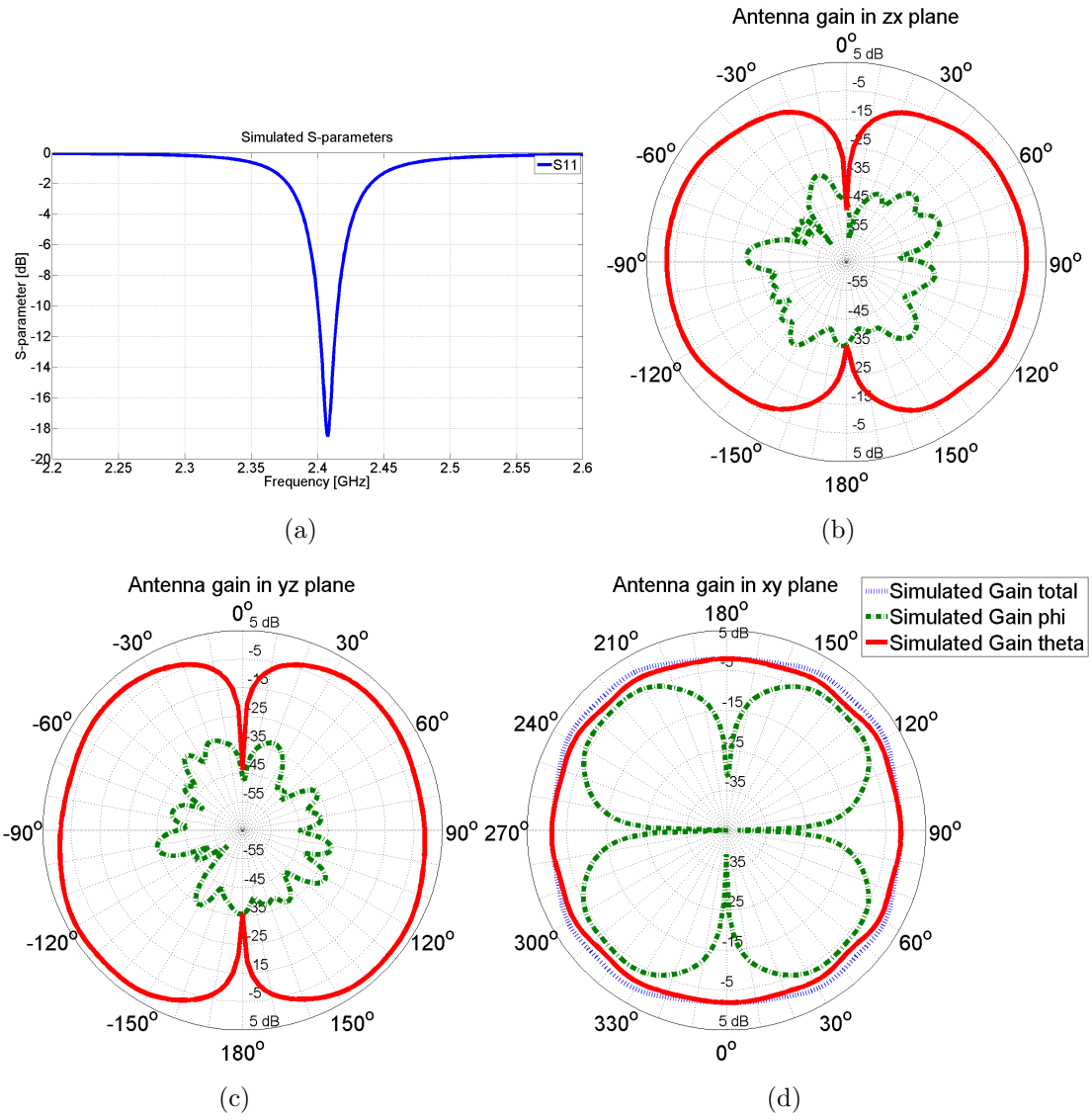

Figure 4.9: Simulated responses of the high-gain Rx antenna: (a) input reflection coefficient; (b) radiation pattern in E(zx)-plane; (c) radiation pattern in E(yz)-plane; (d) radiation pattern in H(xy)-plane.

optimized for operation around 2.41 GHz and summarized in Table 4.2.

Table 4.2: Design parameters of the redesigned receive antenna

l_{h1}	l_{h2}	l_{v1}	l_{v2}	g_1	g_2
7.87 mm	4.78 mm	7.11 mm	3.37 mm	0.76 mm	4.34 mm
l_m	t_1	t_2	t_3	t_4	t_5
1.02 mm	2.41 mm	2.01 mm	1.70 mm	1.09 mm	0.99 mm

4.2.4 Modified Hybrid Ring Coupler

In Section 4.2.2, the concept of repeater isolation based on the symmetric cancellation was described. In order to generate two signals with the same amplitude and 180° out of phase, a conventional hybrid ring coupler can be utilized. The hybrid ring coupler consists of sum and difference input ports and two output ports as shown in [68]. By exciting only the difference input port and terminating the sum input port, two outputs can be produced with the same amplitude and 180° phase difference. To be integrated into the proposed radio repeater system with a limited space, the geometry of the conventional hybrid ring coupler is modified and optimized as shown in Fig. 4.10(a). Since a cascaded RF amplifier is incorporated, any parasitic effects from its circuit layout should be considered in the design of the ring coupler as well. The modified hybrid ring coupler with sharp corners and an embedded circuit layout for the RF amplifier is designed and verified using a commercial finite element method solver (Ansoft's HFSS ver. 12.1). With some optimization, the physical parameters are designed so that the coupler can operate around the desired frequency (2.41 GHz). The design parameters are summarized in Table 4.3. As can be seen in Fig. 4.10(b), the modified hybrid ring coupler produces two signals within 0.01 dB of variation in amplitude and less than 0.05° in phase. As indicated, the vector sum of two outputs shows extremely small value at the desired frequency of 2.41 GHz (-40 dB bandwidth of 65 MHz).

Table 4.3: Design parameters of the modified hybrid ring coupler

L	H	w_1	w_2
38.21 mm	20.14 mm	0.37 mm	0.68 mm

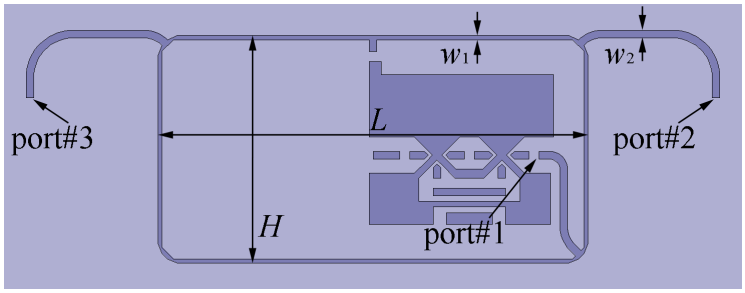

(a)

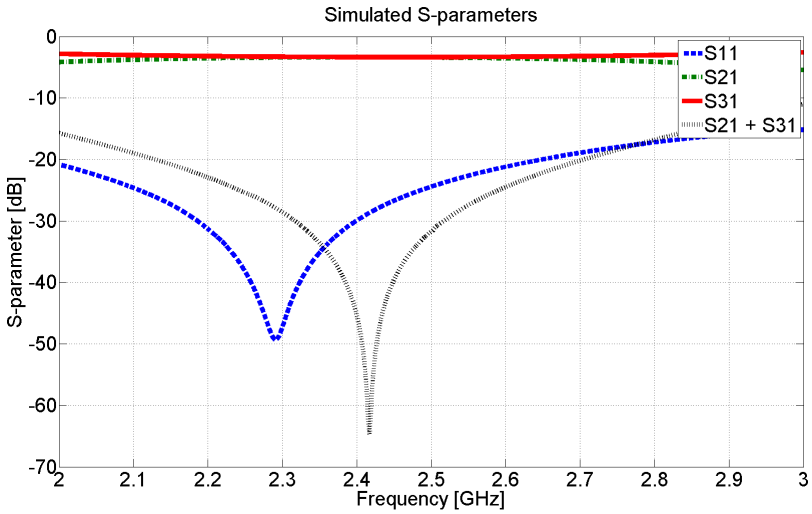

(b)

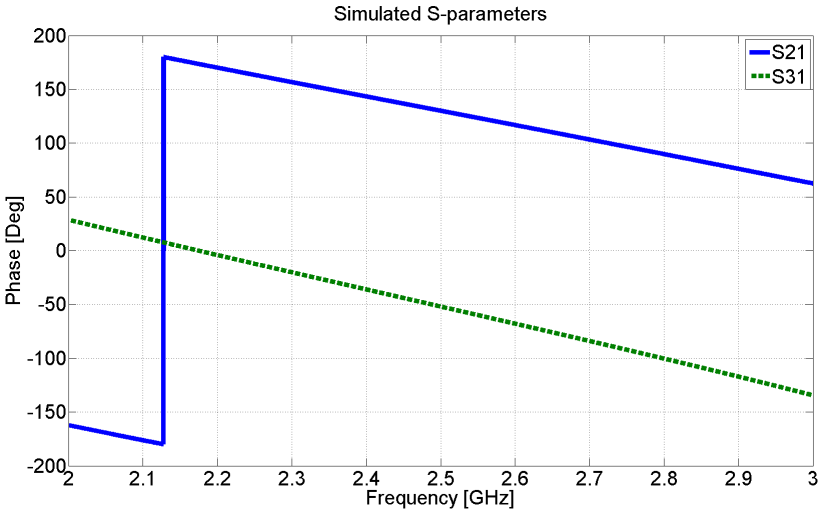

(c)

Figure 4.10: Modified hybrid ring coupler: (a) geometry of the modified hybrid ring coupler; (b) simulated S-parameters; (c) phase responses of two outputs.

4.3 Numerical Simulation Results

4.3.1 Full-wave Simulation of the Miniaturized High-gain Radio Repeater

In Section 4.2, the specific design objective and the principle of operation were discussed. All of the sub-components such as Tx array, Rx, hybrid ring coupler, and the circuit layout for the RF amplifier are integrated as shown in Fig. 4.11(a). In order to take any potential interactions between all sub-components into account, the overall repeater system is further optimized and verified using Ansoft's HFSS. As shown in Fig. 4.11(b), the proposed symmetric cancellation method can suppress the mutual coupling between the Tx and Rx antennas down to -86 dB at the design frequency. Based on the bandwidth of the RF amplifier, the peak level of transmission coefficient (S_{21}) should be considered to set the active gain of the proposed repeater. From the simulated responses, the RF amplifier is configured to 50 dB of gain.

Fig. 4.12 and Fig. 4.13 show the magnitude of the electric near-field and far-field radiation patterns for the vertical polarization when the Tx or Rx antenna is separately excited. As expected, in Tx mode the near fields are perfectly symmetric, and the electric null-plane is generated along the symmetric plane in which the Rx antenna resides. Furthermore, the far-field radiation pattern shows that the proposed radio repeater has wider beamwidth. In Rx mode the designed repeater shows a desired omni-directional radiation pattern.

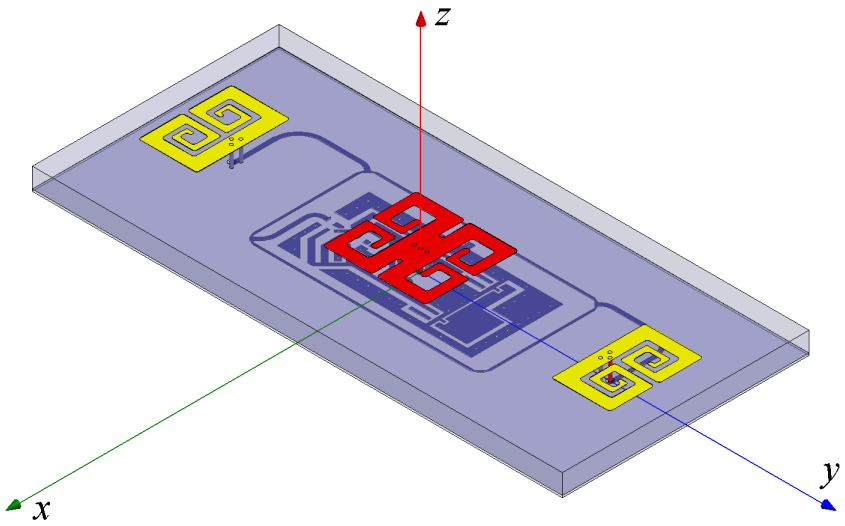

(a)

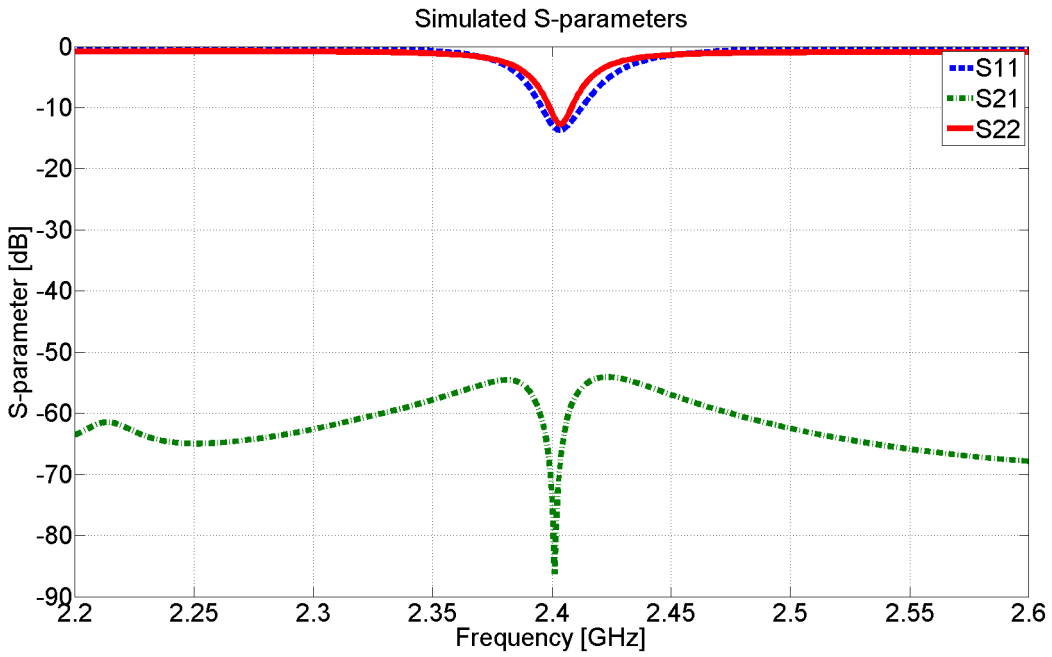

(b)

Figure 4.11: Miniaturized high-gain radio repeater: (a) geometry of the miniaturized high-gain radio repeater; (b) simulated S-parameters.

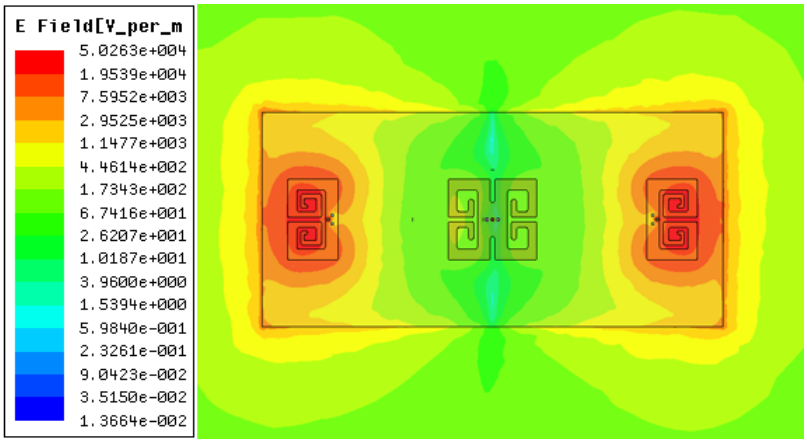

(a)

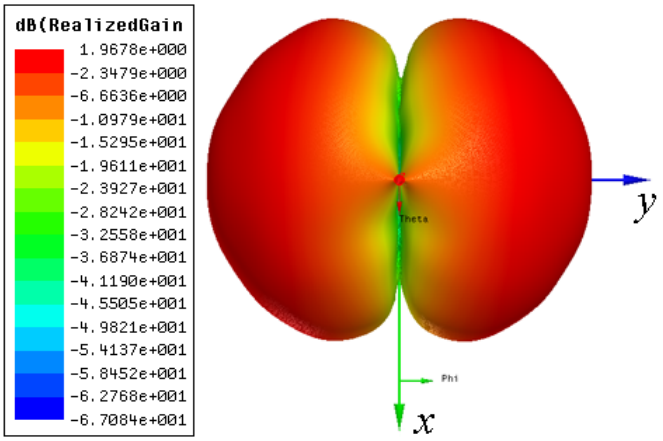

(b)

Figure 4.12: Simulated field profiles in Tx mode: (a) near E-field distribution; (b) E-field radiation pattern in H(xy)-plane.

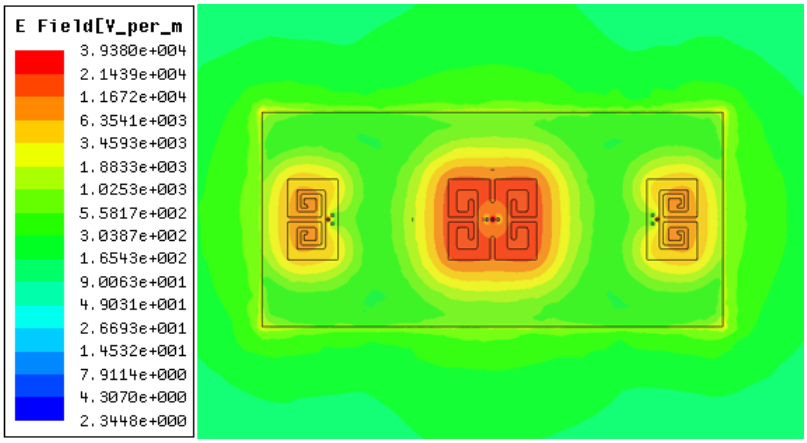

(a)

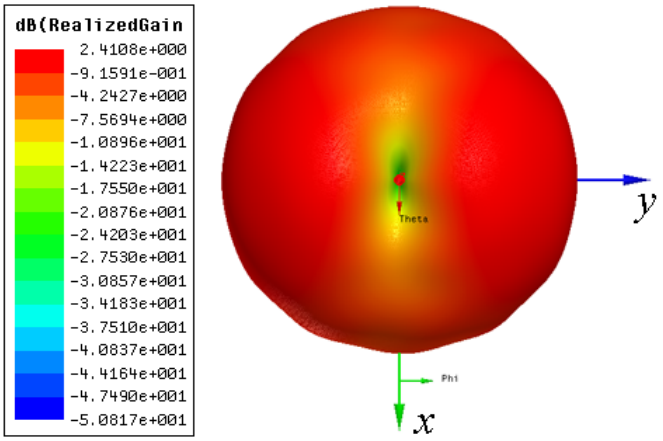

(b)

Figure 4.13: Simulated field profiles in Rx mode: (a) near E-field distribution; (b) E-field radiation pattern in H(xy)-plane.

4.3.2 Repeater Radar Cross Section

The repeater measurement of the overall system gain cannot be done using a network analyzer, as the connecting cables and the instrument can perturb the near fields and establish additional couplings between the Tx and Rx antennas. Also the antenna gains must be measured in the far-field. Hence, the overall repeater gain must be characterized in a different fashion. The best way is through the measurement of the RCS of the repeater when the repeater is placed in isolation and the far-field region. The radio repeater can be viewed as a transponder which can retransmit the received RF signal. The received RF signal by the radio repeater can be considered as an incident field and the retransmitted RF signal as a scattered field from the radio repeater. Thus, the RCS of the radio repeater can be easily calculated using Friis transmission formula.

Without loss of generality, suppose a monostatic radar utilized for the measurement of the repeater's RCS has an isotropic vertically polarized antenna and its output power is P_{t}. Then, the intensity of the received RF signal by the radio repeater can be expressed as

$$P_{\mathrm{r}} = W_{\mathrm{t}} A_{\mathrm{eff}} = \frac{P_{\mathrm{t}}}{4\pi R^2} A_{\mathrm{eff}} \tag{4.1}$$

where W_{t} is the power density at the repeater, $A_{\mathrm{eff}} = \frac{\lambda_0^2}{4\pi} G_{\mathrm{r}}$ is the effective aperture of the repeater Rx antenna, G_{r} is the gain of the repeater Rx antenna, and R is the distance between the repeater and the radar. Since the repeater has an active gain G_{repeater}, the power density of the retransmitted RF signal at the radar receiver is

$$W_{\mathrm{s}} = \frac{P_{\mathrm{s}}}{4\pi R^2} = \frac{P_{\mathrm{r}} G_{\mathrm{repeater}} G_{\mathrm{t}}}{4\pi R^2} \tag{4.2}$$

where P_{s} is the power intensity of the retransmitted RF signal by the repeater, and G_{t} is the gain of the repeater Tx antenna. Hence, the RCS of the repeater is given

by

$$\sigma_{\text{repeater}} = \lim_{R\to\infty}[4\pi R^2 \frac{W_{\text{s}}}{W_{\text{t}}}] = \frac{\lambda_0^2}{4\pi} G_{\text{r}} G_{\text{repeater}} G_{\text{t}} \tag{4.3}$$

In order to calibrate the monostatic radar system, background subtraction method is performed, and a target with known RCS is measured and compared with the measured signal from the repeater. For this purpose, a 0.36 m diameter metallic sphere is utilized. The approximate (assuming $a \gg \lambda_0$) RCS of a metallic sphere is given by

$$\sigma_{\text{sphere}} = \pi a^2 \tag{4.4}$$

where a is the radius of the sphere. From (4.3) and (4.4), the diameter of an equivalent metallic sphere having the same RCS as the repeater also can be calculated.

4.4 System Integration and Experimental Results

A prototype of the proposed radio repeater is fabricated using 3.18 mm-thick Rogers RT/duriod 5880 substrate ($\varepsilon_{\text{r}} = 2.2$) as shown in Fig. 4.14. As shown, the top side of the substrate accommodates the Tx array and Rx antennas. At the backside a very thin substrate includes the hybrid ring coupler, the RF amplifier, and the DC bias circuitry. Furthermore, a small commercial Lithium-Polymer cell is incorporated at the backside for furnishing power over an extended period of time. To obtain the required gain and output power while maintaining low-power consumption, a cascaded RF amplifier composed of a high-gain (20 dB) low-noise and low-power amplifier (μPC8182TB made by NEC) and a moderate power (20 dBm) and high-gain (30 dB) amplifier (μPG2250T5N made by NEC) are integrated into the system. The total gain of the cascaded RF amplifier can be adjusted by controlling the DC bias voltage. To provide an adjustable DC bias, a power efficient voltage regulator

(MAX8892 made by MAXIM) is utilized. At a bias voltage of 3 V, the two stages of RF amplifiers are measured to provide 50 dB of gain and draw 80 mA.

(a) (b)

Figure 4.14: Prototype of the miniaturized high-gain radio repeater: (a) high-gain Tx antenna array and high-gain Rx antenna; (b) RF amplifier and modified hybrid ring coupler.

As an initial test of the radio repeater system including the hybrid ring coupler, the two-port S-parameters of the antennas are measured by connecting coaxial cables to the Rx antenna and the input port of the ring coupler. The measured S-parameters are shown in Fig. 4.15, where a good input impedance matching for the Rx antenna and the Tx antenna array is observed. A minimum isolation of about 40 dB is also observed. It is noted that this is the worst case scenario as the asymmetric placement of coaxial cables in the near-field of the antennas perturbs the symmetry and creates more than expected cross-talk. To avoid such difficulties in the measurement of the mutual coupling, the repeater is characterized in the far-field using a radar system in backscatter mode. In this approach the repeater backscattering RCS is measured with different amplifier gain values while its oscillation is monitored using a spectrum analyzer. No oscillation occurs for the maximum gain value of 50 dB. Fig. 4.16 shows the repeater in the anechoic chamber of The University of Michigan.

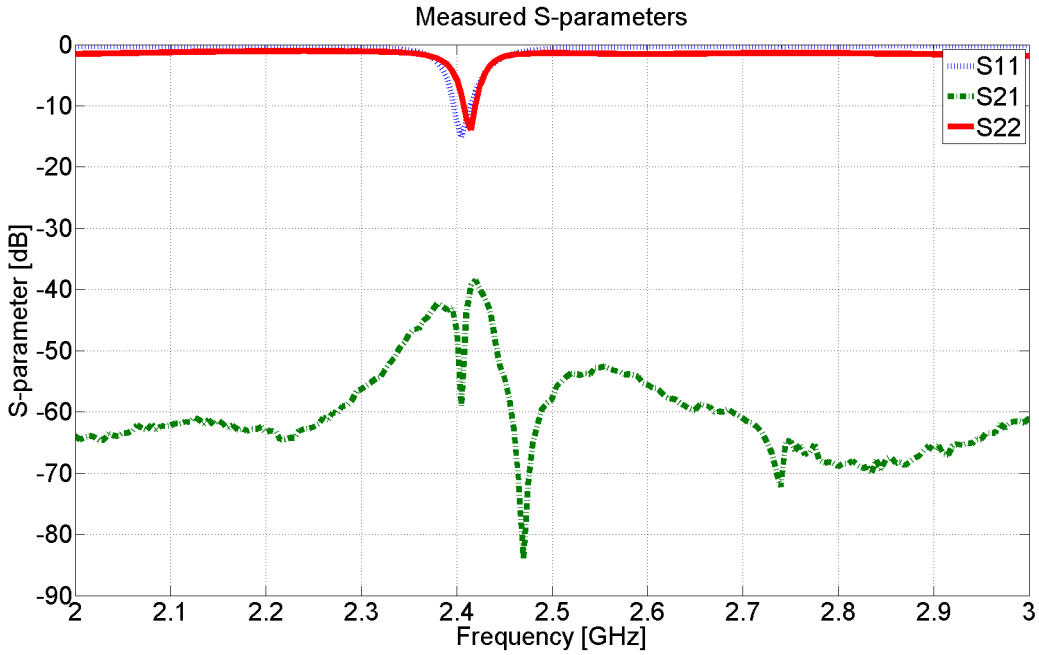

Figure 4.15: Measured S-parameters of the miniaturized high-gain radio repeater

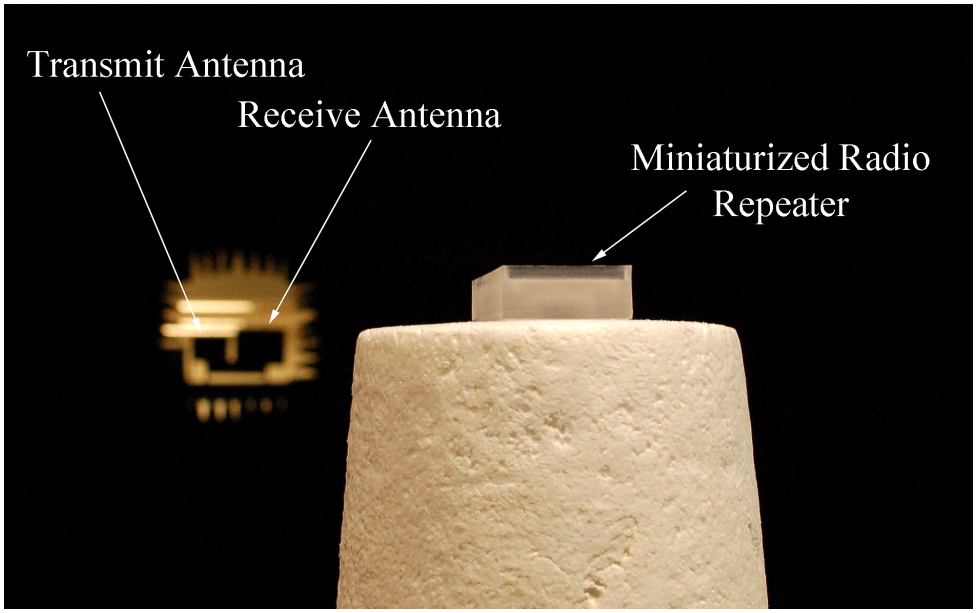

Figure 4.16: Monostatic radar cross section measurement setup

Fig. 4.17(a) shows the radar outputs as a function of frequency for both the repeater and a 0.36 m diameter sphere. At the operating frequency (2.43 GHz) the measured repeater RCS is 31.3 dB higher than the sphere, which corresponds to an RCS value of 21.3 dBsm. This value corresponds to the RCS of a 13.1 m diameter metallic sphere. In addition, the far-field RCS pattern at VV (vertical scattered and vertical incident) polarization is also measured and shown in Fig. 4.17(b). As mentioned before, the proposed repeater shows the electric null-plane along the symmetric plane and a 3 dB beamwidth of about 80° in the H-plane.

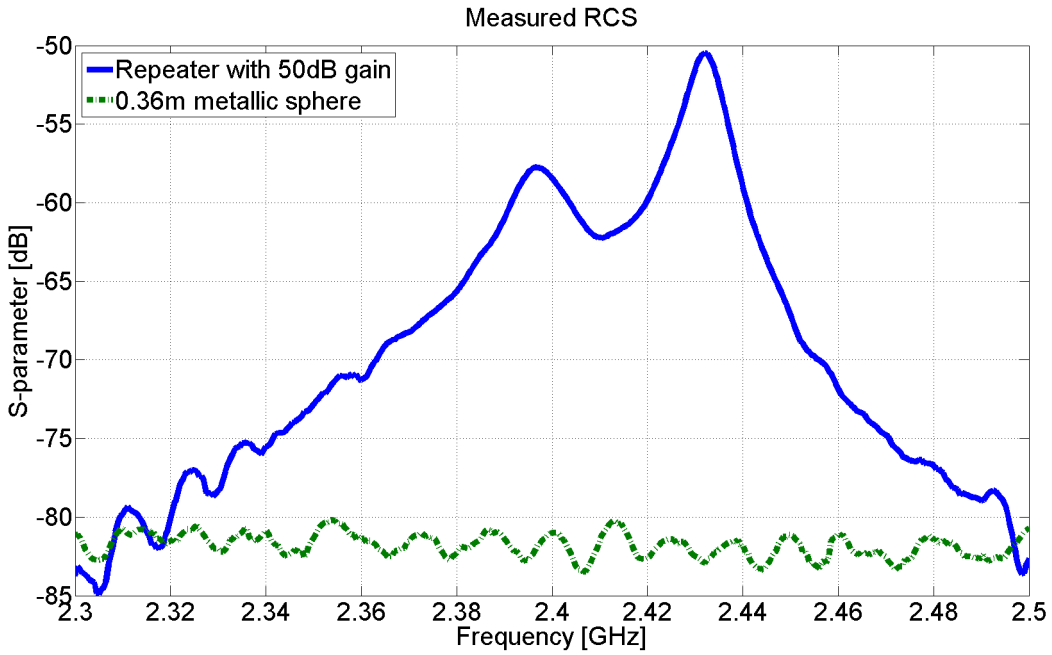

(a)

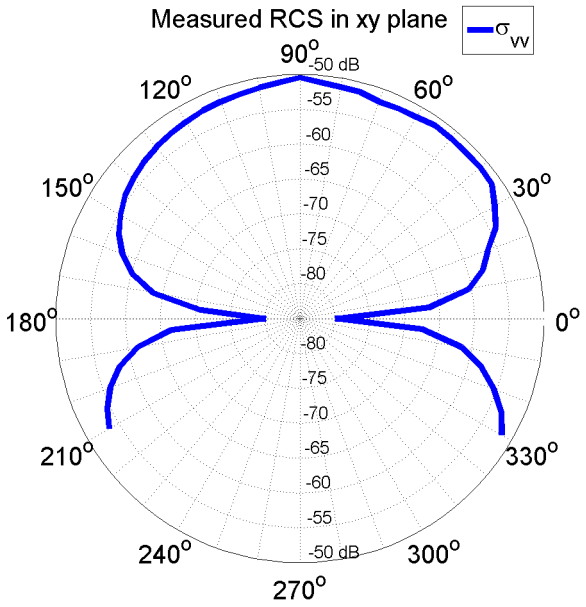

(b)

Figure 4.17: Measured radar outputs: (a) measured radar output in the end-fire direction; (b) measured radar output pattern in H(xy)-plane.

4.5 Conclusions

In this chapter, a novel concept for development of a high-gain and miniaturized radio repeater is presented. The repeater system is composed of miniaturized low-profile planar antennas ($\lambda_0/39$) radiating vertical polarization, a modified hybrid ring coupler for feed the Tx antenna array, and a low-power high-gain amplifier chain, which are integrated into a compact configuration. The Rx antenna is designed to show an omni-directional radiation pattern. The Tx array is composed of two elements, which are designed to maximize the directivity of vertical radiation pattern in the end-fire directions and minimize the mutual coupling to the Rx antenna. The near-field cancellation is accomplished using the modified hybrid ring coupler, which feeds the Tx array with equal amplitude and 180° out of phase to generate a null-plane in the middle of the Tx array where the Rx antenna is placed. As a result, the proposed radio repeater is shown to suppress the mutual coupling down to -54 dB over the entire frequency band. The proposed radio repeater is fully integrated including a DC bias circuitry and battery. Its dimensions are 85.39 mm $\times$ 39.67 mm $\times$ 3.48 mm, which corresponds to $\lambda_0/1.45 \times \lambda_0/3.11 \times \lambda_0/35.48$. The proposed radio repeater system has been evaluated and verified both numerically and experimentally.

CHAPTER V

Simultaneous Dual-channel Radio Repeater Architecture

5.1 Introduction

Radio repeaters have been introduced to enhance the signal coverage and radio connectivity in complex propagation environment with strong signal attenuation and multi-path and in the absence of line-of-sight between transmitter and receiver [6, 7, 8, 9, 18]. Radio repeaters often useful for power constrained ad-hoc communications [24]. By amplifying and retransmitting the received RF signal, the radio repeater can reestablish line-of-sight communication in a complex channel environment if the repeater is in the direct view of both the transmitter and receiver. As a result, the radio repeater promises to extend the communication range and mitigate adverse effects of multi-path communication such as fading effect and exorbitant path-loss. Most radio repeaters down-convert the signal, amplify and up-convert and retransmit it at a different frequency [26, 27]. This way, the adjacent transmit (Tx) and receive (Rx) antennas are isolated. Such repeaters require substantial amount of power and often time require a communication protocol to handle multiple channels. For power limited systems simplified repeaters with only few low-power components are envisioned [55]. Such system simply includes the Tx and Rx antennas as well

as a low-power high-gain RF amplifier. One practical limitation in miniaturizing the physical dimensions and complexity of the radio repeater system, however, is the near-field mutual coupling between the Tx and Rx antennas. This coupling creates a positive feedback and limits the system performance. Due to this intrinsic feedback loop, the gain of the RF amplifier in the repeater system should be restricted in order to prevent the system self oscillation.

In order to decrease the mutual coupling between closely spaced antennas, numerous approaches have been studied and proposed in [34, 38, 39, 40]. Generally speaking, these methods achieve the suppression of the mutual coupling by modifying the current distribution on the ground plane. Although the defected ground structure (DGS) and the artificial current paths improve the isolation between adjacent antennas to some extent, these methods cause the degradation of radiation polarization and pattern. In addition to manipulating the current distribution, artificial electromagnetic structures such as metamaterial electromagnetic band-gap (EBG) structures, which modify the effective material properties have been investigated and demonstrated in [44, 50, 51, 54]. By utilizing the negative effective permeability of the medium with particular resonant characteristics, these methods inhibit wave propagation within the effective medium. However, these artificial structures usually require periodic geometry and large dimensions, which are not suitable for the miniaturized subwavelength system.

Recently, a novel isolation technique utilizing the near-field cancellation has been reported in [56]. In this approach, an electromagnetic null-plane is generated and utilized to suppress the mutual coupling between closely spaced antennas. As a result, a dramatic size reduction of the radio repeater and performance improvement has been demonstrated. This miniaturized radio repeater is shown to have the ability of amplifying the received RF signal by more than 50 dB without going to oscillation. The overall repeater performance is characterized by measuring the Radar Cross

Section (RCS) of the repeater in backscatter direction. Calibrating the measured backscattering against that of a standard metallic sphere, the repeater showed an RCS value of 21.3 dBsm, while having a very small form factor.

In this chapter, a modified design is introduced to provide a simultaneous dual-channel micro-repeater system. Due to the existence of the intrinsic positive feedback loop in radio repeater systems, the open-loop system transfer function is designed to create a phase characteristic with two zero-crossing in the desired band of operation. This allows a closed-loop gain larger than the active RF amplifier gain at two frequencies. In this design, the overall complex closed-loop gain of the radio repeater consisting of the complex mutual coupling between the Tx and Rx antennas, the antenna feed network, and the RF amplifier must be considered. This closed-loop transfer function determines the stability of the system and the overall system gain, which can be verified through its RCS measurement.

In order to design a dual-channel radio repeater and allowing for the desired open-loop transfer function phase characteristic, the Tx and Rx antennas are redesigned to increase the antenna bandwidth. The antennas are based on the multi-element monopole antenna [67] with very low-profile and can radiate purely vertical polarization. Basically by utilizing parasitic elements through magnetic and electric couplings additional poles are introduced. This way, the redesigned antennas show the improved radiation efficiency and bandwidth while maintaining the vertical polarization. The modified antenna structures still maintain a very small form factors and location of the shorting pins are carefully chosen to ensure in-phase electric current distributions for enhanced far-field radiation and bandwidth. The proposed dual-channel radio repeater system employing the near-field cancellation technique is analyzed numerically, and its performance is characterized experimentally. A prototype of the proposed radio repeater shows dual-channel capability at 2.416 GHz and 2.444 GHz with more than 26.0 dBsm of RCS on both channels.

5.2 Closed-loop System Transfer Function

The miniaturized radio repeater system mainly consists of the Tx and Rx antennas and RF amplifier circuitry. In order to achieve the near-field cancellation, a modified hybrid ring coupler is designed as the feeding network for the Tx antenna array. By feeding two symmetric Tx antennas with the same magnitude but out-of-phase signals, an electromagnetic null-plane is generated at the symmetric plane, where the Rx antenna is placed in symmetric manner. Because the retransmitted signals from the Tx array induce electric currents with opposite directions on the arms of the Rx antenna, the total current at the feed of the Rx antenna is vanished. This results in a drastic suppression of the mutual coupling as reported in [56].

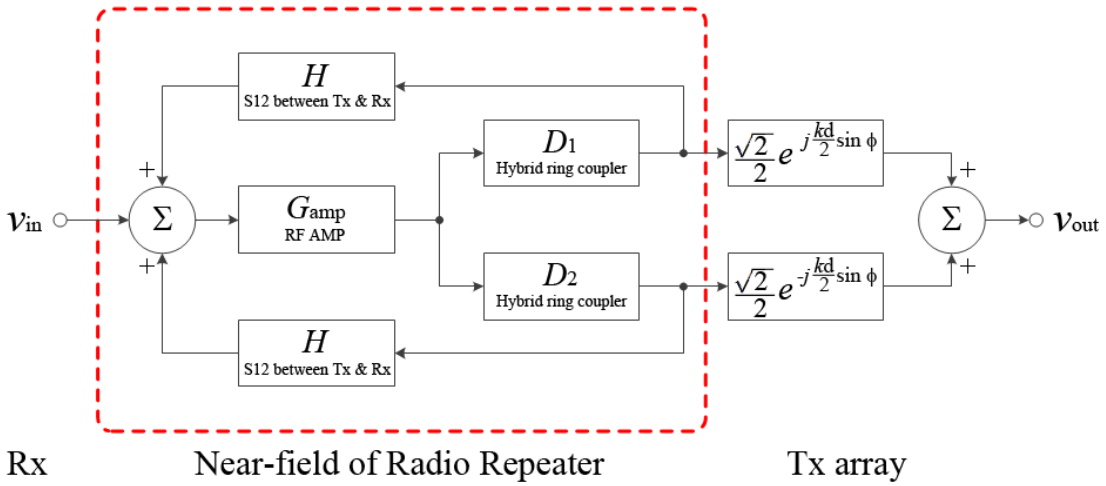

Figure 5.1: Block diagram of the radio repeater system utilizing the near-field cancellation technique.

Fig. 5.1 shows the system diagram of the near-field cancellation technique. As can be seen, the received RF signal v_{in} is amplified and separated into two signals to feed the two Tx elements. The two Tx array elements have access to receiver through substrate mode and air-field coupling. These are shown by symmetric feedback branches with complex frequency dependent transfer function denoted by H. The input signal couples from air and the two transmitted signals are also added in

air after experiencing a propagation phase shift depending on the observation angle ϕ. The overall closed-loop system transfer function $v_{\text{out}}/v_{\text{in}}$ can easily be computed and is given by

$$TF = \frac{\sqrt{2}}{2}\frac{D_1 e^{j\frac{kd}{2}\sin\phi} + D_2 e^{-j\frac{kd}{2}\sin\phi}}{1 - HG_{\text{amp}}(D_1 + D_2)}G_{\text{amp}} \tag{5.1}$$

where G_{amp} is the gain of the RF amplifier, H is the mutual coupling between one Tx antenna and Rx antenna without the modified hybrid ring coupler, and D_1 and D_2 are two output of the modified hybrid ring coupler. Here, k is the wave propagation constant, d $\simeq \lambda_0/2$ is the separation between the two Tx elements, and ϕ is the observation direction in the plane of the repeater. In (5.1), D_1, D_2, and G_{amp} are gentle functions of frequency, however, H can vary sharply with frequency. Observing the field at the end-fire directions where the gain of the Tx array is maximum and at the center frequency, the maximum value of the TF is given by

$$TF_{\max} = \frac{G_{\text{amp}}}{1 - HG_{\text{amp}}(D_1 + D_2)} \tag{5.2}$$

noting that $D_1 \simeq -D_2 \simeq \sqrt{2}/2$ and $e^{-j\frac{kd}{2}\sin\phi} \simeq -1$.

5.3 Miniaturized Dual-channel Radio Repeater Design

The repeater system bandwidth is determined by the impedance bandwidth of the antennas and the minimum isolation level between the Tx and Rx antennas. The minimum isolation, in turn, is determined from the bandwidth of the hybrid ring coupler and the symmetry with which the system is fabricated. It turns out that the hybrid ring coupler has higher bandwidth than the miniaturized Tx and Rx antennas. In an attempt to increase the system bandwidth, the bandwidth of the Tx and Rx antennas of the radio repeater should be improved. This must be done without increasing the physical dimensions of the antennas substantially while maintaining the

antenna height. For bandwidth enhancement, parasitic coupling technique is often utilized [69, 70, 71]. As reported in [56], the previous Rx antenna was designed to show high radiation efficiency with omni-directional vertical polarization in symmetric architecture. Since the Rx antenna consists of four quarter-wavelength traces, the electric current is maximized through the shorting pins. Therefore, by placing additional shorting pins near to the original shorting pins, a pair of the parasitic elements can be easily excited through the magnetic coupling as shown in Fig. 5.2(a). As mentioned before, the bandwidth improved Rx antenna should be designed in symmetric manner to allow for the near-field cancellation. The physical design parameters are optimized for operation around 2.42 GHz and are summarized in Table 5.1.

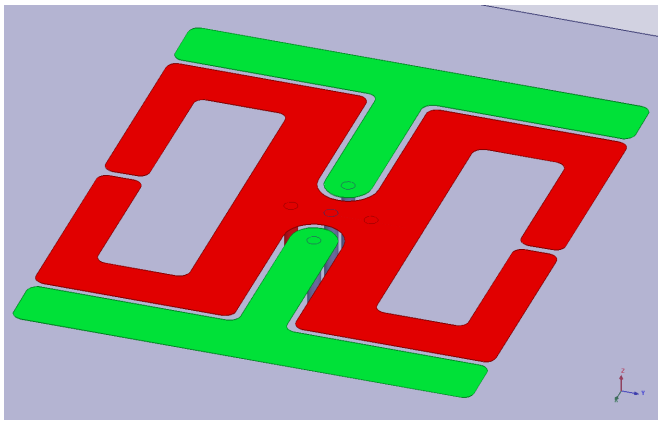

(a)

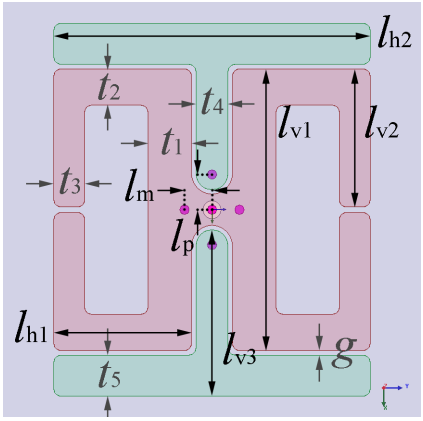

(b)

Figure 5.2: Wideband receive antenna: (a) geometry of the wideband Rx antenna; (b) design parameters.

Table 5.1: Design parameters of the wideband receive antenna

l_{h1}	l_{h2}	l_{v1}	l_{v2}	l_{v3}
7.62 mm	17.53 mm	15.64 mm	7.67 mm	9.25 mm

t_1	t_2	t_3	t_4	t_5
2.41 mm	2.01 mm	1.70 mm	1.78 mm	2.29 mm

l_p	l_m	g
1.96 mm	1.52 mm	0.25 mm

The radiation performance of the antenna can be characterized through the antenna gain and radiation efficiency as well as the input reflection coefficient. Therefore, the field profile should be investigated and analyzed to examine the antenna performance, especially with respect to the radiation bandwidth. As shown in Fig. 5.3, the bandwidth improved Rx antenna shows three operation regions. At the start of the band, one pair of the parasitic elements (see Fig. 5.3(a)) dominantly contributes to the far-field radiation. In the middle of the band, all four vertical pins are excited (see Fig. 5.3(b)) and radiate almost equally. At the end of the band, only the pair of the original pins radiates as shown in Fig. 5.3(c). In order to enhance the radiation gain, the electric currents which contribute to the far-field radiation should be maximized and be in-phased. Due to these in-phase currents, the modified Rx antenna shows an enhanced radiation gain and bandwidth as shown in Fig. 5.4. Considering the finite bandwidth of the input reflection coefficient, a -3 dB radiation bandwidth of almost 100 MHz is achieved while the physical dimensions of the antenna is confined within $\lambda_0/7 \times \lambda_0/6 \times \lambda_0/40$. In order to estimate the RCS of the proposed radio repeater in the backscattering direction, vertical polarization gain in H-plane is reported in Fig. 5.4(b). Due to the asymmetric ground effect, the maximum vertical polarization gain is tilted over the ground plane.

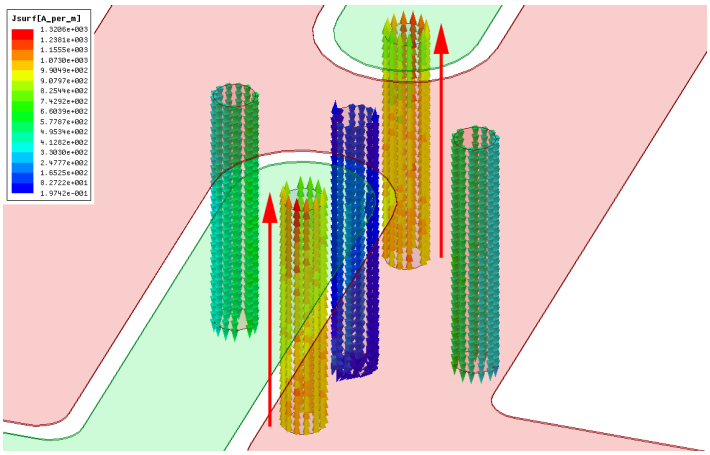

(a)

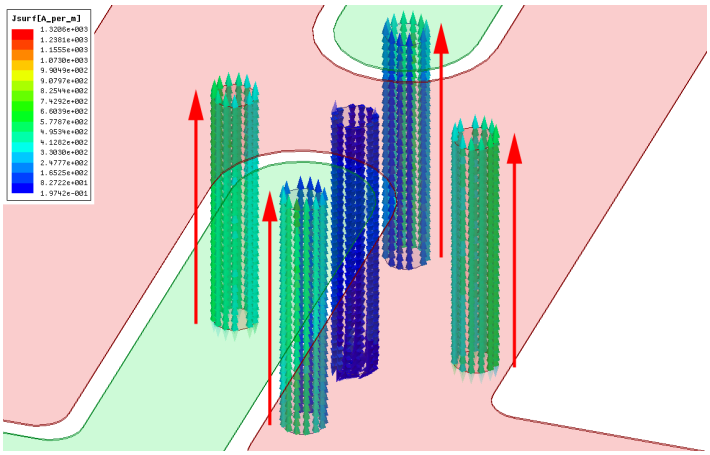

(b)

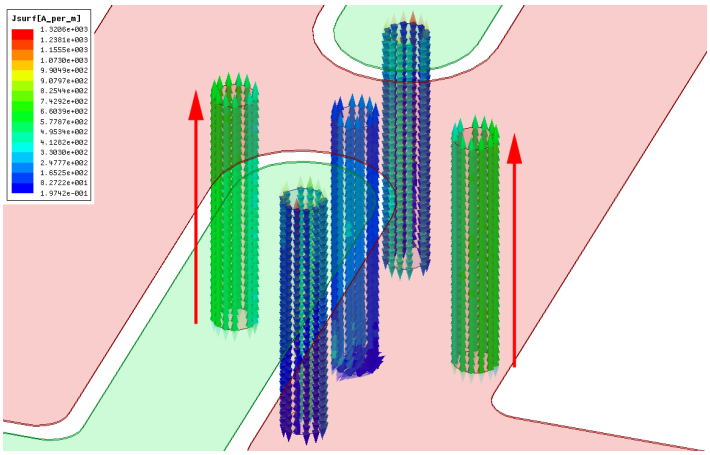

(c)

Figure 5.3: Current distribution on the vertical pins of the wideband Rx antenna: (a) at 2.38 GHz; (b) at 2.42 GHz; (c) at 2.48 GHz.

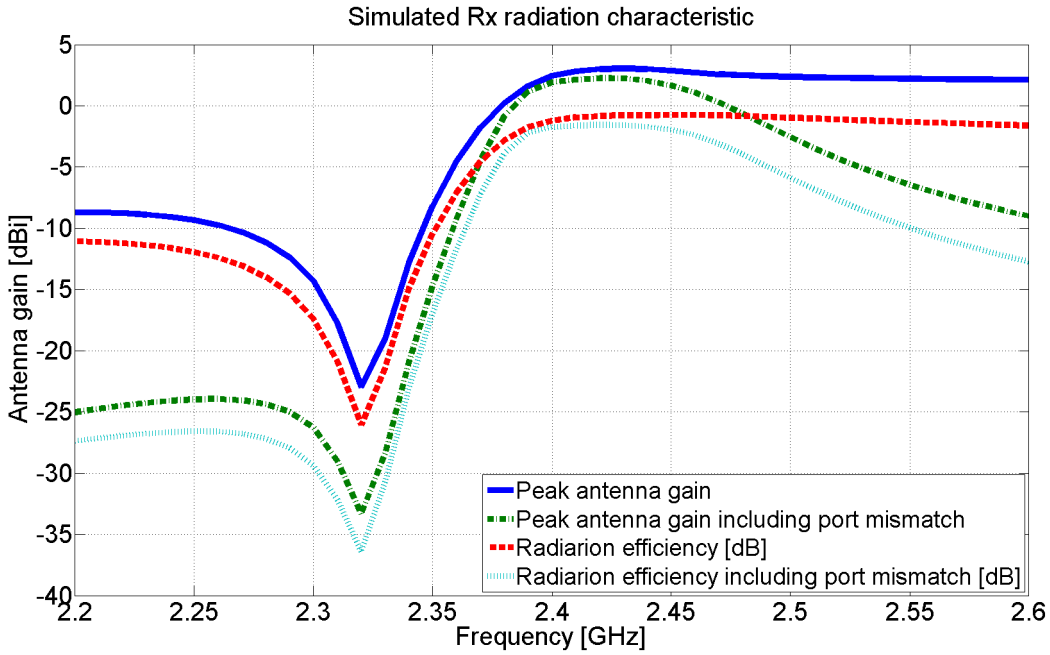

(a)

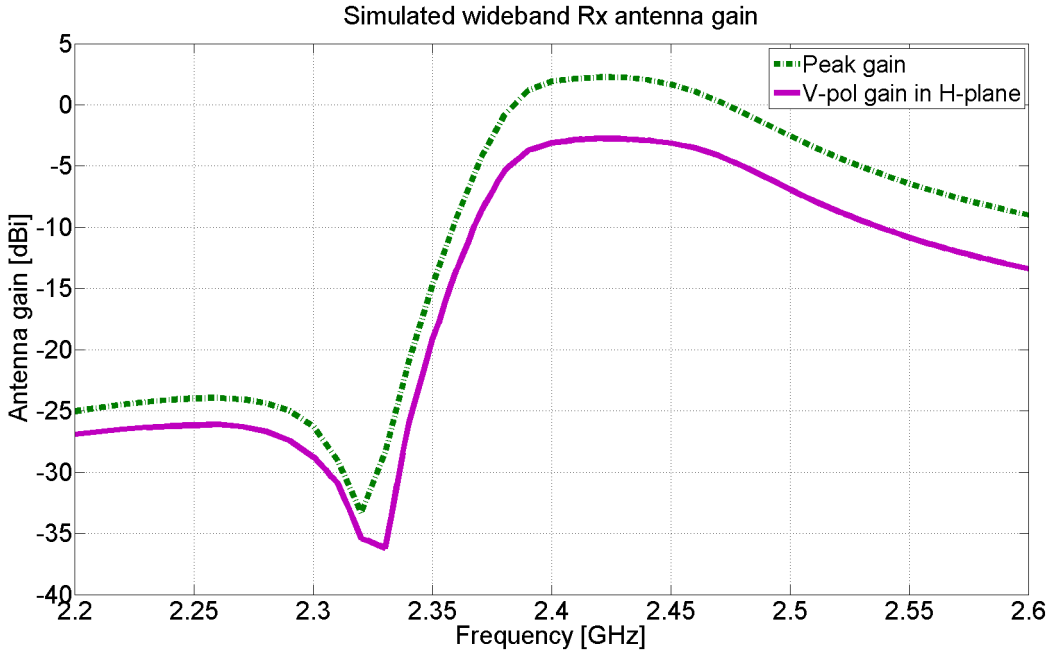

(b)

Figure 5.4: Radiation characteristic of the wideband Rx antenna: (a) peak antenna gain and radiation efficiency; (b) vertical polarization gain in H(xy)-plane.

By utilizing the similar approach as the wideband Rx antenna, the Tx antenna is redesigned, and its geometry is shown in Fig.5.5. However, only two arms are utilized so as to maintain the distance between the Tx and Rx antennas for keeping a low mutual coupling. This asymmetrical geometry of the modified Tx antenna induces out-of-phase current on the parasitic vertical pins, which decreases the radiation gain and bandwidth. In order to compensate the out-of-phase currents, one of the parasitic vertical pin is removed, while remaining the top parasitic element to adjust the level of the current distribution. Because of the smaller volume and surface area, the modified Tx antenna shows less radiation bandwidth compared to the modified Rx antenna as shown in Fig. 5.6. Nevertheless, the Tx antenna shows 60 MHz of -3 dB radiation gain bandwidth with $\lambda_0/6 \times \lambda_0/8 \times \lambda_0/40$ of physical dimensions. In addition, the Tx antenna shows the maximum vertical polarization gain in H-plane as shown in Fig. 5.6(b). The physical design parameters are optimized for operation around 2.43 GHz and summarized in Table 5.2.

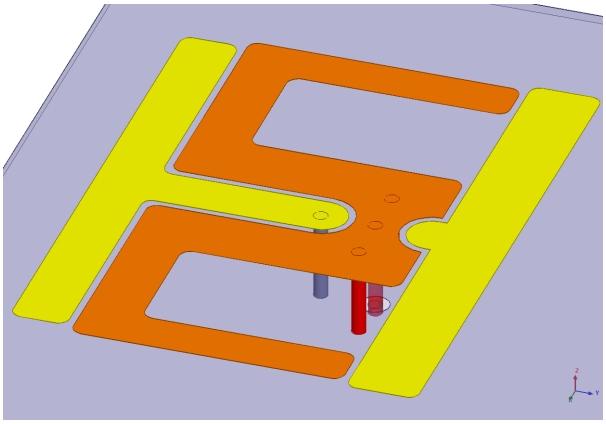

(a)

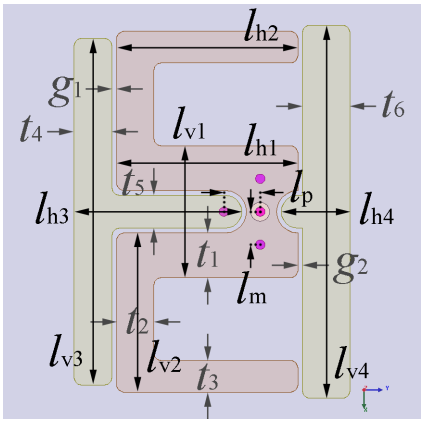

(b)

Figure 5.5: Wideband transmit antenna: (a) geometry of the wideband Tx antenna; (b) design parameters.

Table 5.2: Design parameters of the wideband transmit antenna

l_{h1}	l_{h2}	l_{h3}	l_{h4}	l_p
9.75 mm	9.75 mm	9.02 mm	3.68 mm	1.96 mm

l_{v1}	l_{v2}	l_{v3}	l_{v4}	l_m
7.11 mm	8.59 mm	18.69 mm	20.12 mm	1.78 mm

t_1	t_2	t_3	t_4	t_5
2.41 mm	2.01 mm	1.70 mm	2.03 mm	1.78 mm

t_6	g_1	g_2
2.54 mm	0.25 mm	0.25 mm

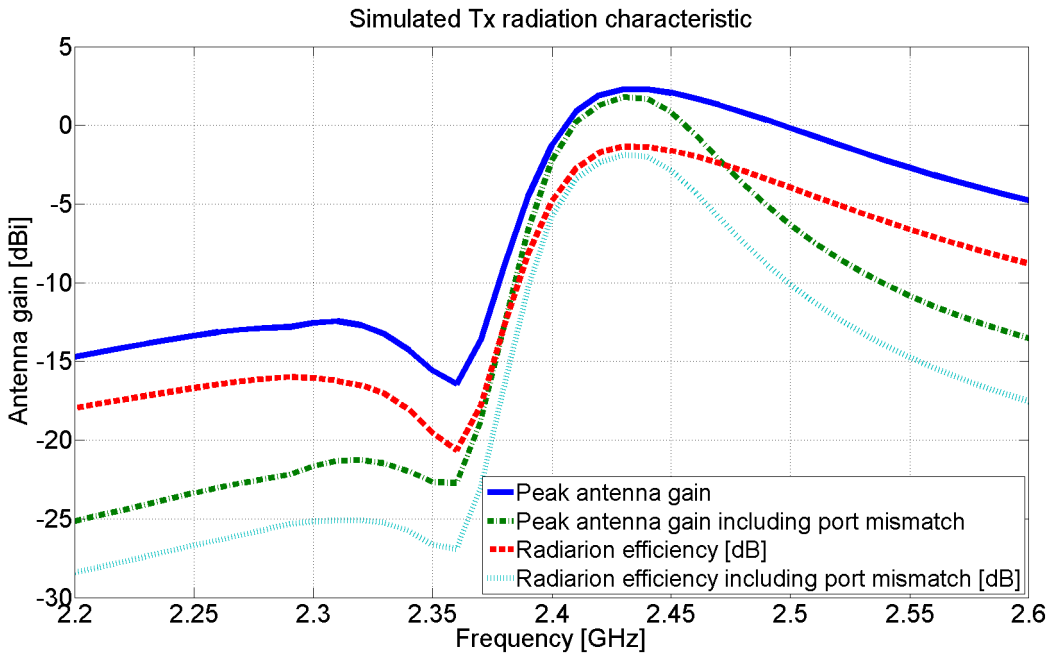

(a)

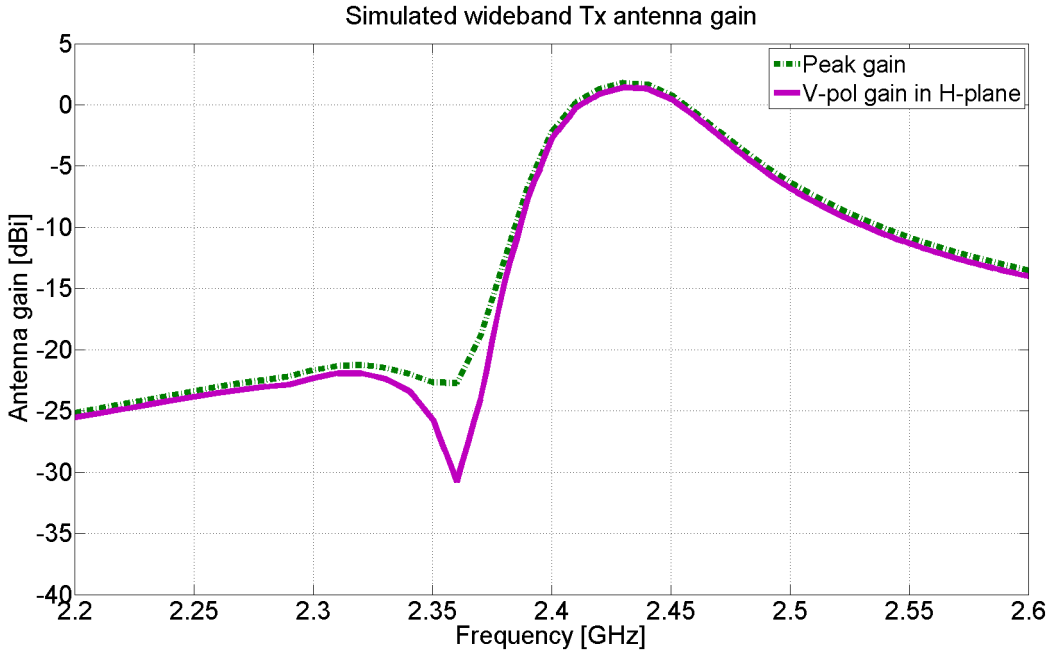

(b)

Figure 5.6: Radiation characteristic of the wideband Tx antenna: (a) peak antenna gain and radiation efficiency; (b) vertical polarization gain in H(xy)-plane.

5.4 Numerical and Experimental Results

Fig. 5.7 illustrates the geometry of the proposed radio repeater design and its simulated S-parameters. To maximize the Tx antenna array gain in the end-fire directions, the distance d between the two TX antennas is chosen to be around $\lambda_0/2$ (55.88 mm). The width W and length L of the substrate are designed so that the area is minimized without degrading the antenna gain in the H-plane. These values are set $W = \lambda_0/3.1 = 39.67\ mm$ and $L = \lambda_0/1.5 = 85.39\ mm$. For the numerical simulation of the combined antennas and the hybrid ring coupler, Port 1 and Port 2 are assigned to the input port of the Rx antenna and the input port of the modified hybrid ring coupler, respectively. Note that in the normal operation the Rx antenna port (Port 1) is attached to the input port of the hybrid ring coupler (Port 2). Based on a full-wave analysis using a commercial FEM solver (Ansoft's HFSS ver. 14.0), it is verified that the maximum mutual coupling is as low as -49 dB over the entire frequency band, while maintaining good input reflection coefficients on both the Rx and Tx antennas. As mentioned in Section 5.3, 100 MHz and 60 MHz bandwidth (-3 dB radiation gain bandwidth) can be achieved by the Rx and Tx antennas, respectively.

Since Port 1 and Port 2 are assigned to the Rx antenna and the input port of the modified hybrid ring coupler, the simulated transmission coefficient in Fig. 5.7(b) corresponds to $H(D_1 + D_2)$ in (5.1). In addition, the frequency response of the RF amplifier G_{amp} can be measured directly. Fig. 5.8 shows the phase of the simulated $H(D_1 + D_2)$ as a function of frequency. Noting that the phase of the RF amplifier is a linear function of frequency in the pass-band (around 2.4 GHz), it is now obvious that the phase of $HG_{\text{amp}}(D_1 + D_2)$ assumes zero value at two frequency points. At these two frequency points $|1 - HG_{\text{amp}}(D_1 + D_2)|$ is minimum, which results in the maximized values in the closed-loop transfer function as shown in Fig. 5.9.

The RCS of the radio repeater system utilizing the near-field cancellation technique can be given by [56]

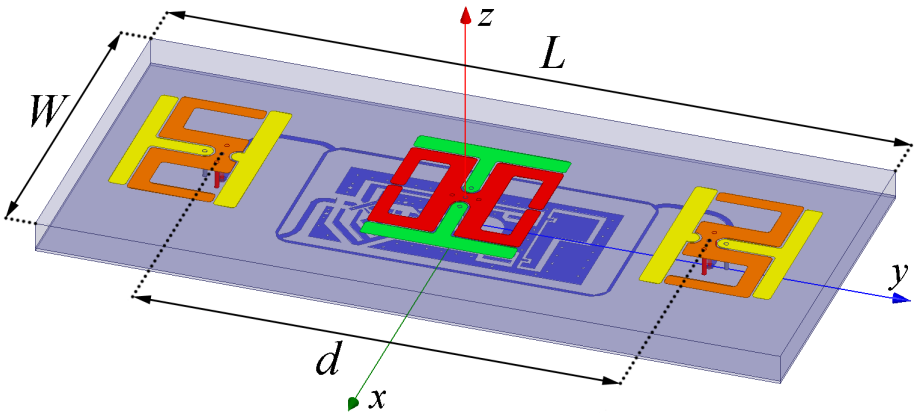

(a)

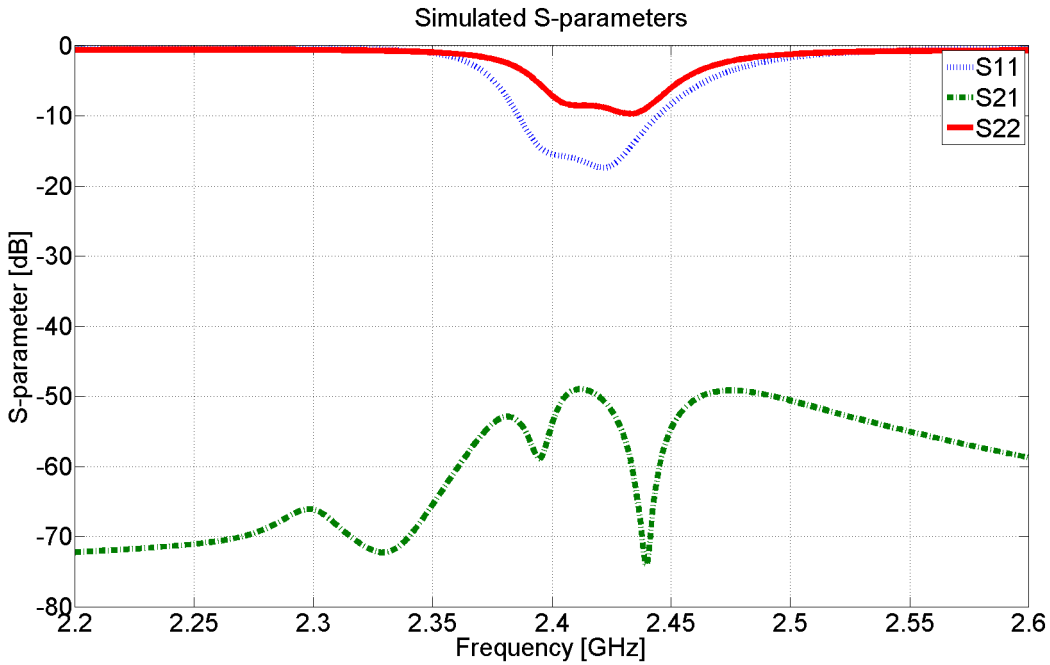

(b)

Figure 5.7: Dual-channel radio repeater: (a) geometry of the dual-channel radio repeater; (b) simulated S-parameters.

$$\sigma_{\text{repeater}} = \frac{\lambda_0^2}{4\pi} G_{\text{r}} T F G_{\text{t}} \tag{5.3}$$

where TF is the closed-loop transfer function and G_{r} and G_{t} are the gain of the Rx and Tx antennas, respectively. Hence, the RCS of the dual-channel radio repeater can be illustrated using the simulated antenna gains (Fig. 5.4(b) and Fig. 5.6(b)) and

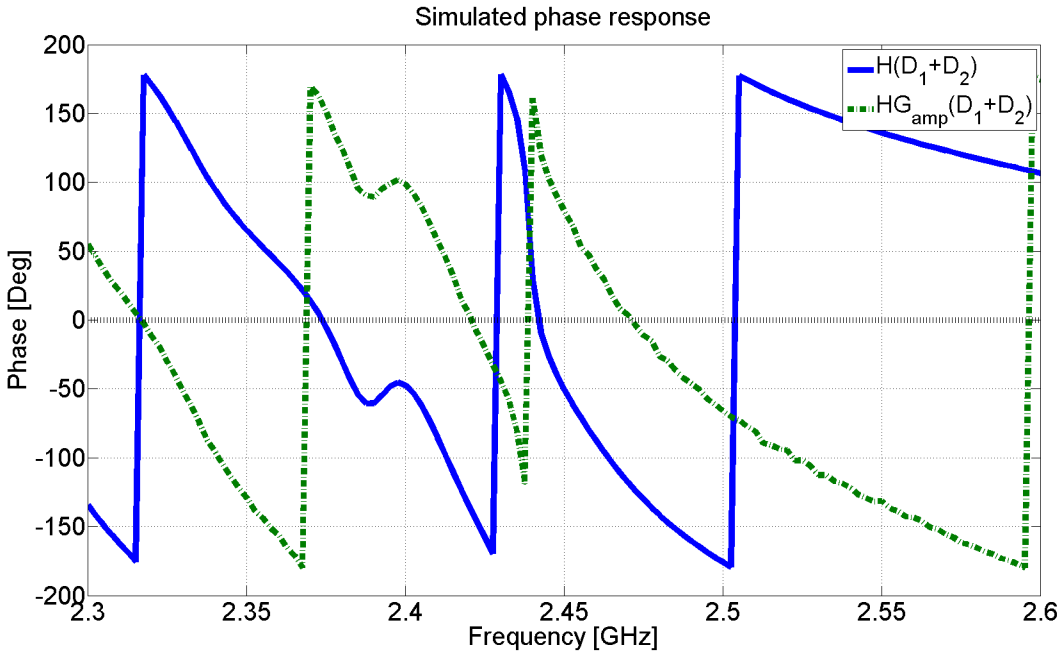

Figure 5.8: Simulated phase response of the mutual coupling including the hybrid ring coupler with and without 45 dB RF amplifier.

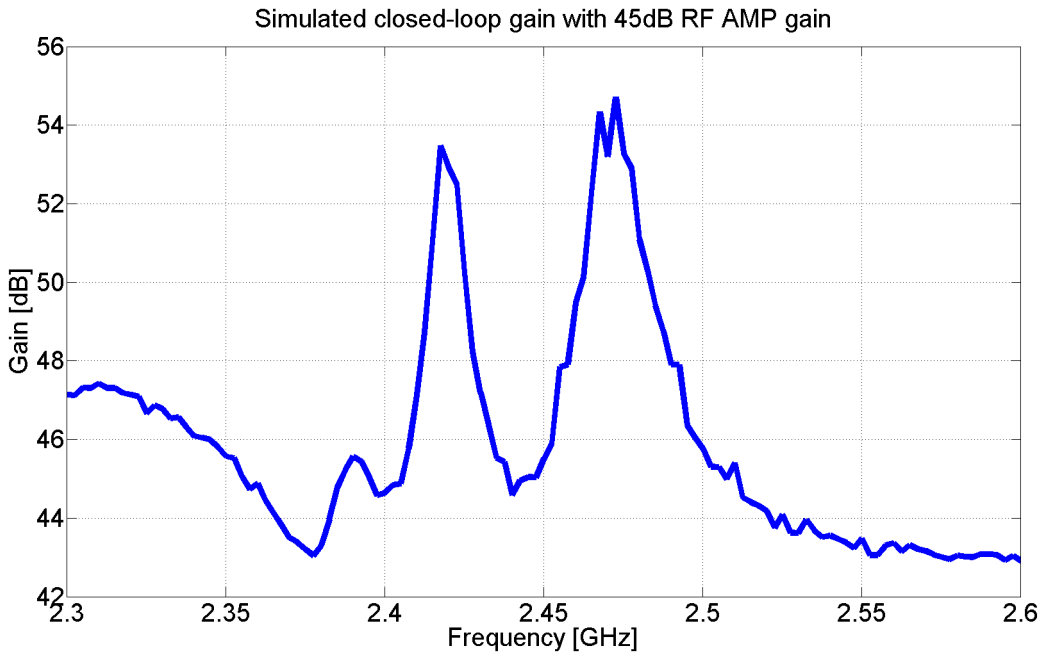

Figure 5.9: Calculated closed-loop transfer function of the miniaturized dual-channel radio repeater with 45 dB of RF amplifier gain.

the calculated system closed-loop function (Fig. 5.9). It should be mentioned that the RCS is calculated based on the simulated mutual coupling between the Tx and Rx antenna including the response of the modified hybrid ring coupler and the measured RF amplifier response. As mentioned, the phase characteristic with zero-crossing creates a closed-loop gain higher than the RF amplifier gain. Therefore, the effect of a commercial battery and a plastic housing might affect the phase characteristic, which results in the frequency shift of the location of the peak RCS values.

A prototype of the dual-channel radio repeater is fabricated using a 3.18-mm-thick Rogers RT/duriod 5880 substrate ($\varepsilon_r = 2.2$) and shown in Fig. 5.10. The fabricated radio repeater is characterized in the far-field using a monostatic radar system in backscatter mode with coherent background subtraction. As shown in Fig. 5.11, the RCS values of the dual-channel radio repeater is measured in H-plane and compared to a 0.36 m diameter metallic sphere. As mentioned, the proposed radio repeater shows two zero-crossing phase characteristic shown in Fig. 5.8. Therefore, if these zero-crossing frequencies are within the Tx and Rx antenna band, it is expected that two peak RCS values are achieved with higher than RF amplifier gain. As can be seen, the measured RCS shows two peak RCS values at 2.416 GHz and 2.444 GHz, which indicates the simultaneous operational capability of two channels. By comparing the RCS of the repeater with that of the metallic sphere, the dual-channel radio repeater shows RCS values of 27.7 dBsm and 26.0 dBsm at the repeater high-gain closed-loop bands. It should also be noted that the measured RCS between the two peaks shows the nominal RCS value of 13 dBsm corresponding to the RF amplifier gain of 45 dB. This means that when the phase characteristic of the open-loop gain crosses 180°, the RF amplifier gain (45 dB) dominates the closed-loop gain.

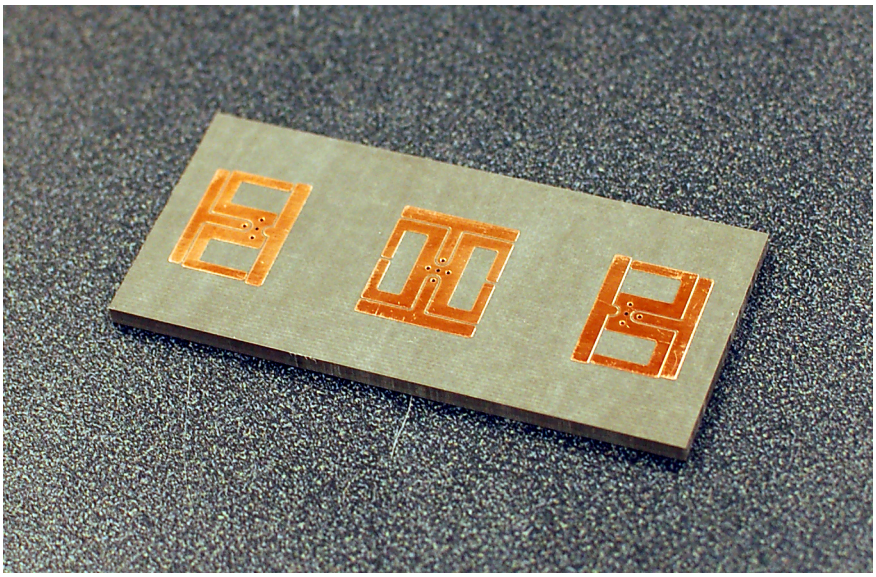

Figure 5.10: Prototype of the miniaturized dual-channel radio repeater.

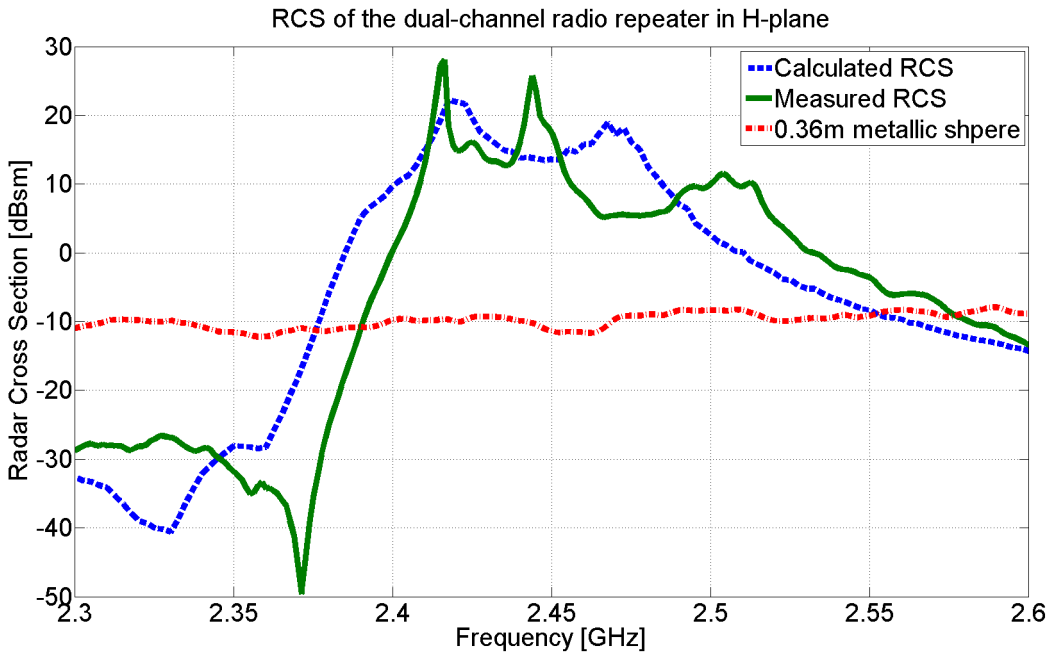

Figure 5.11: Measured radar cross section of the miniaturized dual-channel radio repeater showing two high-gain bands corresponding to high closed-loop gain.

5.5 Miniaturized Isolator-embedded Radio Repeater Design

In Section 5.2, the closed-loop system transfer function of the radio repeater design utilizing the near-field cancellation technique is analytically derived. Based on the calculated closed-loop transfer function and the simulated antenna radiation characteristics, the dual-band radio repeater is designed and experimentally verified. It is obvious that further decrease in the mutual coupling between the Tx and Rx antennas can result in higher gain and larger RCS value for the repeater.

In this section, a new isolator design is proposed and investigated in order to further suppress the mutual coupling to allow for the increase in the overall repeater system gain. The proposed meandered T-shape isolator consists of a meandered metallic trace and a vertical pin at the middle of the trace as shown in Fig. 5.12(a). As explained in Chapter II and III, the vertical shorting pins of the Tx and Rx antennas generate Transverse Magnetic (TM) waves in the substrate with zero cutoff frequency. These TM waves are parallel to the ground plane and perpendicular to the vertical pins. Therefore, the meandered T-shape isolator should be designed to be excited from the TM waves and suppress the mutual coupling. As the fundamental mode propagates from the Tx to Rx antennas, the horizontal H-field induces electric current on the vertical pin of the meandered T-shape isolator. As the T-shape isolator has two quarter-wavelength arms in the opposite direction a resonance occurs and further increases the current on the vertical pin. It turns out that the H-field generated by the T-shape isolator is in the opposite direction of the incident H-field, and as a result, the total H-field beyond the isolator is significantly reduced at the resonant frequency due to Lenz's law as shown in Fig. 5.12(b). In this way, the horizontal H-field at the location of the vertical pins of the Rx antenna can be decreased and the mutual coupling between the Tx and Rx antennas is suppressed. Fig. 5.13 shows the simulated mutual coupling utilizing the proposed meandered T-shape isolator. As can be seen, the mutual coupling is suppressed down to -17 dB, which corresponds to

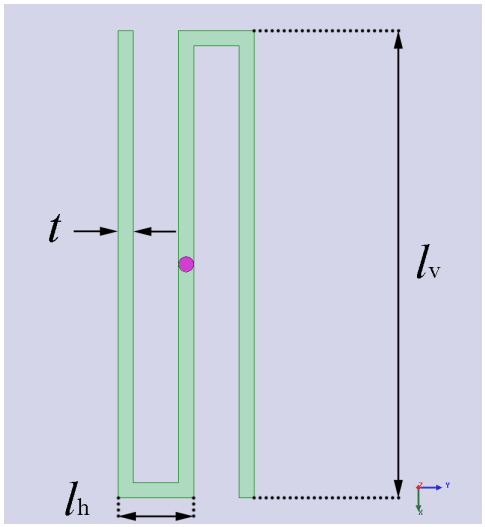

(a)

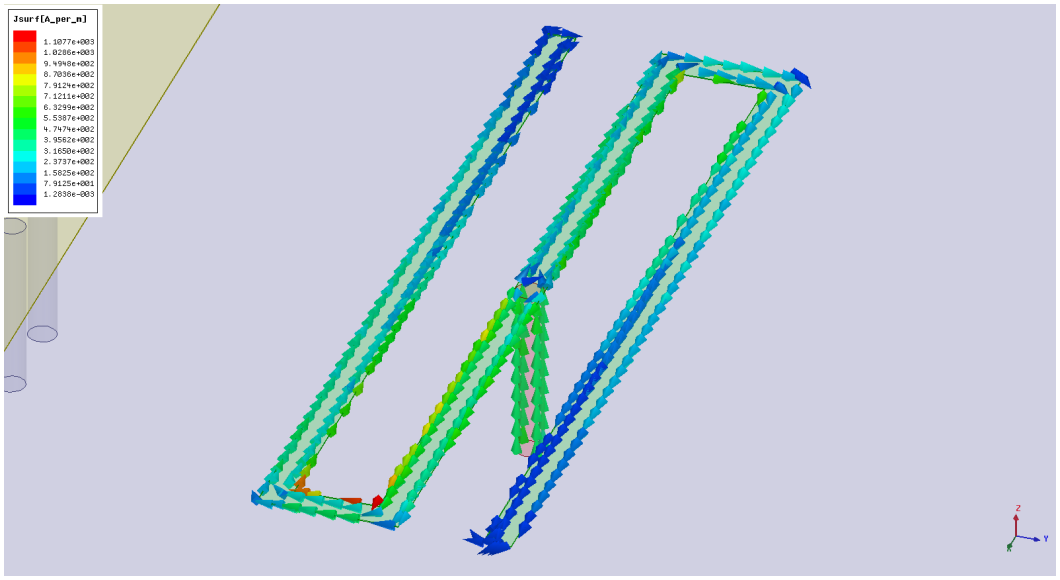

(b)

Figure 5.12: Meandered T-shape isolator: (a) geometry and design parameters of the meandered T-shape isolator; (b) simulated current distribution on the meandered T-shape isolator.

5 dB improvement. Also shown is that the Tx and Rx antenna responses are affected due to the interaction between the antennas and the meandered T-shape isolator. In fact, per our design the antennas are well matched (over -10 dB of input reflection coefficient), and the center frequency is at the desired value in the presence of the isolator. The physical design parameters of the T-shape isolator are optimized for

operation around 2.42 GHz and tabulated in Table 5.3.

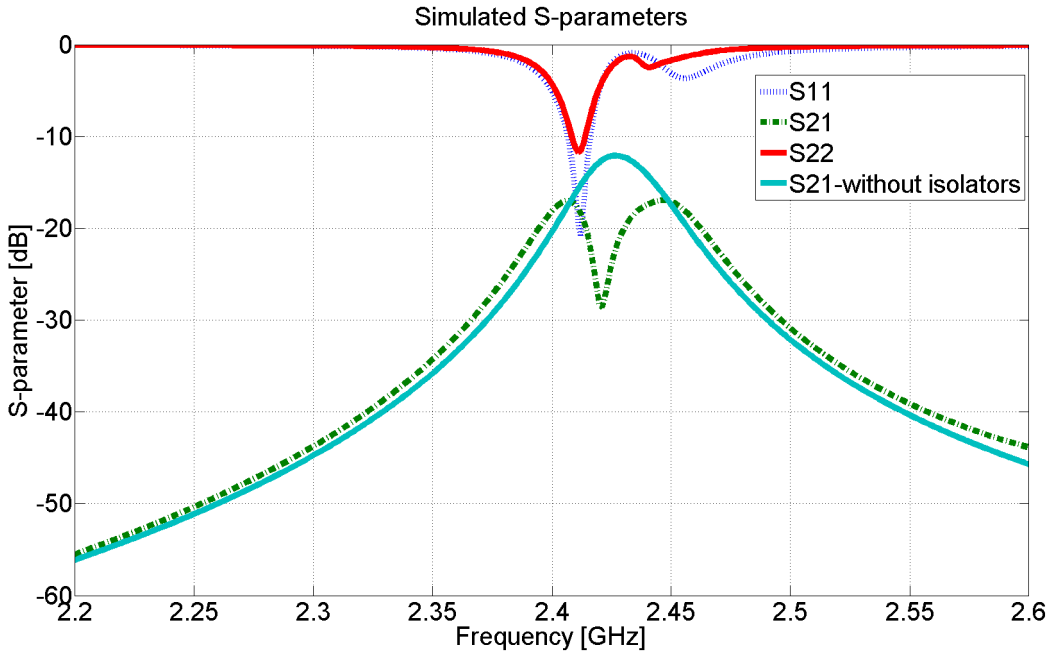

Figure 5.13: Simulated S-parameters with and without the meandered T-shape isolator.

The meandered T-shape isolator is embedded into the miniaturized radio repeater, which utilizes the near-field cancellation technique 5.14(a). As shown in Fig. 5.14(b), the mutual coupling between the Tx and Rx antennas is suppressed down to -80 dB at the operation frequency. Additionally, the peak level of the mutual coupling is decreased down to -55 dB, which corresponds to 1 dB improvement based on the previous design only using the near-field cancellation technique shown in Fig. 4.11 at Chapter IV. The physical design parameters are optimized and summarized in Table 5.3.

Table 5.3: Design parameters of the meandered T-shape isolator and miniaturized isolator-embedded radio repeater

l_v	l_h	t
15.75 mm	2.54 mm	0.51 mm

L	W	D_1	D_2
85.39 mm	39.67 mm	60.96 mm	41.40 mm

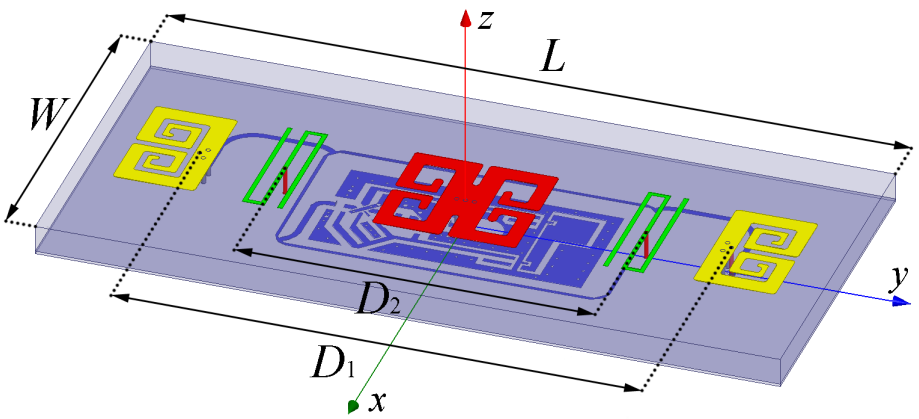

(a)

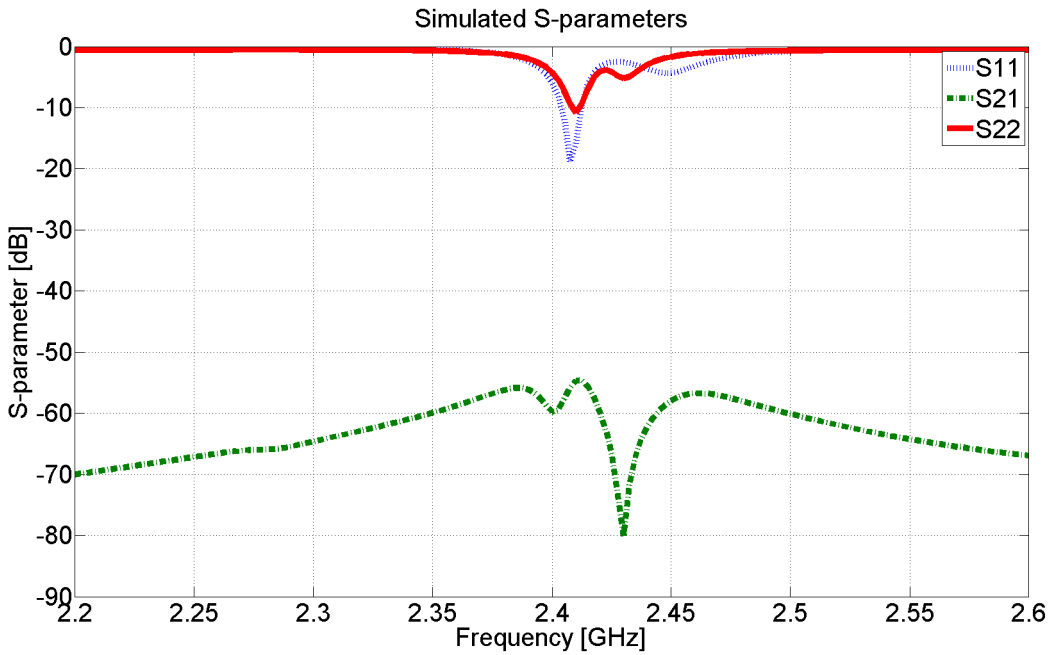

(b)

Figure 5.14: Miniaturized isolator-embedded radio repeater: (a) geometry and design parameters of the miniaturized isolator-embedded repeater; (b) simulated S-parameters.

As mentioned in Section 5.3, the antenna radiation characteristic of the radio repeater should be well characterized in order to estimate the overall repeater system gain as well as the closed-loop system transfer function. For this purpose, the isolator-embedded radio repeater shown in Fig. 5.14(a) is simulated and analyzed in Rx and Tx mode, separately. As shown in Fig. 5.15, the radiation efficiency of the Rx antenna decreases at the resonant frequency of the meandered T-shape isolator. Since the radiation efficiency is calculated as a ratio of the radiated power to the accepted power using a commercial FEM solver (Ansofts HFSS ver. 14.0), the drop of the radiation efficiency indicates that the power of the radiating E-field due to the vertical pins of the Rx antenna is decreased. In order to analyze this decrease of the radiating E-field, the current distributions on the vertical pins of the Tx and Rx antennas and the meandered T-shape isolator are investigated and shown in Fig. 5.16. As mentioned before, the electric current on the vertical pin of the meandered T-shape isolator is induced in the opposite direction of that of the Rx antenna. However, it is shown that the induced electric current on the vertical pin also radiates to the far-field and this, in turn, reduces the efficiency and lowers the gain of the Rx antenna.

Additionally, this phenomenon is also observed at the Tx antenna as shown in Fig. 5.17. However, the Tx antenna shows narrower and sharper drop of the radiation efficiency than the Rx antenna. As shown in Fig. 5.18, the meandered T-shape isolator is excited through the horizontal H-field and shows higher magnitude of the induced current due to the distance between the antenna and the isolator. As a result, the radiation efficiency drops further in the Tx mode than the Rx mode.

Here, it should be noted that the suppression of the mutual coupling needs to be performed in conjunction with the antenna performance. Since the RCS of the radio repeater relies on the combination of all of subcomponents, the investigation of the subcomponents is inevitable in the effort of design and estimation of the overall system performance.

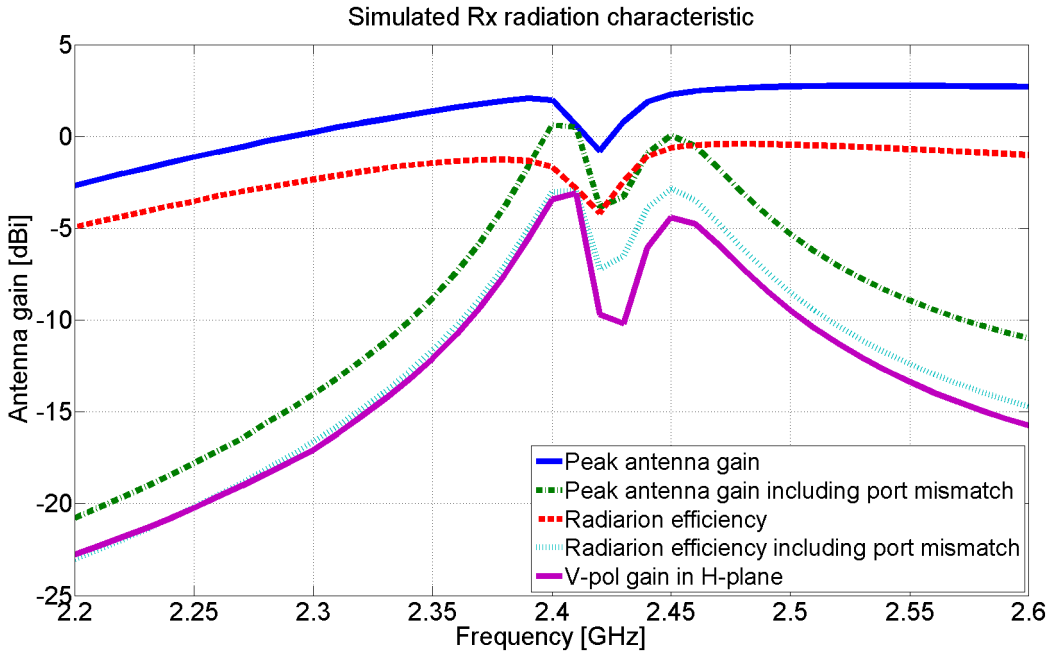

Figure 5.15: Radiation characteristic of the isolator-embedded repeater Rx antenna.

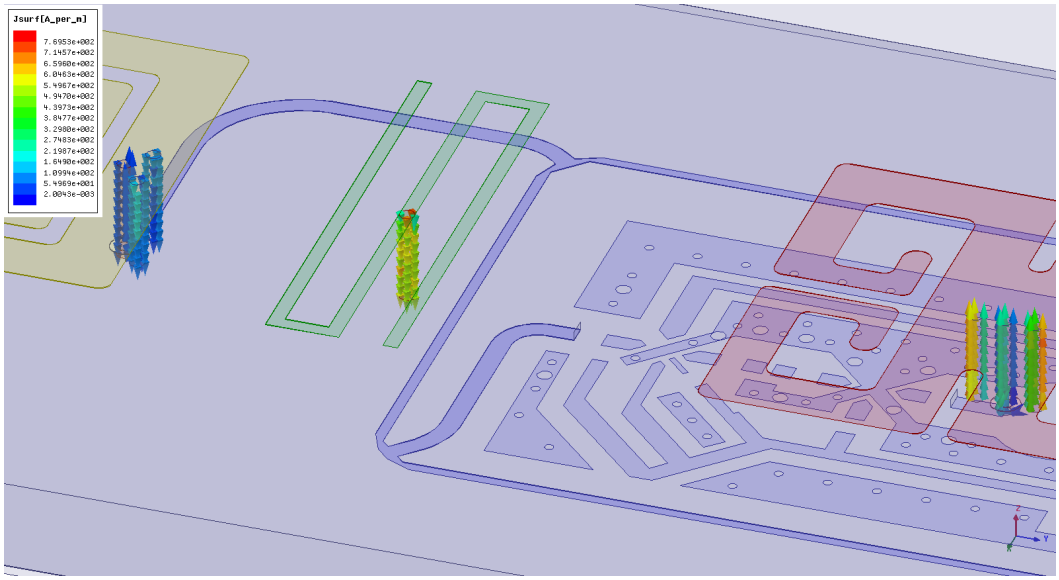

Figure 5.16: Current distribution on the vertical pins of the Tx and Rx antennas and the meandered T-shape isolator at 2.42 GHz (Rx mode).

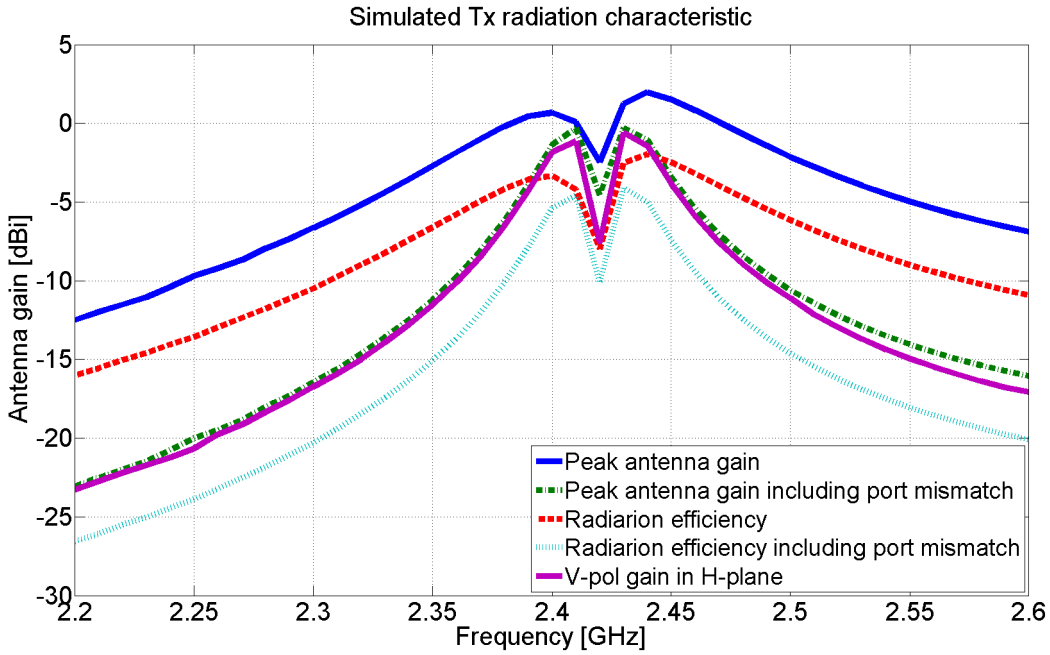

Figure 5.17: Radiation characteristic of the isolator-embedded repeater Tx antenna.

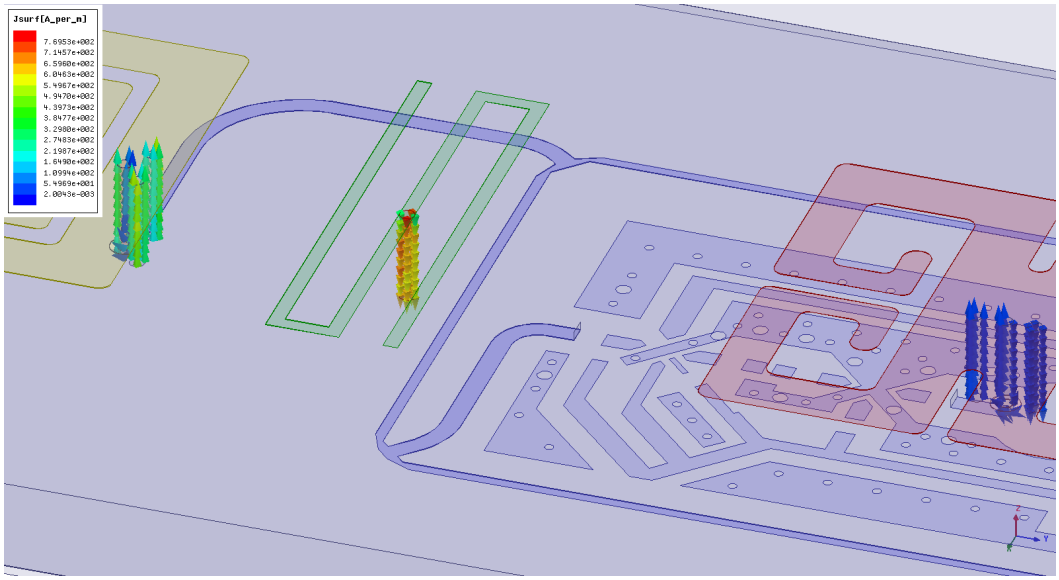

Figure 5.18: Current distribution on the vertical pins of the Tx and Rx antennas and the meandered T-shape isolator at 2.42 GHz (Tx mode).

By using the simulated transmission coefficient in Fig. 5.14(b) and the measured response of the RF amplifier, the closed-loop transfer function is numerically calculated using (5.2) and shown in Fig. 5.19. In this system integration, a 52 dB gain of the RF amplifier is considered due to the system stability margin and physical implementation. As before, the value and location of the peak gain of the closed-loop transfer function depends on the transmission coefficient and the RF amplifier characteristic.

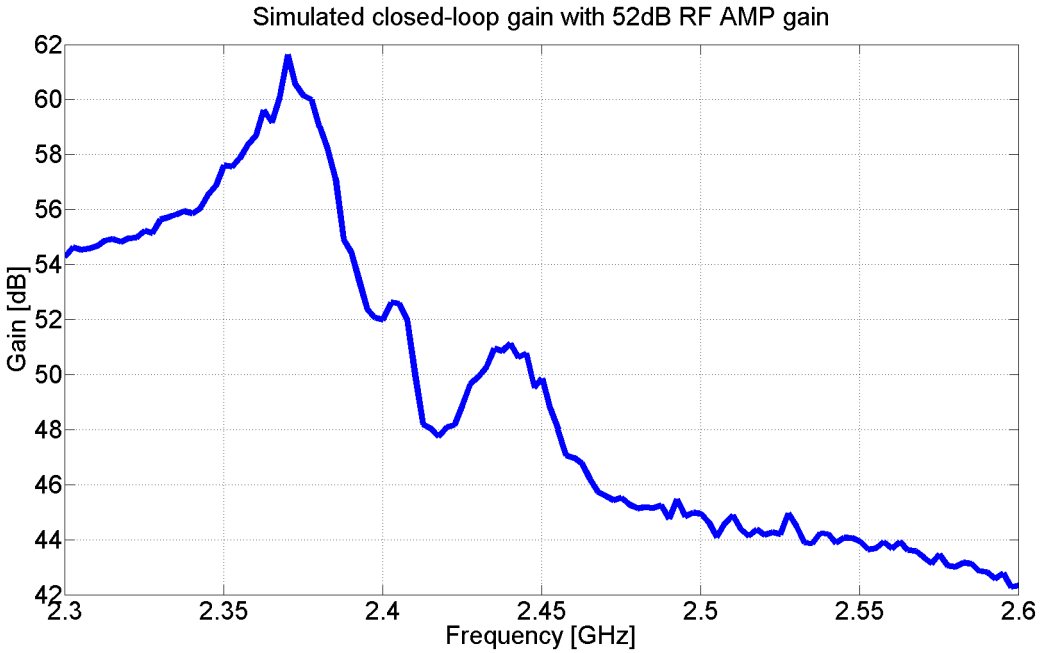

Figure 5.19: Calculated closed-loop transfer function of the miniaturized isolator-embedded radio repeater with 52 dB of RF amplifier gain.

In addition to the closed-loop transfer function, the simulated antenna gains (Fig. 5.15 and Fig. 5.17) are used to estimate the RCS of the miniaturized isolator-embedded radio repeater. As shown in Fig. 5.20, the estimated RCS of the miniaturized isolator-embedded radio repeater shows a lower peak RCS value than the previous radio repeater design using the near-field cancellation technique and the dual-channel radio repeater design. It turns out that although the improvement on the mutual coupling and the high gain of the RF amplifier are achieved, the antenna

gain drop also affects the overall RCS, which results in the lower RCS value. However, it should be mentioned that the miniaturized isolator-embedded radio repeater shows almost flat frequency response and wide bandwidth than previous two repeater designs except for the RCS drop at the resonant frequency of the meandered T-shape isolator. This indicates that by separately utilizing two types of isolation techniques it is feasible to achieve the suppression of the mutual coupling and increase the RCS.

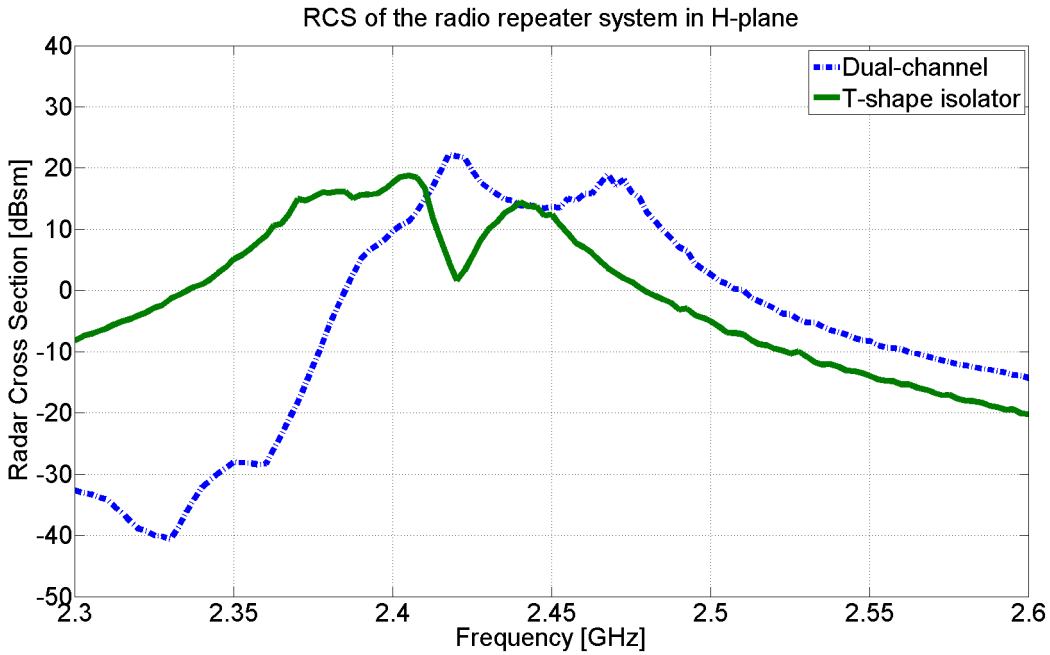

Figure 5.20: Simulated RCS of the miniaturized isolator-embedded radio repeater.

5.6 Conclusions

In this chapter, the system performance and RCS of miniaturized radio repeaters are investigated and analyzed. Due to the intrinsic positive feedback loop between the Tx and Rx antennas, radio repeaters form a closed-loop system. As a result, the overall closed-loop transfer function should be considered rather than a sum of the RF amplifier gain and the antenna gains. This closed-loop transfer function determines the overall system gain and the RCS value. The proposed closed-loop transfer func-

tion is investigated and utilized to enhance the performance of the radio repeater. By utilizing the magnetic and electric couplings, the Tx and Rx antennas are designed to show the improved radiation efficiency and bandwidth with vertical polarization. Incorporated with parasitic elements, the Tx and Rx antennas show multiple resonant frequencies, where the dominant radiation separately comes from the original antenna and the parasitic elements. Therefore, wideband input reflection coefficient and radiation efficiency can be achieved. Based on the calculated closed-loop transfer function and the simulated antenna responses, the RCS of the dual-channel radio repeater is analyzed and compared with a 0.36 m diameter of metallic sphere. It is shown that the proposed radio repeater provides dual-channel capability with more than 27.7 dBsm and 26.0 dBsm of RCS on each of channels. Additionally, the combination of two isolation technique is investigated and demonstrated. In order to reduce the computational cost and fabrication complexity, a quarter-wavelength meandered T-shape isolator is proposed. By incorporating with the near-field cancellation technique, the proposed T-shape isolator decreases the peak level of the mutual coupling by -55 dB over the entire frequency band. Even though the proposed radio repeater utilizing the T-shape isolator and near-field cancellation shows an RCS drop due to the antenna gain drop, it shows the feasibility of the isolation improvement and the integration of two isolation techniques. Therefore, it is expected that by separating the operating frequency of each of isolators wider bandwidth of RCS can be achieved.

CHAPTER VI

Conclusions

6.1 Summary of Achievements

The motivation of this thesis has been to enhance wireless signal connectivity in complex environments, while maintaining low-power communication. In complex environments wireless communication relies on multi-path propagation, which results in the loss of connectivity due to high path-loss and fast fading. By reestablishing line-of-sight propagation, the adverse effects of various complex environments can be mitigated and addressed. This approach can be accomplished by a set of RF devices – so-called signal booster, multi-hop communication, or radio repeater – which amplify the received signal and retransmit it to other communication nodes. In this scheme, mutual coupling between adjacent antennas is the main restriction to system performance and miniaturization. The accomplishment of significant suppression of the mutual coupling can contribute to not only miniaturization of radio repeaters, but also compact integration of wireless systems.

To this end, this thesis places particular emphasis on improving the suppression of the mutual coupling between adjacent antennas. Existing isolation techniques involve large physical dimensions and show poor isolation performance, and hence are not suitable for miniaturized subwavelength wireless systems. Therefore, studies to elucidate physical understanding of the mutual coupling have been conducted,

and new concepts of suppression of the mutual coupling have been proposed and demonstrated in this thesis. As shown in Fig. 6.1, the proposed isolation techniques have achieved great reduction of the mutual coupling between two adjacent antennas within a subwavelength distance. Finally, the repeater system gain and radar cross section (RCS) have been investigated to evaluate the performance of the radio repeater system.

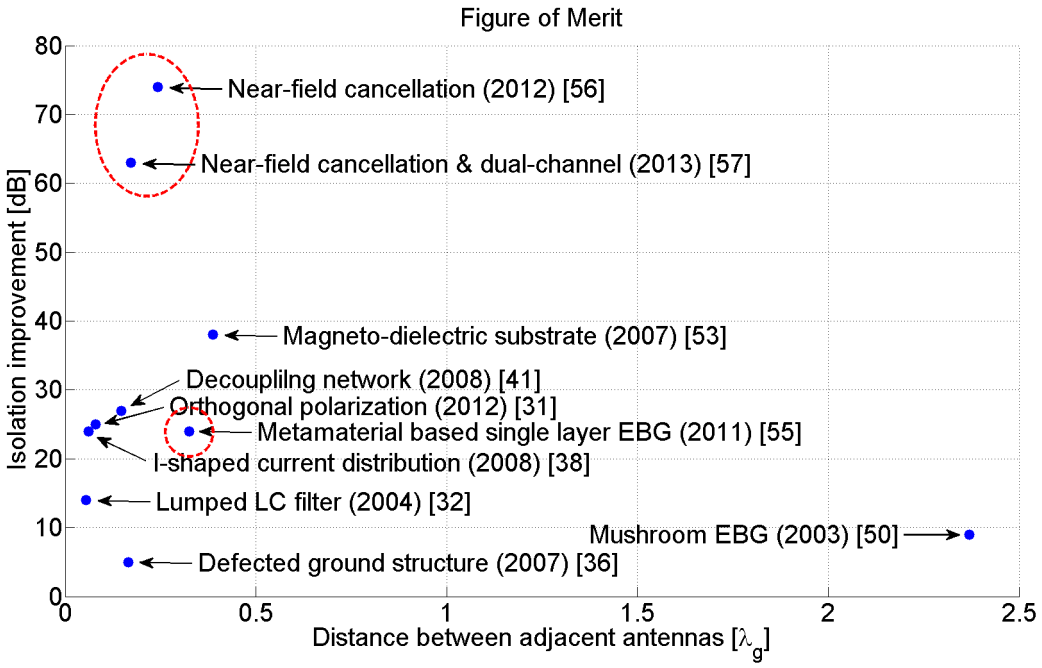

Figure 6.1: Summarized figure of merit for the proposed isolation techniques.

6.1.1 Equivalent transmission line model for a thin dielectric-coated substrate and mutual coupling

In most practical communication system sub-components such as antennas, RF amplifiers, and filters tend to be integrated into a single dielectric-coated conductor for compact system configuration. As these components share a single ground, mutual coupling is inevitable, and it restricts the performance of the system. In order to understand the mechanism of the mutual coupling, surface waves and substrate

modes are explicitly analyzed because the cutoff frequency of each of these mechanisms is zero. The dominant substrate mode can be approximated by a quasi-TEM wave within and at the vicinity of the thin substrate. As a result, the propagation of the TEM wave which causes the mutual coupling is explained by an equivalent transmission line model.

6.1.2 Metamaterial-based Electromagnetic Band-Gap isolator

The term metamaterial generally refers to a material which exhibits a negative permittivity and/or a negative permeability in some frequency range of interest. By possessing a positive permittivity and a negative permeability, it is well known that this effective medium inhibits wave propagation. As a solution to the mutual coupling problem caused by the substrate mode, this property is adopted and utilized. Based on the equivalent transmission line model, a metamaterial-based electromagnetic band-gap (EBG) isolator is designed to be induced by the horizontal H-field and show a magnetic resonance. In this way, a negative permeability can be achieved, which in turn generates a perfect magnetic conductor and shows a band-gap (stop band) characteristic. This metamaterial-based EBG channel isolator is integrated into the subwavelength radio repeater system and shows 24 dB of isolation improvement.

6.1.3 Near-field cancellation technique

Although the metamaterial-based EBG channel isolator suppresses the mutual coupling between two adjacent antennas, the design process of the radio repeater incorporating the EBG channel isolator requires large computational resources. In order to achieve better isolation and also decrease the design complexity, a novel isolation technique is proposed and implemented. As mentioned, the mutual coupling between the transmit (Tx) and receive (Rx) antennas mainly comes from the substrate mode within the thin substrate. We use the idea that by adding two signals 180° out-

of-phase with each other the sum will be cancelled. This can be employed to suppress the mutual coupling by utilizing a two element antenna array as the Tx antenna. A conventional hybrid ring coupler is adopted and modified in order to feed the Tx antenna array with the same magnitude but out-of-phase signals. The radio repeater design utilizing this near-field cancellation technique shows 21.3 dBsm of RCS value with 50 dB of RF amplifier gain.

6.1.4 System gain and Radar Cross Section

The radio repeater can be characterized in backscattering mode due to its transponder response. As a result, the radio repeater is evaluated and validated through RCS measurements. In order to estimate the RCS value, the radio repeater system is investigated and analyzed. As the mutual coupling between the Tx and Rx antennas of the radio repeater forms a positive feedback system, a closed-loop transfer function is derived to estimate the repeater system gain. By using this closed-loop transfer function, Tx and Rx antenna gains, and RF amplifier gain, the RCS of the radio repeater is numerically estimated. Additionally, a pair of parasitic elements is proposed and designed to enhance the radiation bandwidth of the repeater antenna. As a result, it is shown that the radio repeater utilizing wideband antennas and the near-field cancellation technique shows simultaneous dual-channel capability. The dual-channel radio repeater is measured and shows 27.7 dBsm and 26.0 dBsm of RCS values on each of the channels.

6.2 Future work

While the main contribution of this thesis is on the suppression of the mutual coupling and the improvement of the repeater RCS, the future directions of the technologies inspired and enabled by this thesis are extensive. The main focus of the future work entails an increase of the RCS and improved low-power communication.

6.2.1 High-gain Wideband Radio Repeater Architecture

In Chapter III, the metamaterial-based EBG channel isolator proves to suppress the substrate mode within a thin dielectric-coated substrate. By utilizing the magnetic resonance, a perfect magnetic conductor wall can be generated which inhibits the propagation of the dominant substrate mode. In addition to the resonant-based EBG channel isolator, the near-field cancellation technique also has been proposed in Chapter IV, which achieves suppression of the mutual coupling by the summation of two signals with the same magnitude but out-of-phase. Then, it is obvious that a combination of the EBG channel isolator and the near-field cancellation technique improves the suppression of the mutual coupling. This attempt definitely promises to decrease the mutual coupling as the operation principles of these techniques are independent of each other. However, it should be noted that the closed-loop transfer function needs to be maximized in order to improve the RCS of the radio repeater. Therefore, instead of decreasing the mutual coupling at the single operation frequency, it is recommended that two separated isolation frequencies are more helpful to increase the RCS value over a wide frequency range. This can be achieved by separating the resonant frequency of the EBG channel isolator and the center frequency of the near-field cancellation technique (i.e. the operation frequency of the hybrid ring coupler).

6.2.2 Adaptive Beam controlled Radio Repeater Architecture

As discussed in Chapter IV, the radio repeater architecture using the near-field cancellation technique creates an electric null-plane at the plane of symmetry. As a result, the proposed radio repeater shows the maximum RCS in the end-fire directions, which indicates that an array of radio repeaters (repeater cluster) can modify the beam pattern and radiation gain. Furthermore, a phase shifter can be integrated into the radio repeater system. In this approach, beamforming capability with two

or more repeaters enables enhanced repeater performance and an adaptive operation such as security sensing network and tracking the end-node.

6.2.3 Smart Radio Repeater Architecture

The active components required for amplification of the RF signal suffer from the drawback of high-power consumption. The proposed radio repeaters in this thesis employ simple analogy RF circuitry in order to decrease the system complexity and cost. In this scheme the active components continuously operate which reduces the life of the power source. In order to mitigate this power consumption and improve the performance of the radio repeater, the use of a wake-up circuit can be explored. By utilizing this wake-up circuit, three major performance improvements can be recommended: 1) hibernation mode with extremely low-power consumption, 2) channel selective operation capability, 3) isolation improvement by gating the DC bias networks. As the wake-up circuit is triggered by the interrogating signal, the power consumption of the active components is saved. Additionally, modern digital communication is carried out through communication protocols including signal authentication and synchronization. With current technology, a wake-up circuit which can selectively operate to the specific channel by detecting a pilot signal is achievable. Finally, a wake-up circuit can be explored as a gate timing generator, which disconnects the feedback loop by turning off one of the cascaded RF amplifier stages. As a result, the mutual coupling can be greatly decreased at the cost of a small latency.

6.3 List of Publications

The contributions of this thesis have been published in the following peer-reviewed journal articles and conference proceedings.

Referred Journal Articles

Y.J. Song and K. Sarabandi, "System Gain and Performance Enhancement of Miniaturized Radio Repeaters for Ad-hoc Wireless Communication," in preparation.

Y.J. Song and K. Sarabandi, "Equivalent Circuit Model for Metamaterial Based Electromagnetic Band-Gap Isolator," *IEEE Antennas Wireless Propag. Lett.*, vol. 11, pp. 1366-1369, 2012

Y.J. Song and K. Sarabandi, "Miniaturized Radio Repeater for Enhanced Wireless Connectivity of Ad-hoc Networks," *IEEE Trans. Antennas Propag.*, vol. 60, no. 8, pp. 3913-3920, Aug. 2012

K. Sarabandi and Y.J. Song, "Subwavelength Radio Repeater System Utilizing Miniaturized Antennas and Metamaterial Channel Isolator," *IEEE Trans. Antennas Propag.*, vol. 59, no. 7, pp. 2683-2690, Jul. 2011

Conference Proceedings

Y.J. Song and K. Sarabandi, "Gain and Bandwidth Enhancement of Micro-Radio-Repeaters for Ad-hoc Wireless Communication," accepted to *IEEE Int. Symp. Antennas Propag. USNC/URSI Nat. Radio Science Meeting*, Orlando, FL, 2013

Y.J. Song and K. Sarabandi, "Design of Radio Repeater System Using a Near-field Cancellation Technique," *IEEE Int. Symp. Antennas Propag. USNC/URSI Nat. Radio Science Meeting*, Chicago, IL, Jul. 2012

Y.J. Song and K. Sarabandi, "Studies on Mutual Coupling and Invariant Functionality of Small Radio Repeater System," *IEEE Int. Symp. Antennas Propag. USNC/URSI Nat. Radio Science Meeting*, Spokane, WA, Jul. 2011

K. Sarabandi, Y.J. Song, and J. Oh, "Enhanced Ad Hoc Wireless Connectivity in Complex Environment Using Small Radio Repeater Systems," *Proc. SPIE*, vol. 8031, 803117, Orlando, FL, May 2011

Y.J. Song and K. Sarabandi, "Small Radio Repeater System for Enhancement of Wireless Connectivity," *IEEE Int. Symp. Antennas Propag. USNC/URSI Nat.*

Radio Science Meeting, Toronto, ON, Canada, Jul. 2010

Y.J. Song and K. Sarabandi, "Suppression of the Mutual Coupling Between Two Adjacent Miniaturized Antennas Using Printed Resonant Circuits," *IEEE Int. Symp. Antennas Propag. USNC/URSI Nat. Radio Science Meeting*, Charleston, SC, Jun. 2009

APPENDICES

APPENDIX A

RSSI measurement at a wooden building model

A prototype of the proposed miniaturized radio repeater using near-field cancellation technique is experimentally validated and evaluated in the actual complex channel environments. In order to verify the performance of the radio repeater, radio signal strength indicator (RSSI) is measured using a pair of commercial XBee antenna modules [72]. The complex channel is characterized by measuring RSSI with a fixed location of the Tx module and without repeaters, as illustrated in Fig. A.1. As can be seen, deep shadow regions are observed behind the metal post and upper side of the building. By placing a repeater at the edge of the building, it is observed that almost 10 dB of signal enhancement is achieved behind the metal post as shown in Fig. A.2. Furthermore, a chain of multiple radio repeaters is suggested to improve the signal coverage. As shown in Fig. A.3, by utilizing two radio repeaters the shadow region from the metal post is entirely covered, and the north side is also improved.

In this measurement[1], the transmit power was set to -10 dBm, and the gain of repeaters' RF amplifier was set to 50 dB which corresponds to 21.3 dBsm of RCS.

[1]This measurement was collaborated with Dr. Jonathan Fink.

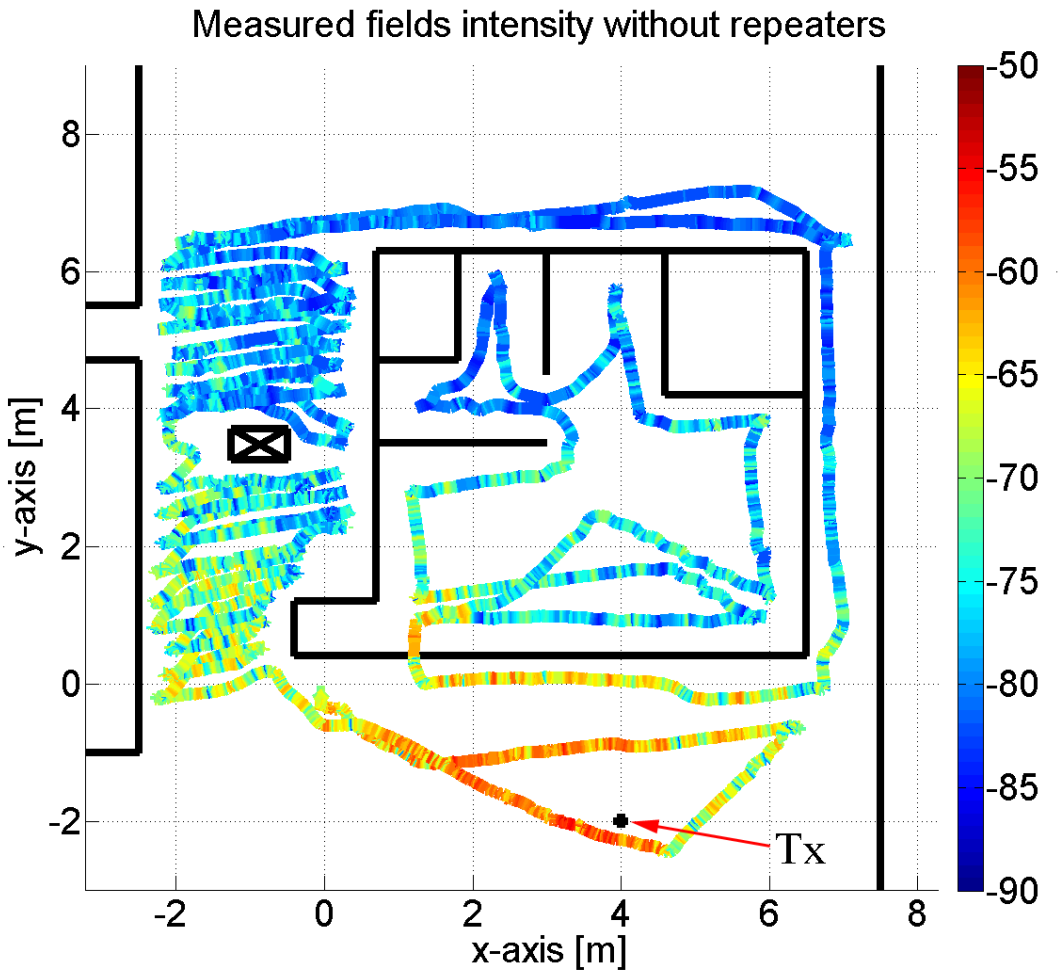

Figure A.1: Measured RSSI of a wooden building without repeater.

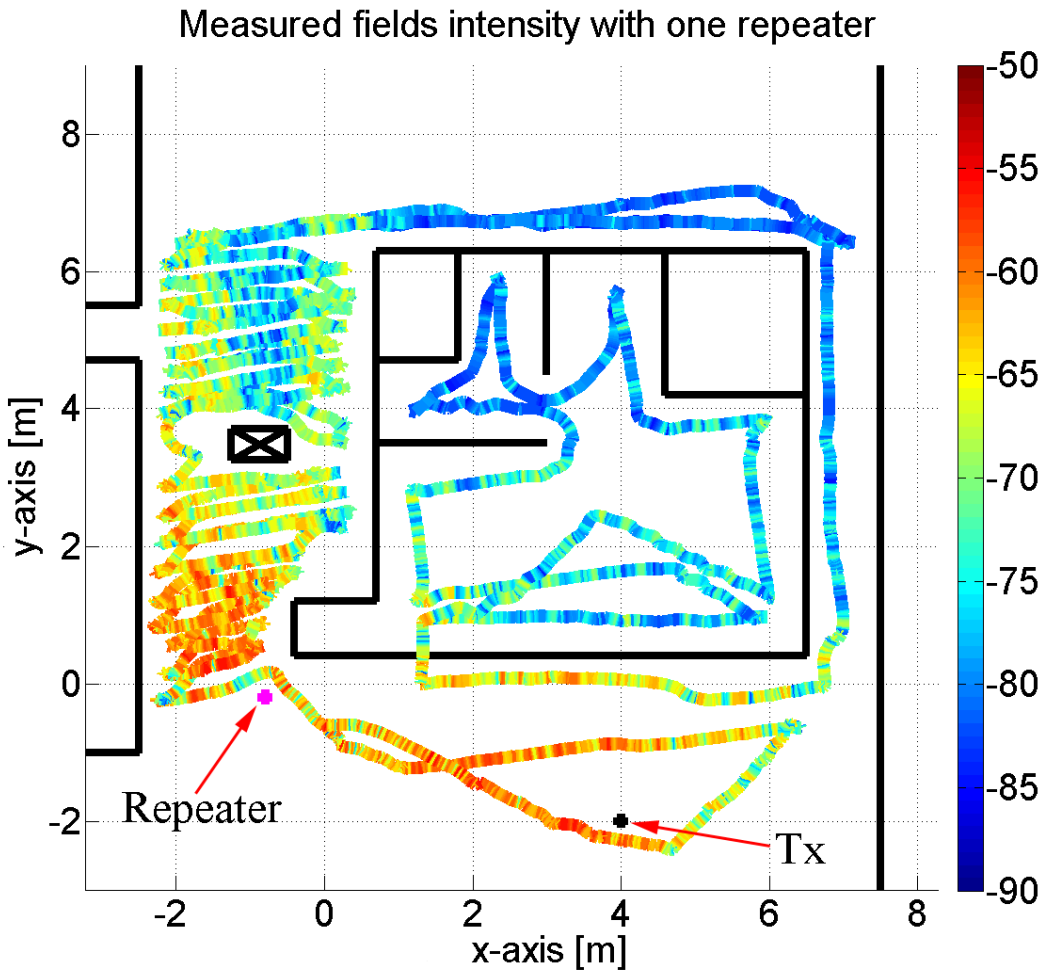

Figure A.2: Measured RSSI of a wooden building with one repeater.

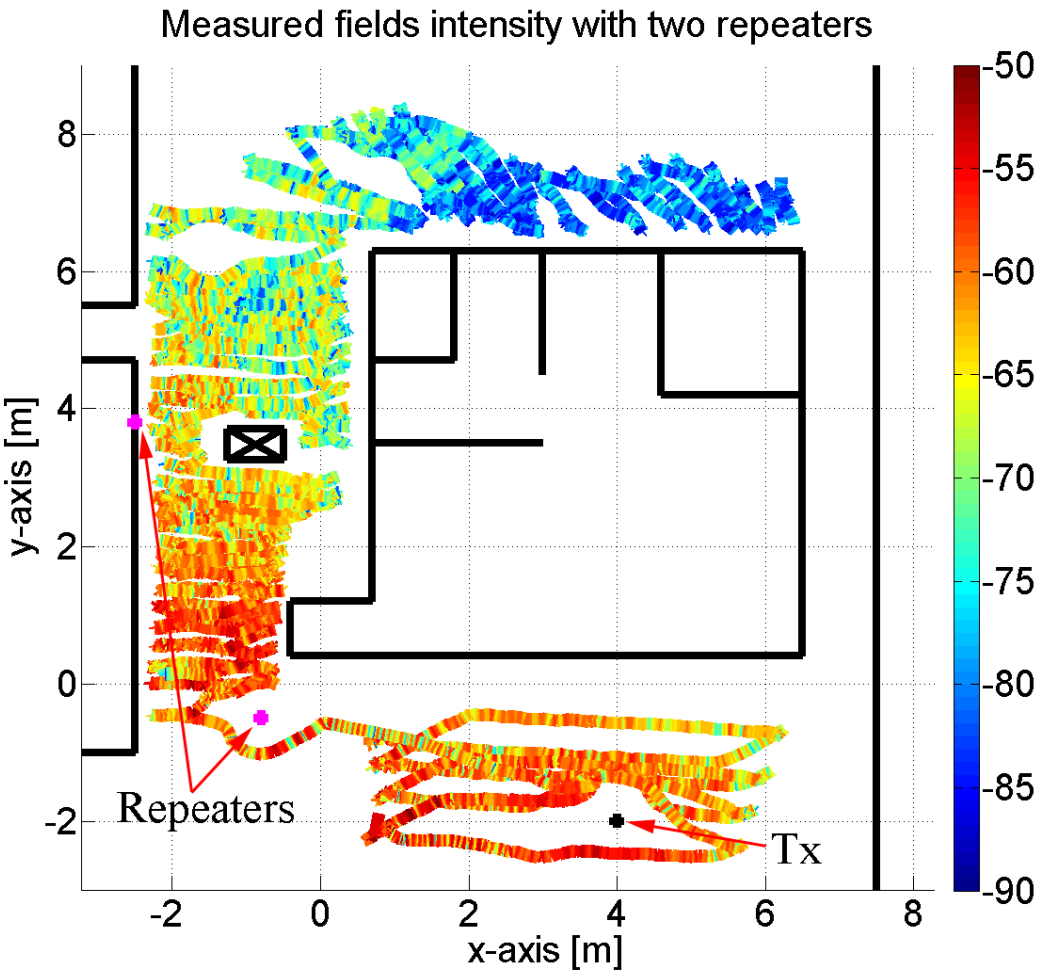

Figure A.3: Measured RSSI of a wooden building with two repeaters in a row.

APPENDIX B

RSSI measurement at a concrete building model 1

Since the radio repeater is designed to enhance the line-of-sight (LOS) propagation, it is suggested that more complex and realistic channel environments with less penetration should be measured to evaluate the performance of the proposed repeater. In order to provide the LOS communication link, the Tx antenna is located at the left-lower corner of the rectangular hallway, and RSSI is measured without repeaters in Fig. B.1. It is observed that the repeater at the right-lower corner enhances the signal strength along the right side of the hallway as shown in Fig. B.2. Furthermore, it is expected that by utilizing a pair of repeaters the first repeater amplifiers the LOS signal, and the second repeater further magnifies the output power of the amplified RF signal. Therefore, this configuration can greatly improve the strength and coverage of the wireless signal. Fig. B.3 shows the measured response utilizing a pair of repeaters at the right-lower corner. As can be seen, the signal strength at the right side of the hallway is completely improved and covered.

In this measurement[1], the transmit power was set to 10 dBm, and the gain of repeaters' RF amplifier was set to 50 dB which corresponds to 21.3 dBsm of RCS.

[1]This measurement was collaborated with Mr. Benjamin Charrow and Mr. James Stephan.

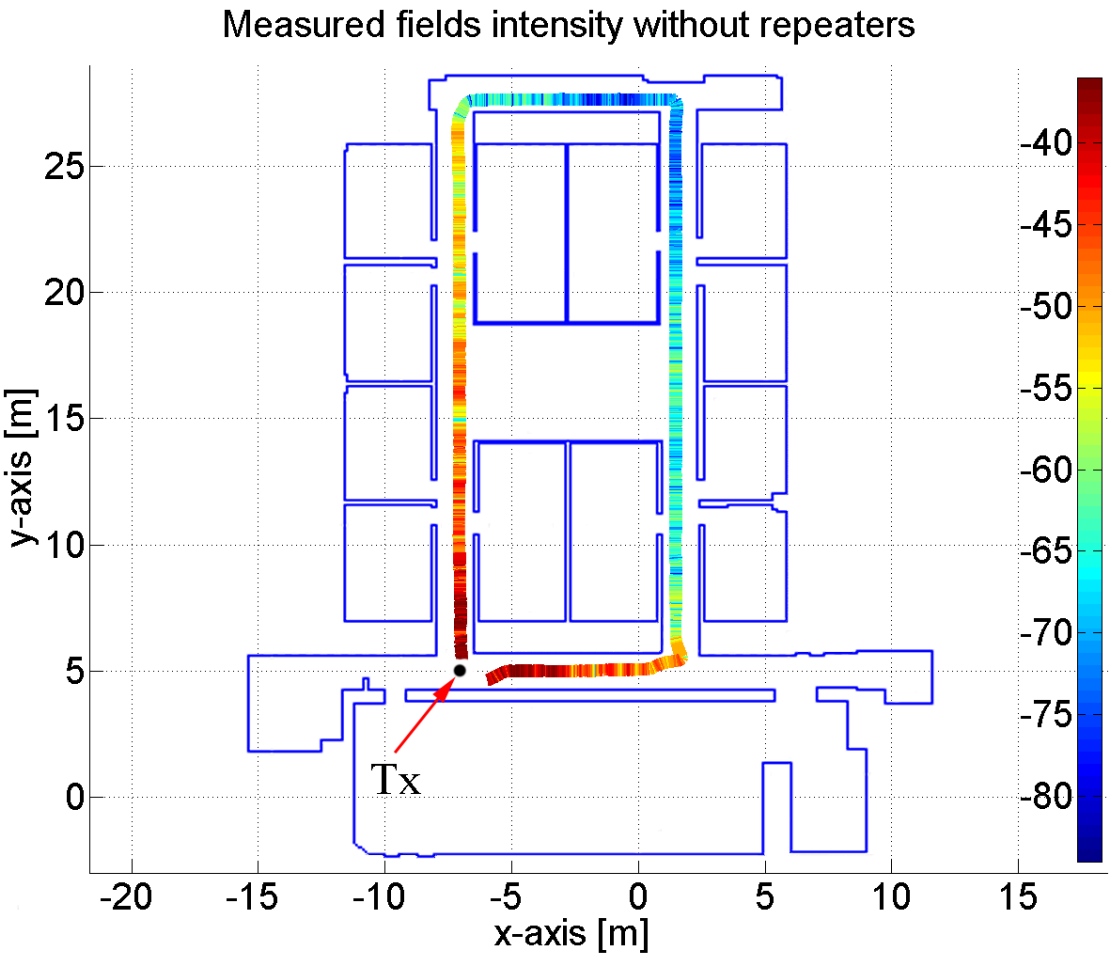

Figure B.1: Measured RSSI of a concrete building 1 without repeaters.

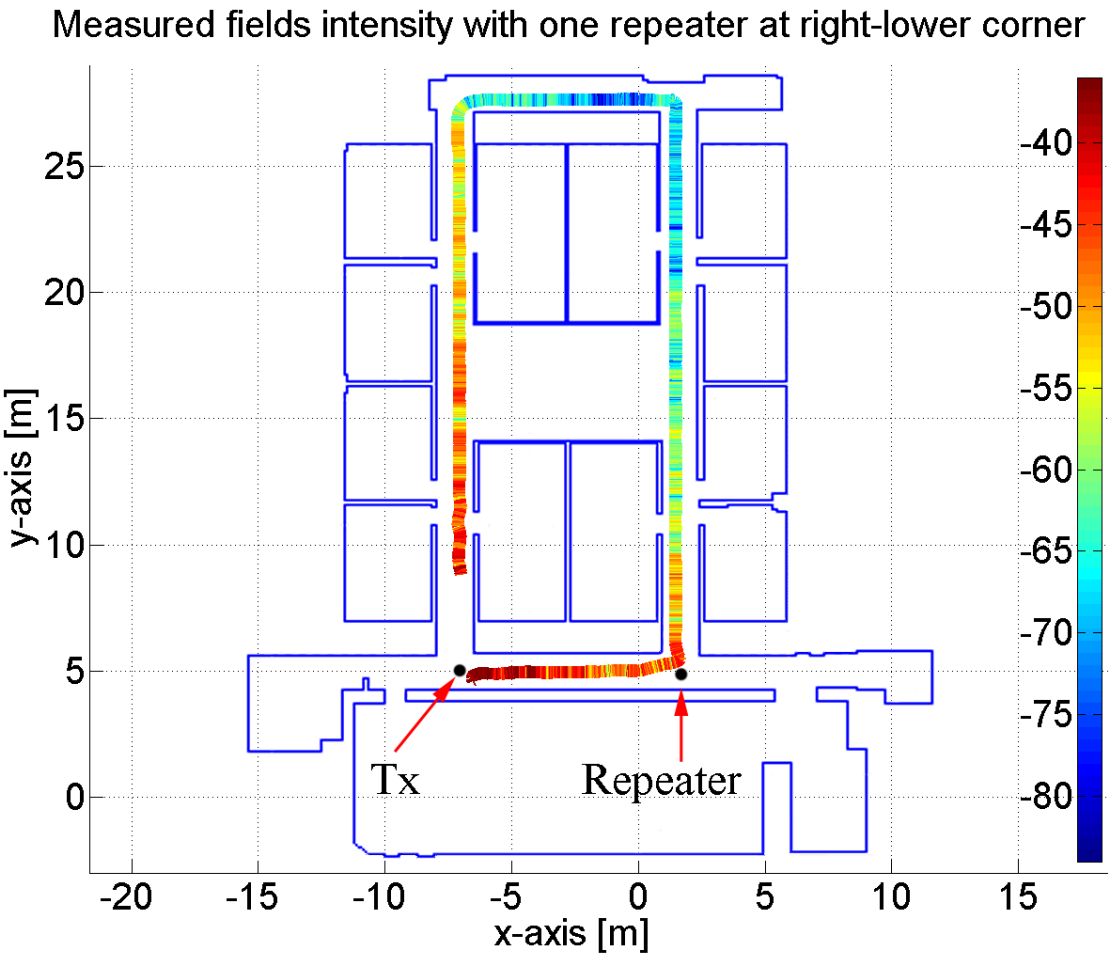

Figure B.2: Measured RSSI of a concrete building 1 with one repeater.

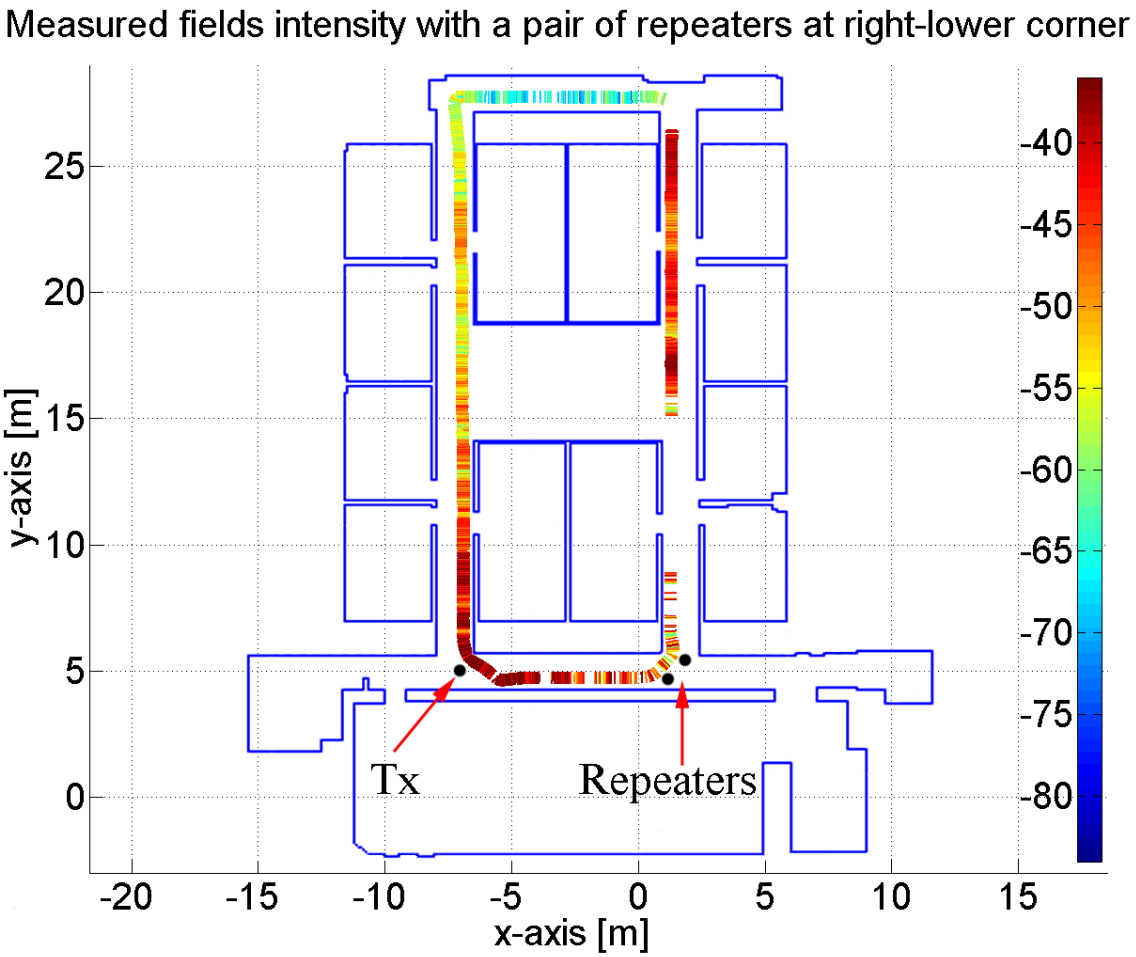

Figure B.3: Measured RSSI of a concrete building 1 with a pair of repeaters.

APPENDIX C

RSSI measurement at a concrete building model 2

Although significant improvements regarding the signal coverage is observed in Appendix A and B, it is suggested that the extension of the communication range should be measured in complex indoor channels. For this purpose, a pair of the proposed radio repeater is placed at the left-upper and left-lower corners as illustrated in Fig. C.1 [73]. Due to the multi-path propagation, the measured signal shows significant fast fading effect. In order to alleviate this severe fluctuation, a set of multiple points (about 10 cm apart) is measured and then averaged at each of Rx points P_i. Additionally, it should be noted that the XBee antenna modules require outgoing and incoming signal propagations in this measurement setup because the Tx antenna transmits the RF signal once it receives it from the Rx antenna. Therefore, the left-upper repeater is placed to amplify the signal from the Rx to the Tx antenna, and vise versa for the left-lower repeater. As reported in Fig. C.2, the placement of one repeater which enhances the signal from the Tx to the Rx antenna improves the signal strength by 8.2 dB and extends the communication range by 12.5 m.

In this measurement[1], the transmit power was set to 10 dBm, and the gain of repeaters' RF amplifier was set to 50 dB which corresponds to 21.3 dBsm of RCS.

[1]This measurement was collaborated with Dr. Fikadu Dagefu.

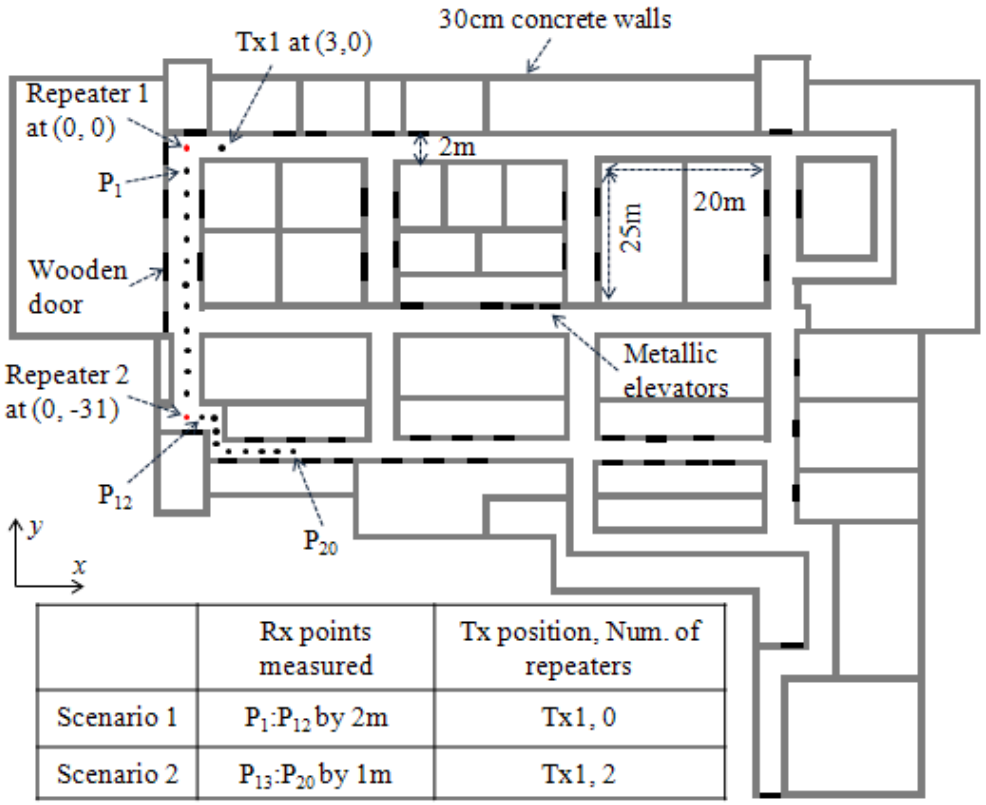

	Rx points measured	Tx position, Num. of repeaters
Scenario 1	P_1:P_{12} by 2m	Tx1, 0
Scenario 2	P_{13}:P_{20} by 1m	Tx1, 2

Figure C.1: Geometry of the measured indoor channel scenario.

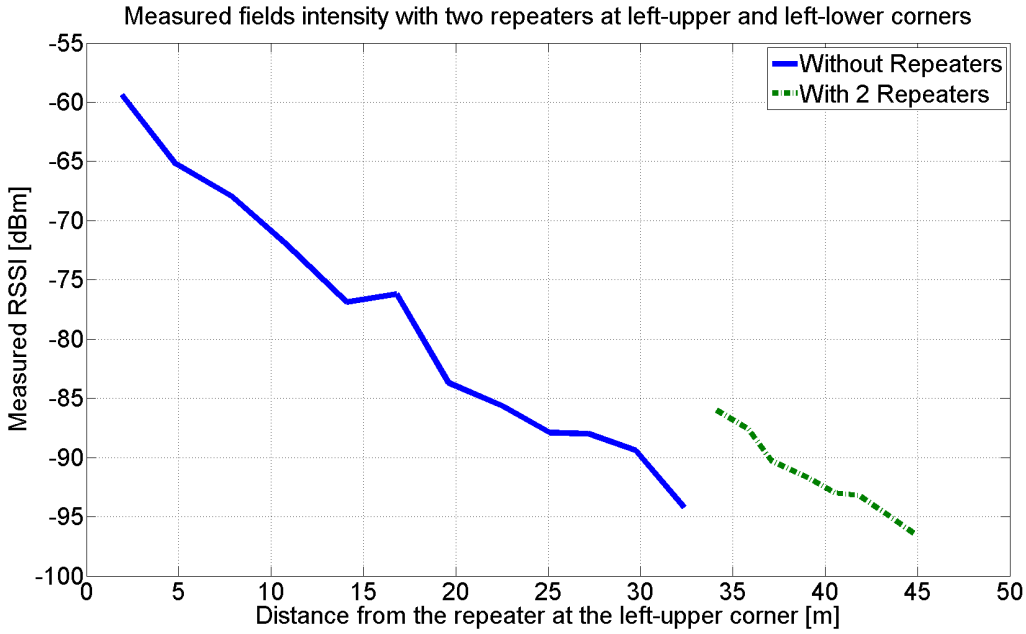

Figure C.2: Measured RSSI of a concrete building 2 with two repeaters.

BIBLIOGRAPHY

BIBLIOGRAPHY

[1] UNAVCO, "Mt. erebus serial radio repeater." `http://facility.unavco.org/kb/questions/507/Communications+Hardware+Used+by+UNAVCO+in+Polar+Applications`, 2004. [Online; accessed 8-April-2013].

[2] CISCO, "Cisco aironet 1140 series." `http://www.cisco.com/en/US/products/ps10092/index.htm`, 2010. [Online; accessed 8-April-2013].

[3] N. Blaunstein and Y. Ben-Shimol, "Prediction of frequency dependence of path loss and link-budget design for various terrestrial communication links," *IEEE Trans. Antennas Propag.*, vol. 52, pp. 2719 – 2729, Oct. 2004.

[4] Y. Wang, S. Safavi-Naeini, and S. Chaudhuri, "A hybrid technique based on combining ray tracing and fdtd methods for site-specific modeling of indoor radio wave propagation," *IEEE Trans. Antennas Propag.*, vol. 48, pp. 743 –754, May 2000.

[5] S. K. Park, P.-J. Song, and G. S. Bae, "Joint optimization of radio repeater location and linking in wll systems with 2.3 ghz frequency band," in *Proc. IEEE Int. Conf. Commun. (ICC)*, 1999, vol. 3, pp. 1617 –1621.

[6] C. K. Toh, *Ad hoc mobile wireless networks: protocols and systems*. Englewood Cliffs, NJ: Prentice-Hall, 2001.

[7] H. Li, M. Lott, M. Weckerle, W. Zirwas, and E. Schulz, "Multihop communications in future mobile radio networks," in *13th Int. Symp. Pers. Indoor and Mobile Radio Commun.*, Sep. 2002, vol. 1, pp. 54 – 58.

[8] R. Pabst, B. Walke, D. Schultz, P. Herhold, H. Yanikomeroglu, S. Mukherjee, H. Viswanathan, M. Lott, W. Zirwas, M. Dohler, H. Aghvami, D. Falconer, and G. Fettweis, "Relay-based deployment concepts for wireless and mobile broadband radio," *IEEE Commun. Mag.*, vol. 42, pp. 80 – 89, Sep. 2004.

[9] D. Sharp, N. Cackov, N. Laskovic, Q. Shao, and L. Trajkovic, "Analysis of public safety traffic on trunked land mobile radio systems," *IEEE J. Sel. Areas Commun.*, vol. 22, pp. 1197 – 1205, Sep. 2004.

[10] P. Slobodzian, "Estimation of the repeater gain required for a wireless link," in *Proc. 15th Int. Conf. Microw., Radar, Wireless Commun. (MIKON)*, May 2004, vol. 2, pp. 656 – 659 Vol.2.

[11] C. Cho, H. Zhang, and M. Nakagawa, "A uwb repeater with a short relaying-delay for range extension," in *Proc. IEEE Conf. Wireless Commun. Netw. (WCNC)*, Mar. 2004, vol. 2, pp. 1154 – 1158 Vol.2.

[12] M. Patwary, P. Rapajic, and I. Oppermann, "Capacity and coverage increase with repeaters in umts urban cellular mobile communication environment," *IEEE Trans. Commun.*, vol. 53, pp. 1620 – 1624, Oct. 2005.

[13] J. Borkowski, J. Niemela, T. Isotalo, P. Lahdekorpi, and J. Lempiainen, "Utilization of an indoor das for repeater deployment in wcdma," in *IEEE 63rd Veh. Technol. Conf. (VTC 2006-Spring)*, May 2006, vol. 3, pp. 1112 –1116.

[14] A. H. Naemat, A. Tee, A. S. M. Marzuki, B. Mohmd, K. Khalil, and A. R. A. Rahim, "Achieving optimum in-building coverage of 3g network in malaysia," in *Int. RF Microw. Conf. (RFM)*, Sep. 2006, pp. 343 –346.

[15] J. Laiho and T. N. Achim Wacker, eds., *Radio Network Planning and Optimisation for UMTS*. New York: John Wiley & Sons, Ltd, 2nd ed., Feb. 2006.

[16] K. Hiltunen, "Using rf repeaters to improve wcdma hsdpa coverage and capacity inside buildings," in *17th Int. Symp. Pers. Indoor and Mobile Radio Commun.*, Sep. 2006, pp. 1 –5.

[17] A. S. M. Marzuki, A. R. Rahim, B. Mohmd, K. Khalil, A. Naemat, and A. Tee, "Antenna isolation considerations in wcdma repeater deployment," in *Int. RF Microw. Conf. (RFM)*, Sep. 2006, pp. 347 –350.

[18] M. Merro, "An observational theory for mobile ad hoc networks (full version)," *Inform. Comput.*, vol. 207, no. 2, pp. 194 – 208, 2009.

[19] B. W. Lovinggood, M. D. Judd, and W. P. Kuiper, "Integrated repeater," U.S. Patent 6,934,511 B1, 2005.

[20] D. L. Runyon, S. B. Thompson, J. W. Maxwell, and D. L. M. SR., "Wireless repeater with feedback suppression features," U.S. Patent 2006/0 205 343 A1, 2006.

[21] V. Pan, "Extending wireless communication rf coverage inside building," U.S. Patent 7,406,300 B2, 2008

[22] B. G. Mats H Andersson, "Wireless communication mimo system with repeaters," U.S. Patent 8,032,080 B2, 2011

[23] Wikipedia, "Radio repeater — Wikipedia, the free encyclopedia." `http://en.wikipedia.org/wiki/Radio_repeater`, 2013. [Online; accessed 8-April-2013].

[24] J. Oh, M. Thiel, and K. Sarabandi, "Wave propagation management in indoor environments using micro-radio repeater systems," *IEEE Antennas Propagat. Mag.*, accepted for publication.

[25] T. W. Ban, B. Y. Cho, W. Choi, and H.-S. Cho, "On the capacity of a ds/cdma system with automatic on-off switching repeaters," in *Proc. IEEE Int. Conf. Commun. (ICC)*, 2001, vol. 3, pp. 780 –784.

[26] M. Lee, B. Keum, Y. Son, J.-W. Kim, and H. S. Lee, "A new low-complex interference cancellation scheme for wcdma indoor repeaters," in *Proc. IEEE Region 8 Int. Conf. Comput. Technol. Electr. Electron. Eng. (SIBIRCON)*, Jul. 2008, pp. 457 –462.

[27] M. Lee, B. Keum, M. Park, Y. S. Shim, H. S. Lee, and D. H. Woo, "A frequency domain approach for complexity reduction in wideband radio interference cancellation repeaters," in *Proc. 9th Int. Conf. Signal Process., (ICSP)*, Oct. 2008, pp. 1971 –1976.

[28] J.-Y. Choi, M.-S. Hur, Y.-W. Suh, J.-S. Baek, Y.-T. Lee, and J.-S. Seo, "Interference cancellation techniques for digital on-channel repeaters in t-dmb system," *IEEE Trans. Broadcast.*, vol. 57, pp. 46 –56, Mar. 2011.

[29] K.-L. Wong, J.-H. Chou, S.-W. Su, and C.-M. Su, "Isolation between gsm/dcs and wlan antennas in a pda phone," *Microw. Opt. Technol. Lett.*, vol. 45, no. 4, pp. 347–352, Aug. 2005.

[30] C.-M. Su, C.-L. Tang, S.-H. Yeh, and K.-L. Wong, "Optimized isolation between internal antennas for a dual-network wireless device," in *Proc. IEEE Int. Symp. Antennas Propag.*, Jul. 2005, vol. 2B, pp. 523 –526.

[31] H. Li, B. K. Lau, Z. Ying, and S. He, "Decoupling of multiple antennas in terminals with chassis excitation using polarization diversity, angle diversity and current control," *IEEE Trans. Antennas Propag.*, vol. 60, pp. 5947 –5957, Dec. 2012.

[32] J. Thaysen and K. B. Jakobsen, "Mutual coupling reduction using a lumped lc circuit," in *Int. Symp. Antennas (JINA)*, 2004, pp. 492–494.

[33] M. Karaboikis, C. Soras, G. Tsachtsiris, and V. Makios, "Compact dual-printed inverted-f antenna diversity systems for portable wireless devices," *IEEE Antennas Wireless Propag. Lett.*, vol. 3, pp. 9 –14, Dec. 2004.

[34] A. Diallo, C. Luxey, P. Le Thuc, R. Staraj, and G. Kossiavas, "Study and reduction of the mutual coupling between two mobile phone pifas operating in the dcs1800 and umts bands," *IEEE Trans. Antennas Propag*, vol. 54, pp. 3063 –3074, Nov. 2006.

[35] M. Salehi and A. Tavakoli, "A novel low mutual coupling microstrip antenna array design using defected ground structure," *Int. J. Electron. Commun.*, vol. 60, no. 10, pp. 718 – 723, 2006.

[36] C.-Y. Chiu, C.-H. Cheng, R. Murch, and C. Rowell, "Reduction of mutual coupling between closely-packed antenna elements," *IEEE Trans. Antennas Propag.*, vol. 55, pp. 1732 –1738, Jun. 2007.

[37] T. Kokkinos, E. Liakou, and A. Feresidis, "Decoupling antenna elements of pifa arrays on handheld devices," *Electron. Lett.*, vol. 44, pp. 1442 –1444, 4 2008.

[38] A. Mak, C. Rowell, and R. Murch, "Isolation enhancement between two closely packed antennas," *IEEE Trans. Antennas Propag.*, vol. 56, pp. 3411 –3419, Nov. 2008.

[39] Y.-S. Wang, J.-C. Lu, and S.-J. Chung, "A miniaturized ground edge current choke - design, measurement, and applications," *IEEE Trans. Antennas Propag.*, vol. 57, pp. 1360 –1366, May 2009.

[40] S.-W. Su, C.-T. Lee, and F.-S. Chang, "Printed mimo-antenna system using neutralization-line technique for wireless usb-dongle applications," *IEEE Trans. Antennas Propag.*, vol. 60, pp. 456 –463, Feb. 2012.

[41] S.-C. Chen, Y.-S. Wang, and S.-J. Chung, "A decoupling technique for increasing the port isolation between two strongly coupled antennas," *IEEE Trans. Antennas Propag.*, vol. 56, pp. 3650 –3658, Dec. 2008.

[42] M. Moharram and A. Kishk, "Decoupling between two asymmetric non-perfectly matched antennas for mimo applications," in *Proc. IEEE Int. Symp. Antennas Propag.*, Jul. 2012, pp. 1 –2.

[43] X. Q. Lin, H. Li, S. He, and Y. Fan, "A decoupling technique for increasing the port isolation between two closely packed antennas," in *Proc. IEEE Int. Symp. Antennas Propag.*, Jul. 2012, pp. 1 –2.

[44] R. A. Shelby, D. R. Smith, S. C. Nemat-Nasser, and S. Schultz, "Microwave transmission through a two-dimensional, isotropic, left-handed metamaterial," *Appl. Phys. Lett.*, vol. 78, no. 4, pp. 489–491, 2001.

[45] C. Caloz and T. Itoh, *Electromagnetic Metamaterials: Transmission Line Theory and Microwave Applications: The Engineering Approach.* New York: Wiley-IEEE Press, Nov. 2005.

[46] D. Schurig, J. J. Mock, B. J. Justice, S. A. Cummer, J. B. Pendry, A. F. Starr, and D. R. Smith, "Metamaterial electromagnetic cloak at microwave frequencies," *Science*, vol. 314, no. 5801, pp. 977–980, 2006.

[47] M. Bait-Suwailam, M. Boybay, and O. Ramahi, "Electromagnetic coupling reduction in high-profile monopole antennas using single-negative magnetic metamaterials for mimo applications," *IEEE Trans. Antennas Propag.*, vol. 58, pp. 2894 –2902, Sep. 2010.

[48] D. Sievenpiper, L. Zhang, R. Broas, N. Alexopolous, and E. Yablonovitch, "High-impedance electromagnetic surfaces with a forbidden frequency band," *IEEE Trans. Microw. Theory Tech.*, vol. 47, pp. 2059 –2074, Nov. 1999.

[49] Y. Rahmat-Samii and H. Mosallaei, "Electromagnetic band-gap structures: classification, characterization, and applications," in *Proc. 11th Int. Conf. Antennas Propag. (ICAP)*, 2001, vol. 2, pp. 560 –564.

[50] F. Yang and Y. Rahmat-Samii, "Microstrip antennas integrated with electromagnetic band-gap (ebg) structures: a low mutual coupling design for array applications," *IEEE Trans. Antennas Propag.*, vol. 51, pp. 2936 – 2946, Oct. 2003.

[51] E. Rajo-Iglesias, O. Quevedo-Teruel, and L. Inclan-Sanchez, "Mutual coupling reduction in patch antenna arrays by using a planar ebg structure and a multilayer dielectric substrate," *IEEE Trans. Antennas Propag.*, vol. 56, pp. 1648 –1655, Jun. 2008.

[52] K. Buell, H. Mosallaei, and K. Sarabandi, "A substrate for small patch antennas providing tunable miniaturization factors," *IEEE Trans. Microw. Theory Tech.*, vol. 54, pp. 135 –146, Jan. 2006.

[53] K. Buell, H. Mosallaei, and K. Sarabandi, "Metamaterial insulator enabled superdirective array," *IEEE Trans. Antennas Propag.*, vol. 55, pp. 1074 –1085, Apr. 2007.

[54] H. Mosallaei and K. Sarabandi, "Design and modeling of patch antenna printed on magneto-dielectric embedded-circuit metasubstrate," *IEEE Trans. Antennas Propag.*, vol. 55, pp. 45 –52, Jan. 2007.

[55] K. Sarabandi and Y. J. Song, "Subwavelength radio repeater system utilizing miniaturized antennas and metamaterial channel isolator," *IEEE Trans. Antennas Propag.*, vol. 59, pp. 2683 –2690, Jul. 2011.

[56] Y. J. Song and K. Sarabandi, "Miniaturized radio repeater for enhanced wireless connectivity of ad-hoc networks," *IEEE Trans. Antennas Propag.*, vol. 60, pp. 3913 –3920, Aug. 2012.

[57] Y. J. Song and K. Sarabandi, "System gain and performance enhancement of miniaturized radio repeaters for ad-hoc wireless communication," in preparation.

[58] K. Payandehjoo and R. Abhari, "Employing ebg structures in multiantenna systems for improving isolation and diversity gain," *IEEE Antennas Wireless Propag. Lett.*, vol. 8, pp. 1162 –1165, 2009.

[59] S. Ghosh, T.-N. Tran, and T. Le-Ngoc, "A dual-layer ebg-based miniaturized patch multi-antenna structure," in *Proc. IEEE Int. Symp. Antennas Propag.*, Jul. 2011, pp. 1828 –1831.

[60] H. Mosallaei and K. Sarabandi, "A compact wide-band ebg structure utilizing embedded resonant circuits," *IEEE Antennas Wireless Propag. Lett.*, vol. 4, pp. 5 – 8, 2005.

[61] D. F. Sievenpiper, *High-Impedance Electromagnetic Surfaces*. Ph.D. thesis, The University of California, Los Angeles, 1999.

[62] H. Mosallaei and K. Sarabandi, "Antenna miniaturization and bandwidth enhancement using a reactive impedance substrate," *IEEE Trans. Antennas Propag.*, vol. 52, pp. 2403 – 2414, Sep. 2004.

[63] C. A. Balanis, *Antenna Theory*. NJ: Wiley, 3rd ed., 2005.

[64] R. Igreja and C. J. Dias, "Analytical evaluation of the interdigital electrodes capacitance for a multi-layered structure," *Sensors and Actuat. A: Phys.*, vol. 112, no. 2-3, pp. 291 – 301, 2004.

[65] R. Collin, *Foundations for Microwave Engineering*. New York: John Wiley & Sons, 2007.

[66] D. Liao and K. Sarabandi, "Terminal-to-terminal hybrid full-wave simulation of low-profile, electrically-small, near-ground antennas," *IEEE Trans. Antennas Propag.*, vol. 56, pp. 806 –814, Mar. 2008.

[67] W. Hong and K. Sarabandi, "Low-profile, multi-element, miniaturized monopole antenna," *IEEE Trans. Antennas Propag.*, vol. 57, pp. 72 –80, Jan. 2009.

[68] D. M. Pozar, *Microwave Engineering*. NJ: Wiley, 3rd ed., 2005.

[69] K. Chung, T. Yun, and J. Choi, "Wideband cpw-fed monopole antenna with parasitic elements and slots," *Electron. Lett.*, vol. 40, pp. 1038 – 1040, Aug. 2004.

[70] C.-Y. Pan, T.-S. Horng, W. Chen, and C.-H. Huang, "Dual wideband printed monopole antenna for wlan/wimax applications," *IEEE Antennas Wireless Propag. Lett.*, vol. 6, pp. 149 –151, 2007.

[71] J. Oh and K. Sarabandi, "Low profile vertically polarized omnidirectional wideband antenna with capacitively coupled parasitic elements," *IEEE Trans. Antennas Propag.*, submitted in 2012.

[72] Digi, "Xbee-pro 802.15.4." `http://www.digi.com/products/wireless-wired-embedded-solutions/zigbee-rf-modules/point-multipoint-rfmodules/xbee-series1-module`, 2009. [Online; accessed 8-April-2013].

[73] F. T. Dagefu, *Exploitation and Mitigation of Multipath in Complex Wave Propagation Environments for Target Detection, Tracking, and Communication*. Ph.D. thesis, The University of Michigan, 2012.